Ionization Instability of the Hollow Cathode Plume

by

Marcel P. Georgin

A dissertation submitted in partial fulfillment
of the requirements for the degree of
Doctor of Philosophy
(Applied Physics)
in the University of Michigan
2020

Doctoral Committee:

Professor Alec D. Gallimore, Co-Chair
Assistant Professor Benjamin A. Jorns, Co-Chair
Associate Professor Ryan D. McBride
Dr. Ioannis G. Mikellides, Jet Propulsion Laboratory
Mr. Timothy R. Sarver-Verhey, Glenn Research Center

"Electrons are sneaky little termites."

– Sarah E. Cusson

Marcel P. Georgin

georginm@umich.edu

ORCID iD: 0000-0003-3733-1682

To my family

ACKNOWLEDGMENTS

This work was funded by the NASA Space Technology Research Fellowship, grant number NNX15AQ37H. In addition, I also received funding from the Michigan Institute for Plasma Science and Engineering Fellowship. Beyond this financial support, I would also like to thank my co-advisors Alec Gallimore and Benjamin Jorns. To Alec, thank you for giving me the opportunity to discover my passion for plasma physics, propulsion, and academic research. To Ben, thank you focusing my efforts and always challenging me to think about problems in new exciting ways. Together, my co-advisors have molded me into the researcher that I am today.

This degree would not have been possible without the help and camaraderie of my labmates in the Plasmadynamics and Electric Propulsion Laboratory. While getting to know everyone made the challenges of graduate school bearable, in particular, I am grateful to have had the opportunity to work with Ethan Dale. He was invaluable at every step of the way throughout my graduate education, from setting up experiments to being open to listening to my theories. Without his input I'm confident I would have taken at least an extra year to complete my degree.

Lastly, I am thankful for the encouragement of my family, who taught me to value education and enabled me to pursue my dreams. But most of all, I would like to thank my colleague, best friend, teacher, and wife Sarah Cusson who has always pushed me to be the best that I can be all the while putting up with my charming nonsense. She has helped me grow personally and professionally and I am excited to continue taking on the challenges of life together.

All of these wonderful individuals have had a lasting impact on this work and on me as a person. This dissertation, in many ways, is an amalgamation of these influences and hopefully puts to rest a few questions in plasma physics as it pertains to electric propulsion devices.

TABLE OF CONTENTS

LIST OF FIGURES

Figure

LIST OF TABLES

Table

NOMENCLATURE

Roman

a	fit parameter
A	area
b	fit parameter
c	integration constant
E	electric field
f	frequency
I	current
j	current density
ℓ	lengthscale
L	gradient lengthscale
m	mass
n	density
q	unit charge
r	radius
R	radius
S	dispersion
t	time
u	drift velocity
v	thermal velocity
V	voltage or volume
z	axial position

Greek

α	ratio of the plasma density ot the neutral density
α_1	constant of proportionality for the anomalous collision frequency

β	constant of proportionality indicating the non-linearity of the ionization rate with temperatu
γ	growth rate
γ_e	electron contribution to the growth rate of IAT
γ_{iz}	response of ionization to temperature fluctuations
Γ_i	ratio of ion flux to the ionization rate
Γ_n	ratio of neutral influx to the ionization rate
δ	ratio of outlet electron temperature times the inlet density to the product of the inlet tempe
ϵ	the ratio of the gradient lengthscale to the ionization mean free path
ϵ_{iz}	the ionization energy of xenon
ϵ_i	the imaginary part of the dispersion
ϵ_r	the real part of the dispersion
η	ratio of the electron collision frequency to the electron transit rate
η_{iz}	ratio of the ionization rate to electron transit frequency
ν	frequency
Φ	potential
ω	oscillation frequency

Subscripts (Unless Specified Above)

an	anomalous
ca	cathode to anode
dc	discharge
D	diffusion
$Diff$	diffusion
e	electron property
ei	electron-ion
en	electron-neutral
i	ion property
in	inlet value or ion-neutral
iz	ionization
IAT	IAT property
k	evaluated at the keeper or designates the k^{th} mode
n	neutral property
o	evaluated at the orifice
p	probe

probe	probe
r	real component
sat	saturation
th	thermal
ω	mode with frequency ω
0	steady state value
1	first order, linear perturbation

Constants

q	Elementary charge, 1.602×10^{-19} C
k_b	Boltzmann constant, 1.38×10^{-23} J/K

Abbreviations

IAT	Ion Acoustic Turbulence
BaO	Barium Oxide
JPL	Jet Propulsion Laboratory
LaB_6	Lanthanum hexaboride
LIF	Laser-induced fluorescence
LP	Langmuir Probe
NASA	National Aeronautics and Space Administration
PEPL	Plasmadynamics and Electric Propulsion Laboratory
SCCM	Standard cubic centimeters per minute

ABSTRACT

This work explores a possible mechanism for the onset of a poorly-understood, low-frequency plasma wave that arises in the plume region of thermionic hollow cathodes used for electric propulsion systems. This phenomenon is often referred to as the plume mode instability. Previous experimental measurements and descriptions of the wave are first reviewed. These results are often interpreted as an ionization wave, although there no direct evidence. Simulations that resolve the oscillation suggest that nonclassical electron heating via ion acoustic waves is critically linked to this behavior. Initial experiments, presented herein, show that the plume mode instability is a spatially localized phenomenon where large oscillations in ion acoustic wave amplitude are able to drive fluctuations in plasma resistivity and electron temperature. The phase relationship between temperature and density is shown to be consistent with a changing ionization rate, ultimately making the experimental connection to an ionization driven mode. Synthesizing this evidence, a physically plausible mechanism for the onset and growth of the instability is devised. It is proposed that predator-prey behavior between the electrons and neutral atoms, a process that is mediated by ionization, could be destabilized by the temperature fluctuations caused by the ion acoustic waves. A 0-dimensional, analytical model for a predator-prey instability is derived. This system of equations is analyzed under three different scenarios for the dominant form of electron collisionality: Coulomb collisions, large and constant collisions, and saturated wave-driven collisions. The result of the Coulomb collision analysis shows that the wave is ultimately damped by plasma diffusion and the neutral influx from the cathode. The other two con-

ditions provide a stability criterion. If enhanced ionization due to temperature fluctuations exceeds the losses to diffusion and the influx of neutral atoms, then the wave begins to grow. The onset criterion is manipulated to show that it can be interpreted as a critical electron temperature that varies weakly on the neutral density. This is shown to be equivalent to a critical discharge voltage. The theory is then evaluated using experimental data over a broad range of discharge currents and mass flow rates. The theoretical growth rate and oscillation frequency are found to be positively correlated to the measured wave amplitude and frequency, respectively. This result corroborates our theory that the plume mode wave is likely a predator-prey ionization instability that is driven unstable by temperature fluctuations made possible by the presence of enhanced Ohmic heating of electrons due to the ion acoustic turbulence. Lastly, the presence of waves is examined experimentally under an applied magnetic field – an environment that is more representative of a cathode used in a Hall effect thruster. It is shown that the plume mode instability is ultimately damped with increasing magnetic field and that rotating anti-drift waves can form in the same frequency band. The keeper oscillations typically associated with the plume mode wave are likely the result of anti-drift waves when operating in a Hall effect thruster.

CHAPTER 1

Introduction

Low-temperature plasmas find many technological uses from semiconductor etching to medicine. The work herein is motivated by the application of this class of plasmas to space propulsion. These so-called electric propulsion systems are now being widely deployed on commercial satellites and military spacecraft and are a critical element of several current and future deep space exploration missions. Their increased popularity is driven by the relatively high propellant exhaust velocity that can be achieved with these devices over that of traditional chemical rockets. This key feature of electric propulsion reduces the overall mass and cost of a spacecraft, making it an enabling technology for new ambitious space missions and commercial ventures.

Notably, NASA's long term goals for the robotic and manned exploration of deep space hinges upon the use of high-power Hall thrusters. Preparing for these long duration missions poses a new set of scientific and technical challenges that need to be addressed. For example, flight qualification of propulsion devices typically requires end-to-end testing of the system for its intended life-span with some margin of safety. However, since deep space missions require the propulsion system to operate almost continuously for several years, there is an apparent need for a new paradigm for flight qualification; namely, qualification through predictive modeling. This process reduces time and cost; however, particularly in the subfield of Hall thruster research and development, such simulation capabilities do not exist. This is in part because of non-classical behavior in the plasma formed by these devices. Further-

more, to model a full thruster using particle methods is too computationally intensive and reduced-fidelity, fluid codes require modification to account for myriad kinetic effects, such as non-Maxwellian particle distributions and the non-classical effects of turbulence that are becoming increasingly important to our understanding of these devices.

One area of the Hall thruster that behaves non-classically is the plume of the hollow cathode. This subsystem supplies the necessary electron current to the thruster to maintain the discharge and neutralize the ion beam. A long-standing question for cathode physics has been describing the so-called spot-to-plume mode transition; where the initially steady current produced by the device in spot mode becomes highly oscillatory in plume mode. Associated with this transition is the presence of an ionization-like instability, whose amplitude can be on the order of the time-average plasma parameters and is linked to the generation of energetic ions that enhance cathode erosion. This transition is furthermore connected with the formation of a large-scale, coherent structure near the device, the so-called "plasma ball." Overall, these properties and structures have yet to be described through classical physics or modeling and so it is difficult to predict this deleterious behavior on orbit. As such, this lack of insight poses a risk to long duration deep space missions. Thus, it is imperative that we better understand this mode transition and the ionization instability from first principles.

In this context, our aim is to identify an intuitive physical mechanism for this seemingly non-classical process and to support it through theory and experiment. To this end, we have organized this thesis in the following manner. In Chapter 2, we provide a background of previous work and the relevant physics used to describe the cathode plasma plume. Then in Chapter 3 we conduct a few exploratory experiments where the time-dependent plasma parameters are measured to identify key properties of the wave and any simplifying assumptions that can be implemented in an analytical theory. In Chapter 4, we use this insight to derive a stability criterion for the plume mode wave. This expression for the onset is evaluated experimentally in Chapter 5 by conducting a parameter sweep and measuring both plasma and wave properties. The plume mode instability is then experimentally characterized in

the presence of a magnetic field (similar to what might be experience in a Hall thruster) and analyzed in the context of leading theories for the formation of other large-scale structures in the plume. Lastly, we conclude in Chapter 7 with our major results and contributions to the field along with some future work on this topic.

CHAPTER 2

Background

2.1 Introduction

In this Chapter, we first overview the function and geometry of the hollow cathode. Then, we review the existing body of literature on the spot-to-plume mode transition and the associated plasma instability. This information is presented in a chronological fashion, first focusing on early experimental results and theoretical descriptions of the wave. Next, we pivot towards numerical findings that have advanced our thinking about the problem, notably making the connection to enhanced heating due the presence of ion acoustic turbulence in the plume. We then provide a high-level description of IAT, its various characteristics, and the known effects it has on the cathode plasma parameters. These previous results are used to guide a initial experimental investigation that is described later in Chapter 3.

2.2 The Hollow Cathode

Direct current (DC) plasmas, for example a neon sign, rely on secondary electron emission from ions impacting the negative electrode, i.e. the cathode, to sustain the discharge. The sheath at the cathode is typically a few hundred volts for the ions to gain sufficient kinetic energy such that an electron is emitted when they impinge upon the cathode surface. For propulsion applications, this large sheath voltage can be thought of as a penalty for extracting electrons to the thruster and is ultimately an efficiency loss for the system. [6] The hollow

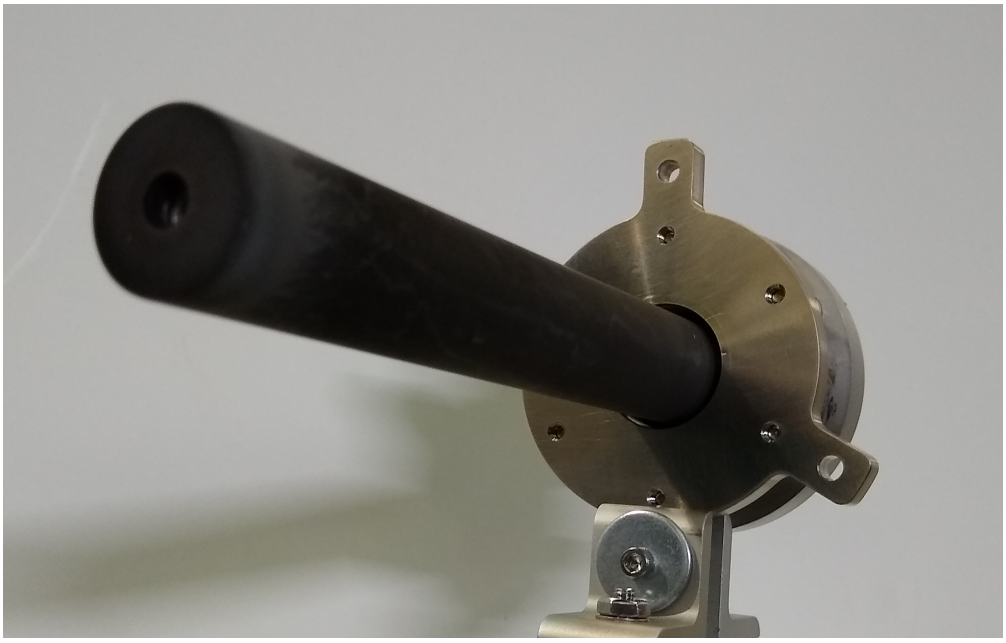

Figure 2.1: A hollow cathode design capable of providing 5 - 100 A of discharge current for use in Hall thrusters and nested Hall thrusters. [1]

cathode is a technology that uses a tubular electrode, in contrast to the usual planar cathode geometry, that enhances secondary electron emission from the walls through the so-called hollow cathode effect. This was first recognized by Friedrich Paschen in 1916. [7] Because of the cathode's shape, the electron residence time in the cathode region is increased. The electrons bounce between the walls of the cathode and ultimately enhance electron production through additional secondary electron emission, among other processes. From a system standpoint, this exponentially reduces the necessary voltage to produce electrons and maintain the plasma, [8] therefore improving the efficiency of DC plasma discharges.x

For propulsion applications, the tubular cathode is made of a low work-function, thermionic material. Common materials are LaB_6 [9–12] or W-BaO. [13] The emitter, also referred to as the insert, is heated using a resistive element to achieve electron emission. These free electrons then interact with the neutral gas provided to the device, producing ions through electron impact ionization. The highly collisional plasma keeps the electrons relatively cold ($\sim$ 1 eV) which results in low sheath voltages. [6] This property makes thermionic

emitting hollow cathodes ideal for generating large currents at low voltages. High-power electric propulsion systems, such as ion and Hall thrusters, can be made upwards of 60% efficient when using hollow cathode electron sources, like the one shown in Fig. 2.1. Figure 2.2 is an illustration of the internal geometry of a state-of-the-art cathode. To ignite the plasma, the thermionic emitter is first heated with the resistive heating element to produce an electron gas. Xenon gas (typically used for propulsion) is then introduced to the system. The keeper electrode is biased to a high voltage to increase the kinetic energy of the electrons, such that they ionize the neutral gas. After the initial ignition, a constant current is typically extracted from the cathode by a downstream discharge anode and the keeper electrode is left floating (collects no current). In this configuration, the cathode enters an autothermionic state, where the plasmas impinging upon the insert is able to maintain the emitter temperature to efficiently sustain the current demanded by the propulsion system.

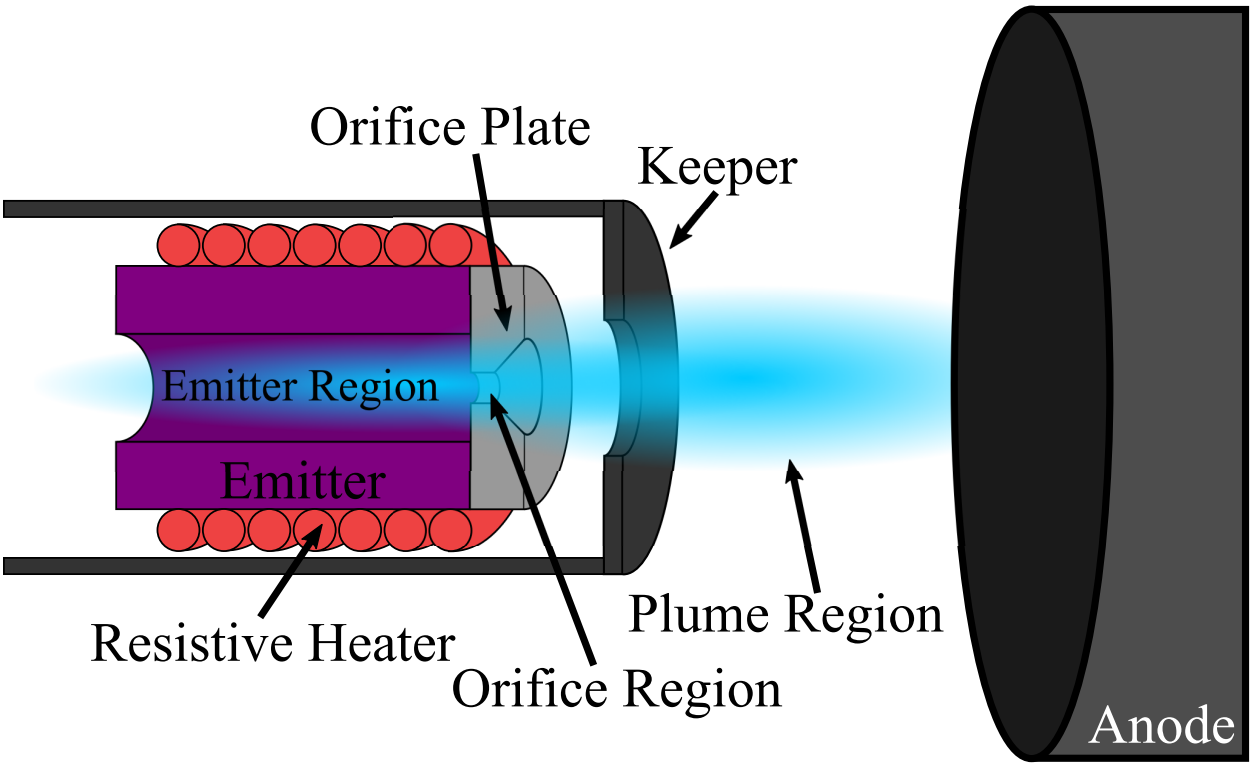

Figure 2.2: Hollow cathode geometry showing the tubular thermionic emitter, the orifice plate, keeper electrode and plasma plume.

There are three primary regions of these devices where the dominant physics changes drastically. These three regions are identified in Fig. 2.2, as the emitter (insert), orifice, and plume regions. These are discussed at length in Ref. [6]. Here we simply provide a short overview of driving physics in each of these areas. In the insert region, the neutral gas is at relatively high pressure and the plasma is cold and dense. [14–19] Here, the thermionic emission of electrons and the ionization of the neutral gas through electron-impact and photo-ionization play an important role in dictating the plasma state. In the orifice region, the plasma reaches its highest densities and the energy balance is primarily dictated by Coulomb and wall collisions. [19,20] Downstream of the orifice is the plume region where the plasma transitions from a highly collisional fluid to a nearly collisionless plasma over a few centimeters. This region of the plasma is the primary area of investigation for this body of work. However, as is discussed in later Chapters, the plasma state of this region cannot be described with classical plasma physics. These properties make this section of the plasma of great theoretical interest with practical consequences for propulsion. [2, 4, 20–22]

2.3 Experiments on Cathode Stability

Early experiments on cathode stability for ion thrusters [23–28] identified two modes of operation, the so-called spot and plume modes, which are shown in Fig. 2.3. [29–33] The spot mode is relatively quiescent and dim while the plume mode is bright and exhibits characteristically large discharge current oscillations like the ones shown Fig. 2.4 (a). Experimentally, the mode transition is typically induced by reducing the mass flow rate to the device as shown in Fig. 2.4 (b), where the oscillation amplitude begins to rise below a flow rate of 7 sccm. More generally, the plume mode oscillations tend to grow at the confluence of high discharge current and low propellant flow rate. In combination, this empirical onset criterion has lead to the interpretation of this mode transition as being ionization-related and is thought to onset above a critical ionization fraction. Although this interpretation of the

results is intuitive, there is no direct experimental evidence or theoretical basis for why the discharge current begins to oscillate in plume mode.

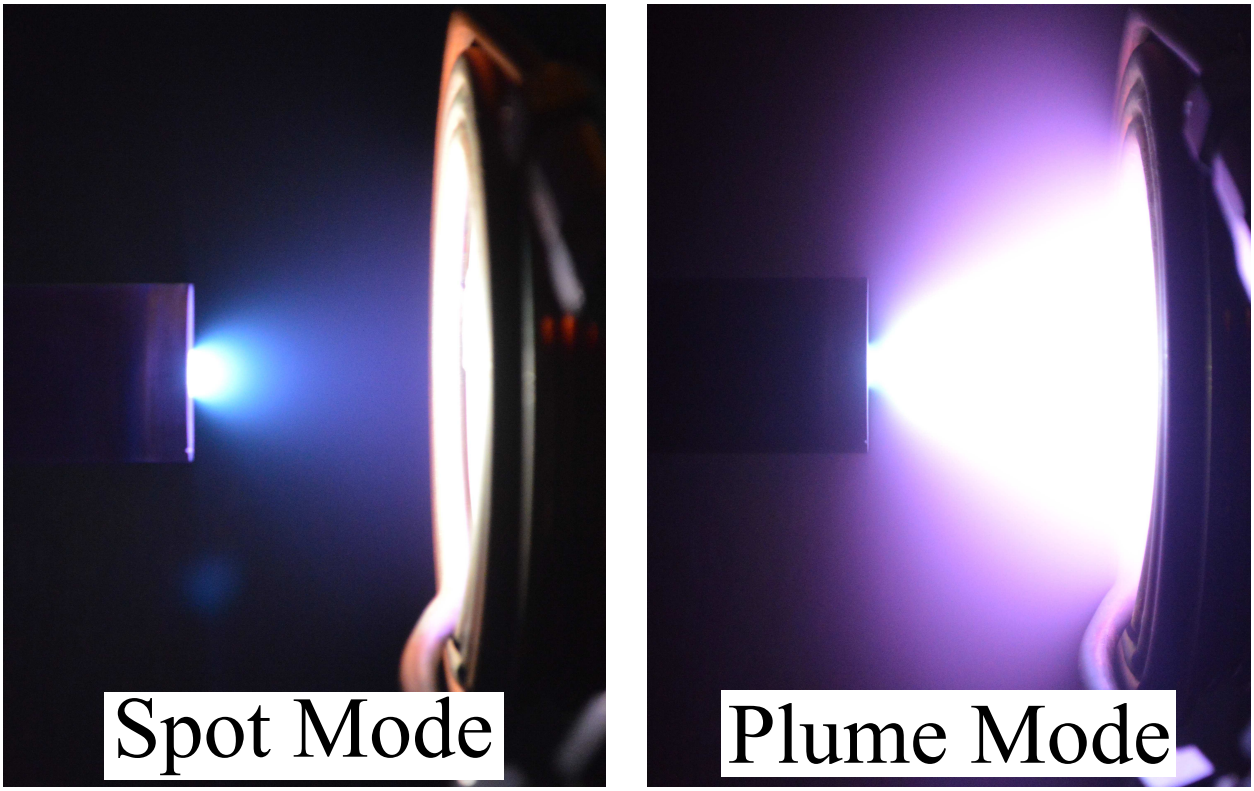

Figure 2.3: Spot and plume mode discharges. The transition from spot to plume mode is induced by reducing the flow rate to the cathode from 15 to 5 sccm Xe.

The use of hollow cathodes in high-power Hall thrusters for extended deep space missions has spurred a new set of investigations into this poorly understood mode transition. The plume mode was shown to be correlated with greater discharge voltage and the presence of high energy ions that lead to enhanced erosion of cathode surfaces, a deleterious effect for space propulsion. [19, 34–36] Seminal work by Goebel, reproduced in Figs. 2.4 (a) and (b), showed that the question of cathode stability is intrinsically linked to the presence of plasma waves that exist in the plume of the device. The work in Ref. [2] showed that the global discharge current fluctuations in plume mode are the result of plasma potential oscillations that exist exclusively in the plume region. These waves periodically produce large spike in plasma potential at a frequency near the ionization rate, further connecting the plume

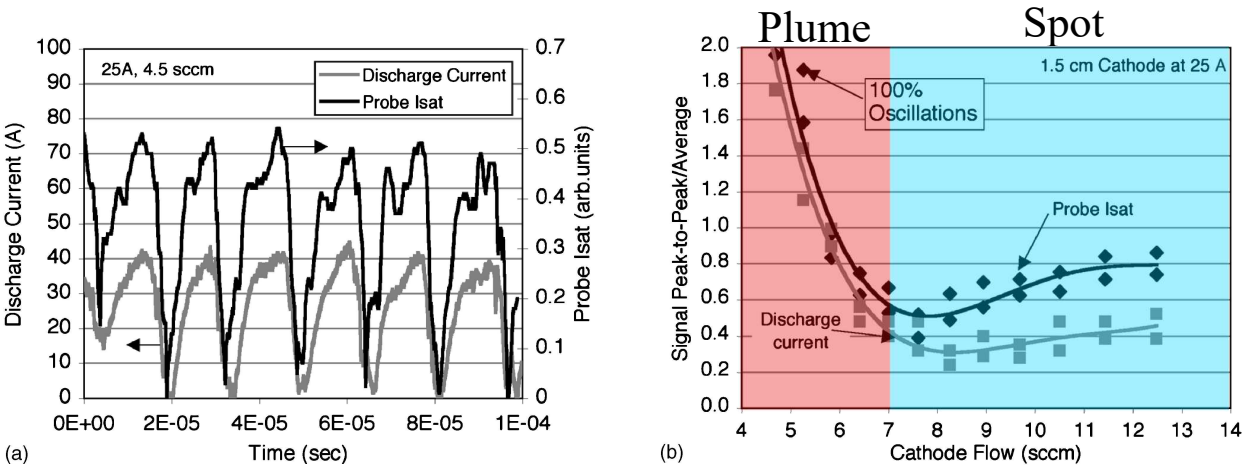

Figure 2.4: Illustration of a typical discharge current oscillation (a) and a stability map for a hollow cathode showing how discharge current fluctuations change with varying flow rate (b). Reproduced with permissions from AIP Publishing Ref. [2].

mode to ionization processes. Furthermore, the plasma instability's greatest amplitude is co-located with a seemingly self-organized plasma structure, the so-called "plasma ball," that appears downstream of the keeper electrode. This phenomenon is shown in Fig. 2.5. These plasma potential oscillations, which can exceed the discharge voltage, were used to explain the presence of energetic ions that cause erosion. Although the deleterious effects and properties of this wave have been measured, the exact nature of the instability still remains unknown. Therefore if a cathode needs to operate stably for long durations, one typically measures the so-called plume margin curve (Fig. 2.4 (b)) and operates the device at moderate currents and flow rates to avoid the increased erosion from the plume mode instability.

This low-frequency plume mode wave (supposedly ionization related) can be readily observed in high-speed probe measurements of hollow cathodes. Work from Ref. [3], reproduced in Fig. 2.6, shows the Fourier transform of an ion saturation current probe signal. Here, the Fourier transform represents the relative amplitude of the plasma plane waves at frequency, f. This analysis shows the existence of low frequency oscillations, with a relatively coherent peak around 100 kHz, and high-frequency broadband waves above 200 kHz. This lower-frequency mode is associated with the ionization-like wave observed when operating

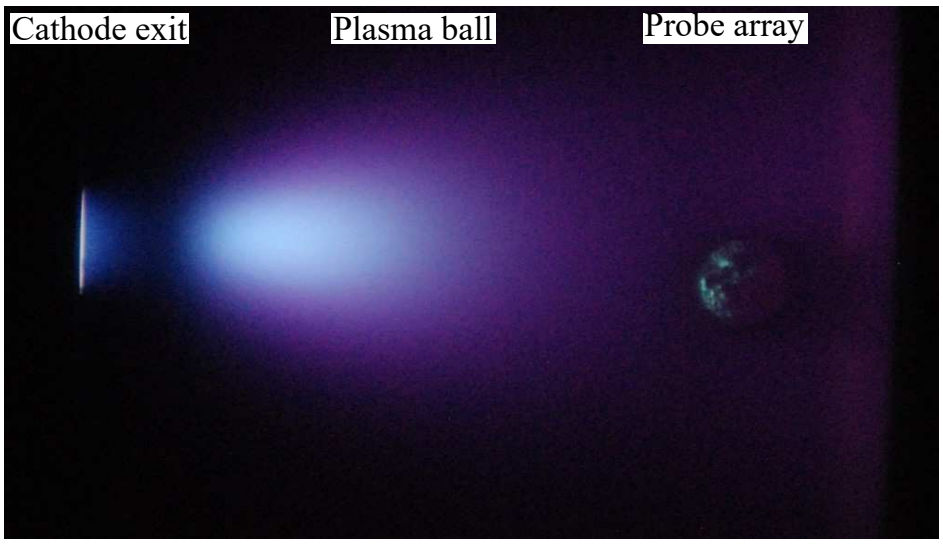

Figure 2.5: Formation of the coherent "plasma ball" structure associated with the plume mode ionization wave.

a cathode in plume mode. When the plume mode wave reaches larger amplitudes, multiple harmonics of this fundamental frequency can be excited, indicating nonsinusoidal structure of the oscillation. The higher-frequency modes are linked to another form of instability referred to as ion acoustic turbulence (IAT) that is also known to propagate in the plume of hollow cathodes. Typically in a spot mode discharge, the amplitude of the ionization-like plasma wave is relatively small compared to the turbulence. We will return to a more complete discussion of the turbulence in later sections.

To summarize, this early experimental work exposed several key properties and trends about the plume mode wave. First, its low-frequency (between 10 and 100 kHz) was connected with ionization and possibly undergoes a form of predator-prey like process between electrons and neutrals. In addition, the formation of energetic ions that lead to cathode erosion were linked to the presence of the large plasma potential fluctuations. Lastly, the onset of the wave was identified empirically to scale with the discharge current, and inversely with mass flow rate. Together, these results are the experimental starting point from which we aim to acquire new insight for this poorly understood process.

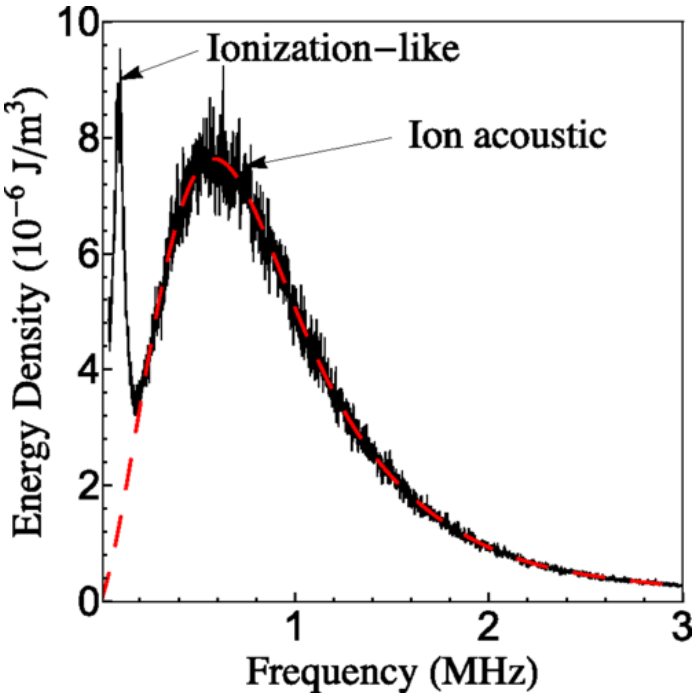

Figure 2.6: Fourier transform of plasma waves in a hollow cathode plume for high-power Hall thrusters showing ionization-like waves and broadband ion acoustic waves. [3]

2.4 Existing Theories for the Plume Mode

Understanding this mode transition has been a long standing question for the plasma propulsion community. There have been several attempts to describe this behavior. Some have proposed that the wave is an ionization instability [2,37] due to predator-prey action between electrons and neutral atoms; however, no analytical stability criterion has been identified for this mechanism. Numerical simulations of predator-prey oscillations in Hall thrusters [38,39] have proposed that electron temperature fluctuations can drive them unstable; however, there is no clear mechanism for this to occur in hollow cathodes. Others have suggested it is born out of a current imbalance in the anode sheath [40]. If the current collected by the anode is larger than the thermal current, then the electrons are accelerated at the sheath leading to the characteristic enhancement in light emission; however, it is unclear how this relates to the discharge current and keeper voltage oscillations. The onset criterion for this

phenomenon is [40]

$$\frac{I_{dc}}{I_{e,th}} = 4\pi^{3/2}\frac{I_{dc}}{I_{i,th}}\frac{r^2}{A_a}\sqrt{\frac{m_e T_i}{m_i T_e}}\ , \tag{2.1}$$

Where I_{dc}, $I_{e,th}$, and $I_{i,th}$ are the discharge, electron thermal, and ion thermal currents, respectively and T_e and T_i are the electron and ion temperatures. The electron and ion masses are m_e, and m_i, respectively. A_a is the anode area and r is the cathode orifice radius. Moving striations, [41–45] (waves of stratification i.e. ionization waves) are another contender for describing the observed structure. This type of ionization wave forms in DC positive column discharges and is the result of a kinetic resonance between the electron energy distribution function and spatially periodic electric fields. [46] Electrons are accelerated by the electric field until they achieve sufficient energy to ionize the neutral gas, generating slow electrons for the cycle to repeat. Striations, however, usually manifest themselves as backward waves, i.e. the dispersion relation follows $\omega k \propto c$, which early wave propagation measurements of the plume mode do not support. [47] Furthermore, striations tend to occur at higher pressures than we typically expect in the plume of a cathode discharge. Lastly it has been proposed that the plume mode oscillation is the result of nonlinear behavior in the underlying ion acoustic waves forming an ion acoustic soliton. [48] Although existing theory for these nonlinear waves [49–52] qualitatively describes the waveforms produced by the instability, the length-scale of the "plasma ball" is several orders of magnitude too large, given the plasma densities, for it to be described by a soliton. Overall, there has yet to be a consensus on the type of wave that describes the plume mode instability. Furthermore, there is still no clear physical description for the nature of the wave nor does there exist an analytically derived stability criterion that can predict its characteristic features and onset.

2.5 Review of Hollow Cathode Simulations

Along with predicting the hollow cathode spot-to-plume mode transition, there are several other poorly understood processes that have made the numerical modeling of these devices challenging. The need for a self-consistent simulation of the cathode plasma comes from the strong desire in the electric propulsion community for design and flight qualification through numerical modeling. However, there are obstacles to building up these capabilities. One could use a particle-in-cell (PIC) code to directly simulate the trajectories of electrons, ions, and neutral particles through all three regions of the device. [53] However, given the dramatic change in density across the length of the plasma, one would be required to use very short time steps to capture the electron dynamics but also a long time to resolve these low-frequency modes. Such calculations quickly become intractable, therefore many modeling efforts have focused on reduced-order, fluid simulations of the device. [54–57] These fluid models are highly-successful in capturing the physics of the internal cathode plasma, where the densities are very high, collisions a frequent, and the underlying assumptions, for example a Maxwellian plasma, are generally met. Beyond the orifice, however, the density drops by several orders of magnitude and the plasma becomes collisionless, in which case those same assumptions may not apply. Historically, it has been a challenge for continuum simulations to capture the experimentally observed trends in this region. Below, we first discuss the recent progress that has been made for modeling of the hollow cathode plume and how these efforts have informed our investigation of the plume mode instability.

Historically, a key challenge for fluid modeling of hollow cathodes is predicting the plasma potential profile of the plume region. In other words, although the plume is essentially collisionless some non-classical process is enhancing the resistance of the plume and driving up the potential. Figure 2.7 shows the results of one of these simulations where the predicted plasma potential profile using Coulomb collisions, shown as solid lines with open symbols, is in stark disagreement with experimental measurements. As a solution to this problem, it was posited that the large currents produced by hollow cathodes could drive ion acoustic

waves in the plume. [4, 15, 58, 59] These turbulent waves grow at the expense of the electron drift velocity and therefore they can collectively act as an effective drag force on the electron fluid. This is frequently interpreted as the IAT anomalously raising the resistivity of the plasma. This kind of non-classical behavior can be implemented into fluid codes through various approximations on the nature of the turbulence. [55–57, 60] For example, higher fidelity simulations that include such effects, like those shown by the solid and dashed lines in Fig. 2.7, are able to better capture the shape of the experimentally observed plasma potential when empirical scaling factors are appropriately tuned for the resistivity. Later experimental measurements confirmed the presence of this turbulence (see Fig. 2.6) and good agreement was shown between theory and experiment for the growth and propagation of these modes. [3, 61]

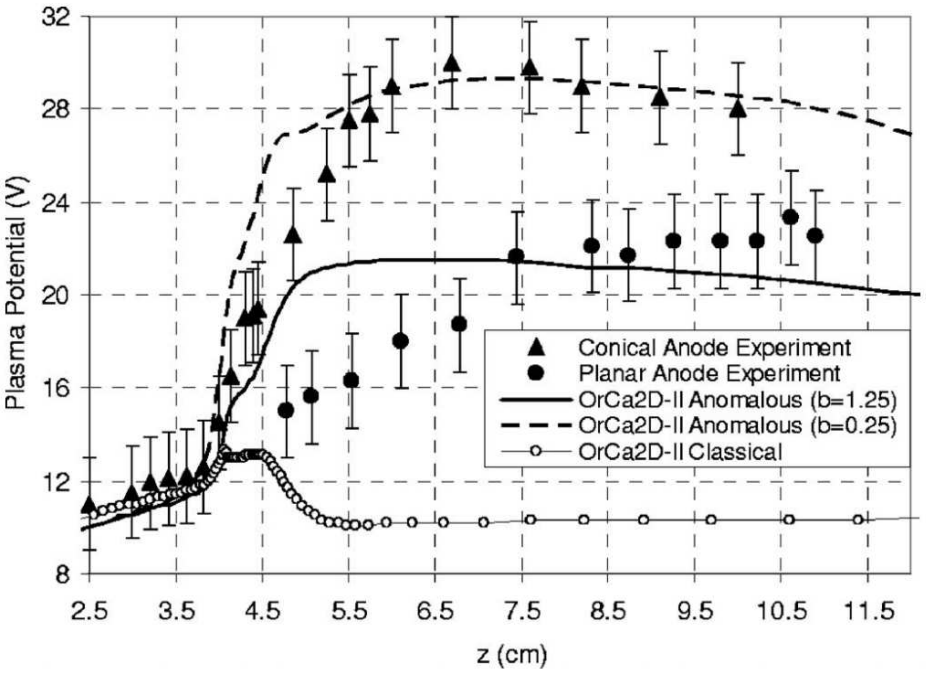

Figure 2.7: A comparison of simulations and experiments showing the need for non-classical resistivity in the plume to account for observed changes in potential. Reproduced with permissions from AIP Publishing in Ref. [4]

In addition to high fidelity predictions of the time-average plasma parameters, the inclusion of these wave-driven effects in some cases led to the formation of low-frequency

oscillation in the plume. These waves were reminiscent of experimental measurements of the plume mode instability. This crucial finding made the connection between anomalous, wave-driven resistivity in the cathode plume and the coherent, low-frequency oscillation of the plume mode. Two such high-fidelity numerical codes have produced large-scale oscillations that originate in the cathode plume, however, the interpretation of the results has differed. For example, *Sary et. al.* claim that the phenomenon is primarily a result of periodic saturation of the turbulent energy density and is unrelated to ionization, contrary to previous descriptions. [56, 57] There is, however, no experimental validation for this simulated result. A separate model by *Mikellides et. al.* also found large plasma density oscillations that originate in the plume. They noted that the onset of this wave is somehow connected to the enhanced Ohmic heating of the electrons by IAT. [62] The simulation was compared with experimental measurements of the so-called "plume margin" curve (see Fig. 2.4 (b)), a characteristic curve of keeper voltage oscillations with varying mass flow rate to the cathode. This comparison between simulation and experiment is shown in Fig. 2.8. The numerical calculation found good agreement with the experiments. Overall, there is no consensus on the precise nature of the plume mode instability; however, it is clearly linked to the presence of turbulence in the cathode plume.

In summary, the plasma state of the hollow cathode plume is driven by the non-classical effects of IAT. These processes are thought to play an important role in the onset of the low-frequency wave that is associated with the hollow cathode plume mode transition. It is unclear, however, if the turbulence is providing an inherently new mechanism for instability to arise or if it simply influences the plasma parameters such that a classically derived wave goes unstable. In the following sections, we examine the properties and effects of IAT more closely with the eventual goal understanding how it might play a role in the formation of the plume mode instability.

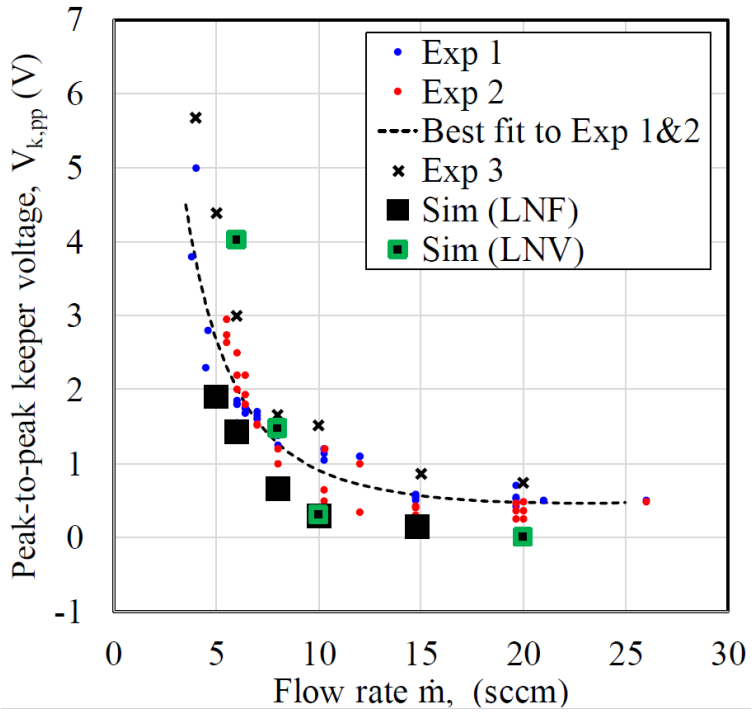

Figure 2.8: Hollow cathode plume margin from Ref. [5], reproduced with permission.

2.6 Ion Acoustic Turbulence

Given the importance of wave-driven effects in establishing the steady state plasma properties of the hollow cathode plume, here we discuss the relevant theory of IAT and its effects on the background plasma.

2.6.1 Dispersion

The propagation and growth of IAT can be derived from the Boltzmann equation for electrostatic interactions between charged particles through a linear analysis. [63] The resulting dispersion relation is given by

$$\omega_r = \frac{kc_s}{\sqrt{1+(k\lambda_D)^2}} + ku_i \tag{2.2}$$

$$\omega_i = kc_s\left(\frac{u_e-(u_i+c_s)}{v_e} - \left(\frac{T_e}{T_i}\right)^{3/2} e^{-T_e/2T_i}\right) - \frac{1}{2}\nu_{i,n}\ , \tag{2.3}$$

where $c_s = \sqrt{T_e/m_i}$ is the ion sound speed, λ_D is the Debye length, k is the wavevector, $u_{e,i}$ are the electron and ion drift velocities, respectively, $T_{e,i}$ are the electron and ion temperatures, and ν_{in} is the ion-neutral collision frequency. To arrive at this expression, several assumptions are made about the velocity and frequency hierarchy in the plasma. These are discussed at length in Ref. [63]. Physically, the first term in Eqn. 2.3 indicates that the electron drift velocity is the source of energy for the growth of the wave. This occurs through the process of inverse Landau damping, where electrons that are resonant with the wave are able to collisionlessly transfer energy leading to growth. The second term is the result of ion Landau damping, the same effect as the electrons, but where the ions are extracting energy from the wave. The last term represents additional damping of the turbulence as a result of collisions between ions and neutral gas. As shown in previous works (see Ref. [61]), the frequencies that are excited in the cathode plume are well below the ion plasma frequency i.e. $k\lambda_D \ll 1$, and the electron velocity is large compared to the ion sound speed, so we simplify these terms to

$$\omega_r = k\left(u_i + c_s\right) \equiv k v_g \tag{2.4}$$

$$\omega_i = k c_s \frac{u_e}{\nu_e} \equiv k c_s M_e, \tag{2.5}$$

where v_g is the group velocity and M_e is the electron Mach number. These characteristics are valuable for assessing if the waves we observe are indeed IAT as well as for estimating the collective effect of these waves on the plasma.

2.6.2 Anomalous Resistivity

From the dispersion relation, we identify the energy source of the instability to be the electron drift velocity relative to the ions. The waves are damped by the ion Landau damping and collisions between ions and neutrals. Consider this collisionless interaction in the context of conservation of momentum in the frame of the ion wave. Electrons that are moving quickly

with respect to the wave, i.e. $u_e - |u_i + c_s| > 0$, will donate some of their momentum to the wave by way of electric fields. Conversely, electrons that are moving slowly extract momentum from the wave. This is shown graphically by Fig. 2.9. If there are relatively many fast electrons then the wave will grow. This process is often called inverse Landau damping. By this conservation of momentum argument, we can construct an effective rate of momentum transfer from the electron fluid to the ion acoustic waves. The rate of change in the electron momentum density and the wave momentum density are given by [64]

$$\frac{\partial p_e}{\partial t} = n m_e u_e \nu_{an} \ , \ \frac{\partial p_k}{\partial t} = \frac{W_k}{v_g} \gamma_e. \tag{2.6}$$

Here, ν_{an} is the anomalous (effective) momentum transfer frequency between the electrons and the wave. In the second part of Eqn. 2.6, p_k and W_k are the wave momentum density and energy density while γ_e is the electron contribution to the growth rate i.e.

$$\gamma_e \simeq k c_s M_e \ . \tag{2.7}$$

Combined these expressions indicate that modes with greater energy densities and growth rates result in a larger momentum transfer rate. It can be shown that the wave energy density of the IAT is given by [63]

$$W_k = \frac{\omega_r}{k c_s} n_e T_{e0} \left(\frac{q \phi_k}{T_e} \right)^2 \ , \tag{2.8}$$

where ϕ_k is the amplitude of a single electrostatic potential oscillation with wavevector k associated with the IAT. Physically, Eqn. 2.8 tells us that the energy held in ion acoustic waves scales with the thermal energy density of the plasma. Combined with Eqns. 2.6 and 2.7, we find that modes with greater amplitude can more rapidly extract momentum from the electron fluid. Considering that momentum is conserved between the electrons and all the waves in the IAT spectrum (i.e. setting the two parts of Eqn. 2.6 equal to each other) we

need to calculate the sum over the IAT modes. However, without a closed form expression for the wave amplitude for a given wavenumber, it is common to assume that $W_k \propto k^{-\alpha}$. Under this assumption and applying the dispersion relation of ion acoustic waves, the anomalous collision frequency at which electrons transfer momentum and energy to the IAT can be approximately given by [64]

$$\nu_{an} \propto \frac{W}{nT_e}\omega_{pe} \ , \tag{2.9}$$

where $W = \sum_k W_k$ is now the total wave energy density of the IAT spectrum and ω_{pe} is the electron plasma frequency. Physically, Eqn. 2.9 indicates that the greater the energy density of the turbulence relative to the thermal energy density, the greater the effective collision rate. From a fluid perspective, this term can be added to the electron-ion collision frequency, enhancing the collisionality of the plume. This result ultimately has two global effects on the plasma. First, it increases the resistivity of the plasma causing the characteristic potential rise in the plume, as is observed in Fig. 2.7. Second, in keeping with the idea of greater resistance in the plume, there is enhanced Ohmic heating of the electrons that leads to higher temperatures.

As has been observed in experiment [3,65–67] the effects of the turbulence tend to totally dominate the steady state characteristics of the cathode plasma. However, an important question for numerical simulations is how to account for the fact that the problem is not closed, i.e. we don't know a priori the wave spectrum. This brings to light an important distinction between the two high-fidelity numerical models identified in Sec. 2.5. They use different closure models for the IAT, i.e. they model W in different ways. *Mikellides et al.* [5] use a saturated model for W, such that the anomalous collision frequency is given by

$$\nu_{an} = \alpha_{IAT}\omega_{pe}\frac{T_e}{T_i}M_e \ , \tag{2.10}$$

where α is a constant that depends on saturation mechanism for the waves, and is typically

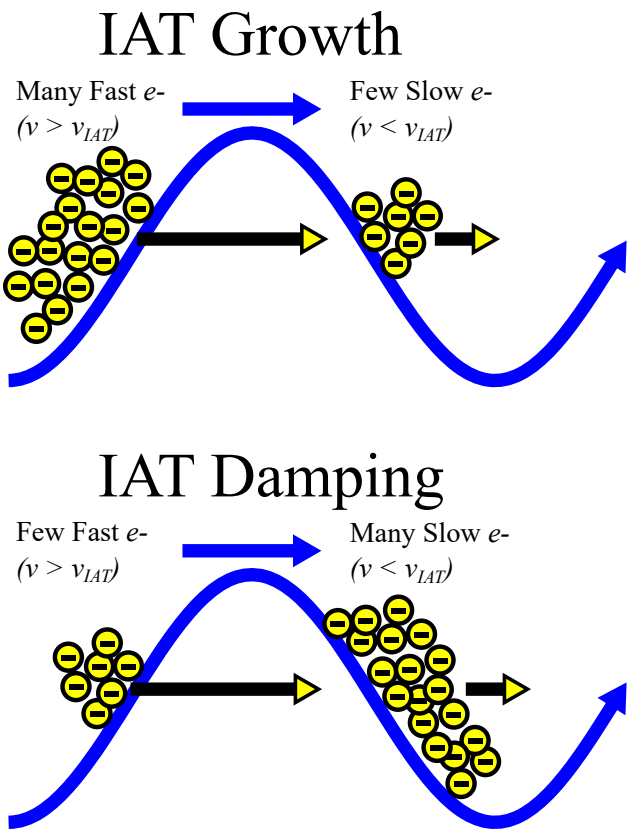

Figure 2.9: IAT growth process through a resonance between the wave and drifting electrons.

$\mathcal{O}\left(10^{-2}\right)$. This is an implementation of the work of Sagdeev, where the IAT is assumed to saturate through non-linear ion Landau damping. Using this idealized model greatly simplifies the simulations and in several cases produced results that agree with plasma measurements. [4] However, the agreement degraded when applied to higher current discharges. It was postulated that under these conditions that capturing the growth of the waves was critical and so the the model was extended to capture this effect. [55–57, 68] These newer codes allow for propagation and growth of the waves by using the wave kinetic equation [69] to conserve the wave energy density of the IAT. This is written as [63]

$$\frac{\partial W}{\partial t} + \nabla(v_g W) = \omega_{pi} W \left(\frac{u_e - (u_i + c_s)}{v_e} - \left(\frac{T_e}{T_i}\right)^{3/2} e^{-T_e/2T_i} \right) - \frac{1}{2}\nu_{i,n} \ . \tag{2.11}$$

This additional conservation equation, along with Eqn. 2.9, allows the evaluation of the

anomalous collision frequency.

Since there are conflicting interpretations and varying implementations coming from numerical simulations, in Chapter 4 we will investigate the necessary physics for capturing these plume mode oscillations by modifying expressions for the anomalous collision frequency in our analytical theory.

2.7 Approach

Subject to the insights that have emerged from the numerical and experimental work summarized in the above sections, we make the hypothesis that the plume mode wave can be described by the classical three-fluid equations for the quasi-neutral plasma and neutral gas with additional terms that include non-classical resistivity:

$$
\begin{aligned}
\frac{\partial n}{\partial t} + \nabla \cdot (n u_i) &= n \nu_{iz} \text{ (ion continuity)} \\
\frac{\partial n}{\partial t} + \nabla \cdot (n u_e) &= n \nu_{iz} \text{ (electron continuity)} \\
\frac{\partial n_n}{\partial t} + \nabla \cdot (n_n u_n) &= -n \nu_{iz} \text{ (neutral continuity)} \\
m_i \frac{\partial n u_i}{\partial t} + m_i \nabla \cdot (n u_i u_i) &= nqE - n m_e (u_e - u_i)(\nu_{an} + \nu_{ei}) \\
&\quad + n m_i (u_i - u_n) \nu_{in} - \nabla (n T_i) \text{ (ion momentum)} \\
m_e \frac{\partial n u_e}{\partial t} + m_e \nabla \cdot (n u_e u_e) &= -nqE - n m_e (u_e - u_i)(\nu_{an} + \nu_{ei}) \\
&\quad + n m_e (u_e - u_n) \nu_{en} - \nabla (n T_e) \text{ (electron momentum)} \\
\frac{3}{2} \frac{\partial n T_i}{\partial t} + \frac{5}{2} \nabla \cdot (n u_i T_i) - u_i \cdot \nabla (n T_i) + \kappa_i \nabla^2 T_i &= n m_e u_e \left((u_e - u_i)(\nu_{an} + \nu_{ei}) + (u_i - u_n) \nu_{in} \right) \\
&\quad + Q_i \text{ (ion energy)} \\
\frac{3}{2} \frac{\partial n T_e}{\partial t} + \frac{5}{2} \nabla \cdot (n u_e T_e) - u_e \cdot \nabla (n T_e) + \kappa_e \nabla^2 T_e &= n m_e u_e \left((u_e - u_i)(\nu_{an} + \nu_{ei}) + (u_e - u_n) \nu_{en} \right) \\
&\quad - n \epsilon_{iz} \nu_{iz} + Q_e \text{ (electron energy) .}
\end{aligned}
\tag{2.12}
$$

The subscripts i, e, n indicate the ion, electron, and neutral quantities, respectively. The particle masses, densities, velocities, and temperatures are given the variables m, n, u, T, respectively. The ionization, Coulomb collision, ion-neutral collision, electron-neutral, and anomalous collision frequencies are ν_{iz}, ν_{ei}, ν_{in}, ν_{en}, ν_{an}, respectively. The coefficient of heat conduction is κ and ϵ_{iz} is the first ionization energy of xenon. The form of these equations is rather complicated and likely can be simplified while still capturing the physics driving the oscillation. Our approach in the following is first to experimentally characterize the properties of the instability to understand the relationships between these quantities and which ones, on physical grounds, may be neglected. Following this, we employ a simplified version of the governing equations, guided by experiment, to arrive at a physically-intuitive and first-principles derivation of the governing equations for the instability.

2.8 Problem Statement

From this body of work arises the following state of knowledge about the spot-to-plume mode transition and associated ionization-like instability. The wave tends to onset at higher currents and lower flow rates. It generates large plasma potential oscillations that are thought to be ionization related and creates energetic ions that enhance the erosion of plasma facing surfaces. In attempting to produce higher fidelity cathode models, numerical simulations indicated that the presence of IAT may be intrinsically linked with the transition to plume mode and the onset of the oscillation. Furthermore, the success of fluid simulations implies that this instability can be captured in a fluid framework. Moving forward, through this work we seek to answer the following questions about the onset of the wave:

1. What is the structure of the plume mode oscillation?
2. Is the wave actually related to ionization?
3. How is IAT connected to the wave? Does it drive temperature fluctuations and does it vary on the time scale of the cathode mode?

4. What is the energy source for driving this wave unstable?

5. Can we derive a self-consistent theory for the instability?

6. Does the onset criterion predict the experimentally observed onset of the wave?

7. Will this phenomenon be observed in cathodes operating in Hall thrusters?

These questions are examined in this dissertation through theory and experiment. The following Chapters are devoted to the experimental and theoretical investigation of this plume mode oscillation and an eventual evaluation of our theory.

2.9 Conclusion

In this Chapter, we presented the current state of understanding for the low-frequency, coherent, plume mode oscillation. Phenomenologically, it has been suggested that this wave is ionization related; however, there is only sparse experimental corroboration to support this claim. Numerical simulations have linked the formation of the plume mode wave to the presence of IAT, notably the enhanced Ohmic heating of the electrons. With this information, we have synthesized the known features of the instability and translated them into a general fluid framework that is, however, too complicated to analyze. This has set the stage for our following experimental Chapter, where we conduct an initial investigation of the plume mode to identify key characteristics of the wave and possible simplifying assumptions to aid in the development of the theory.

CHAPTER 3

Exploratory Measurements of the Plume Mode Oscillation

3.1 Introduction

The goals of this Chapter are to experimentally examine the relationship between the fluctuating properties associated with the instability and then to identify any simplifying assumptions that can be employed to reduce the complexity of Eqns. 2.12. To this end, we first conduct an experiment using a high-speed camera to image the plasma. The results of this experiment set the stage for a second investigation that examines the connection between the IAT and the plume mode oscillation (a notable hypothesis that has stemmed from numerical work that we explore experimentally is the connection of IAT to the plume mode wave) using electrostatic probes. Here, our aim is to show that the IAT indeed varies on the time-scale of the plume mode wave. Lastly, we use a collection of probes to link fluctuations in the IAT wave energy with changes in the collision frequency and with electron temperature oscillations. Altogether, these experiments will tackle the first three questions of our problem statement:

1. What is the structure of the plume mode oscillation?

2. Is the wave actually related to ionization?

3. How is IAT connected to the wave? Does it drive temperature fluctuations and does it vary on the time-scale of the cathode mode?

The results are then interpreted to devise a possible mechanism for instability.

3.2 High-speed Imaging

Here we discuss the high-speed imaging experiment used to show the spatiotemporal structure of the plume mode instability. First we describe the experimental methods used to acquire the data. Then we present the results and analyze them in search of simplifying assumption for our theory. Lastly, we summarize our findings with concluding remarks.

3.2.1 Experimental Methods

For this experiment, we used a 20 A LaB_6 hollow cathode with a 3 mm tungsten orifice and a graphite keeper electrode. We varied the xenon mass flow rate to the device between 15 and 5 sccm to observe the mode transition (as in Fig. 2.8). The anode was placed 40 mm downstream of the cathode exit and the discharge current was also varied between 10 and 25 A. The cathode test facility base pressure was 0.7 μTorr, which is achieved by cryogenic pumping. During the experiment the background pressure in the facility was between 50 and 500 μTorr-Xe, depending on the operating condition. We used the Photron Fastcam SAZ high-speed CCD camera to image the plasma at 700 kfps through an acrylic viewport located perpendicular to the plasma discharge, allowing us to observe axially propagating oscillations, and a similar viewport on axis to see the radial evolution of the mode. The experimental setup is illustrated in Fig. 3.1, indicating the positions of the various experimental components.

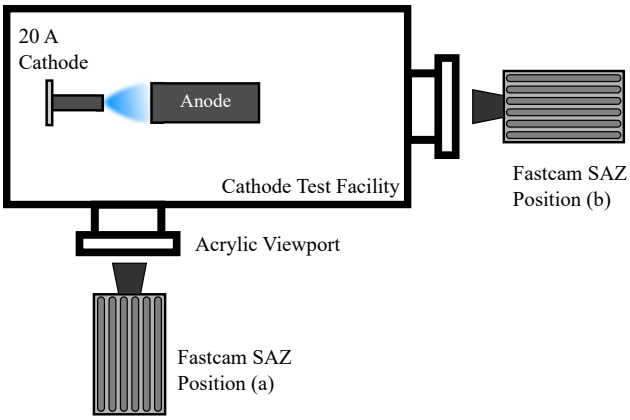

Figure 3.1: Experimental setup for the high-speed camera measurements of cathode oscillations.

3.2.2 Results

Figure. 3.2 (a) shows a full cycle of oscillation for the plume mode instability captured from the high-speed camera when it was placed perpendicular to the discharge axis. Here, we have saturated the image to better show the structure of the wave. The cathode exit can be seen as the consistent bright spot on the left hand side of the image. The anode sits on the right hand side. What we see is a relatively localized structure that forms in the plume, near the cathode. The formation grows quickly, then slowly dissipates as it propagates towards the anode. By tracking the cathode side of the wave front propagation we find that the wave travels at around 1.1 km/s until it reaches the anode. Then, the structure begins to reform near the cathode at the same location after about 20 μs. This 50 kHz periodicity is the same as what is observed in the discharge current (see Fig. 2.4) therefore the changes in light intensity are likely related to the processes that cause the discharge current oscillation. Figure. 3.2 (b) shows the oscillation when placing the camera along the axis of the discharge. The asymmetry in the images is likely because of a slight mis-alignment of the camera. Note the images are are not taken simultaneously. We have phased the sequence of images such that the dimmest frames are synced. Together, Figs. 3.2 (a) and (b) indicate that the plasma ball structure propagates in the axial direction and diffuses radially as it moves towards the anode.

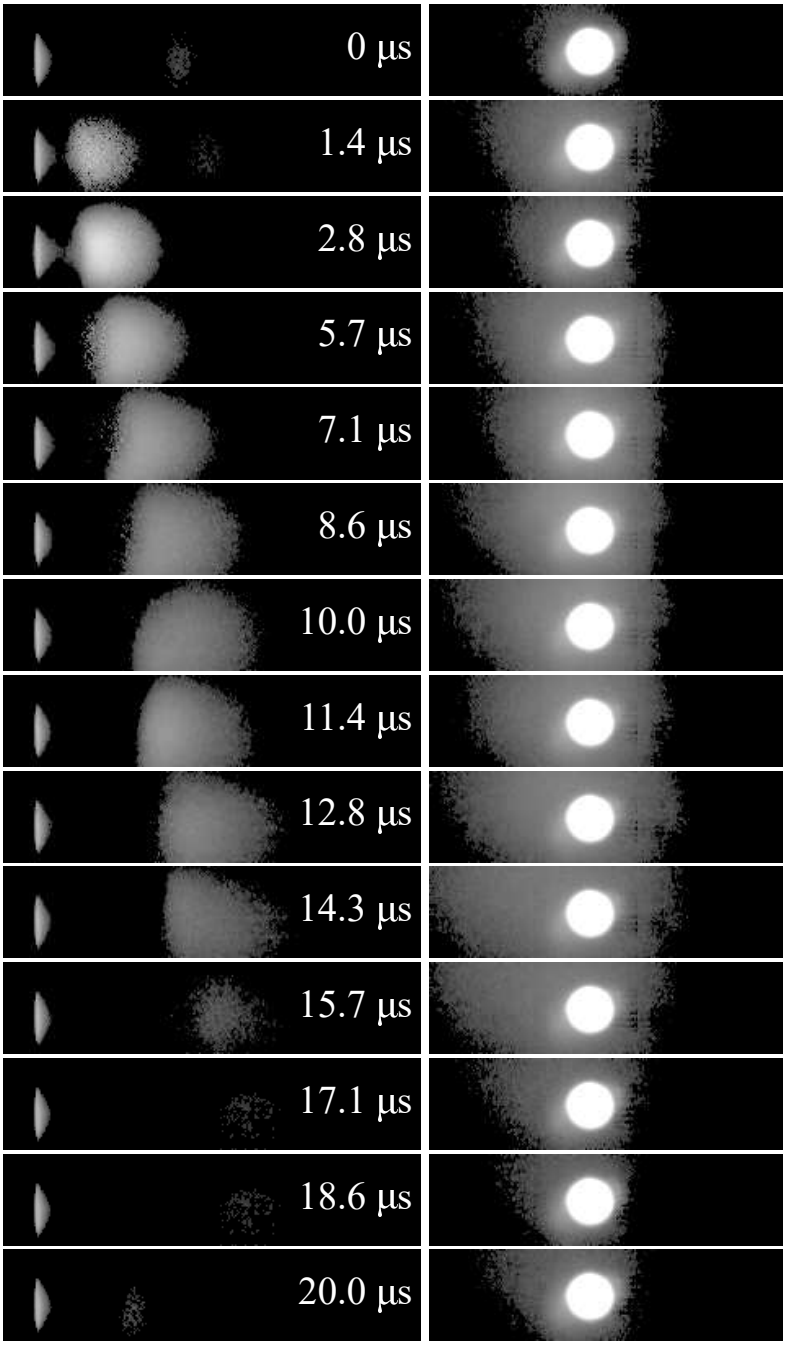

Figure 3.2: High-speed camera images of the plume mode instability at 20 A discharge current and 6 sccm Xe. We show a full cycle of the oscillation captured at 700 kfps, which is around 50 kHz. Images are saturated to show detail. (a) Fastcam position (a), (b) Fastcam position (b)

3.2.3 Discussion

The images have revealed that the increased brightness of the plasma in plume mode is not a steady-state process, but rather a highly periodic and localized phenomenon. We find that the wave propagates in the axial direction, appearing to be convected out from an "active region" at the ion velocity. As the wave propagates downstream of the region where the coherent plasma ball forms the light intensity decreases. This effect is likely due to the density gradient in the plume. This points to diffusion of the plasma possibly playing an important role in the evolution of the wave.

In addition to identifying diffusion as a potentially important process, these images also provide insight for how we can simplify the problem of determining an analytical onset criterion for the instability. We see that the phenomenon is highly localized in the plume. Specifically, it forms periodically at a fixed location and then diffuses as it propagates towards the anode. This relatively low velocity is characteristic of the heavy particle species and suggests that the oscillation can perhaps be described in a 0 dimensional framework where the wave is formed locally and is convected out by the flow of the ions and neutrals. This observation will play an important role in simplifying our theoretical analysis of the instability.

Lastly, we analyze the fact that the plume mode instability is generating large amounts of light, periodically. For xenon, we can model the light intensity, $\mathcal{I}$, as [47, 70]

$$\mathcal{I} \simeq n n_n \sigma_0 \sqrt{T_e} e^{-\frac{\epsilon}{T_e}} \left(1 + \frac{\epsilon}{T_e}\right) , \tag{3.1}$$

where σ_0 is the excitation cross-section for xenon and ϵ is the threshold energy for excitation. We see that fluctuations in light emission are the result of variations either the densities, electron temperature, or both. The ionization rate is given also depends on these parameters and therefore we expect that changes in light emission are highly correlated with ionization fluctuations. As IAT is the known dominant form of electron heating in the plume, it is

possible that if there indeed are temperature fluctuations, then there is a correlation between the light emission and the wave energy of the IAT.

3.2.4 Conclusion

In summary, the high-speed camera experiment indicates that the plume mode instability is a localized phenomenon, rather than a global one. There is a region of intense periodic light emission near the cathode that then appears to diffuse and propagate downstream towards the anode at a velocity that is on the same order as that of the ions an neutrals. This leads us to two important conclusions.

1. Diffusion likely plays an important role.

2. The periodic formation of the structure at a consistent location suggests that we can analyze this process in a 0 dimensional framework.

3.3 Dispersion of Plasma Waves & Correlation of Turbulence with the Ionization-like Wave

One of the key tenants that emerged from simulations is that the presence of IAT is necessary for the onset of the plume mode wave, possibly because it drives Ohmic heating of the electrons. This would suggest that both IAT amplitude and temperature may vary on the time-scale of the instability. In this section, we explore this potential link experimentally. Our goal is to elucidate the propagating nature of the instability and to explore the key hypothesis from simulations that it is correlated with IAT. To this end, we first describe the experimental setup and analysis techniques that we use to evaluate IAT and the plume mode wave properties. We then present the experimental results and discuss them in the context of the previous high-speed camera measurement and numerical simulations.

3.3.1 Experimental Setup

Figure 3.3 shows the experimental test configuration. For this investigation, we used 20-A BaO hollow cathode with a 3 mm tungsten orifice and a graphite keeper electrode [13]. The device was installed in a 1 m × 1 m vacuum chamber with an operating pressure of 20 μTorr at NASA Glenn Research Center (VF-56). The plasma discharge was established between the cathode and a cylindrical anode located a distance ℓ = 38 mm downstream of the cathode's exit. We operated the source at 22.5 A and 19.0 V with a 10 sccm flow-rate of xenon, a plume mode condition (see Fig. 3.5).

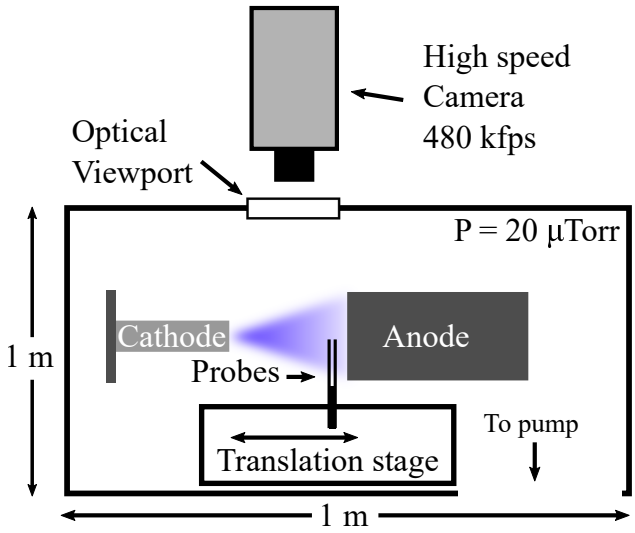

Figure 3.3: Experimental setup for measuring cathode oscillations with the high-speed camera measurements and ion saturation probes.

To measure both coherent (plume mode) and incoherent waves (IAT), we used two diagnostics, a high-speed camera and cylindrical Langmuir probes. The camera captured the characteristic fluctuations in light intensity of the plasma plume through an optical viewport. The images were acquired at 480 kfps. We measured ion saturation current oscillations in the plume of the cathode with a pair of ion saturation probes, a common technique for characterizing oscillations in low temperature plasmas [3, 61, 71–73]. These cylindrical probes, 3 mm long and 0.5 mm in diameter, were spaced 5.2 mm apart, oriented perpendicularly to the plasma flow, and biased to -50 V below ground using a collection of batteries. The

large-scale oscillations also drove variations in the total discharge current to the cathode, which we simultaneously measured. As outlined in the following sections, this latter signal served as a trigger reference for time-resolved analysis. Both the ion saturation and discharge current signals were acquired at 10 MS/s for 100 ms at each position using an oscilloscope.

3.3.2 Results

Below are the results of the experiment. First we present the time average plasma parameters. Then we examine the time average IAT and ionization wave propagation properties using a cross-correlation analysis. Lastly, investigate transient behavior in the IAT and compare it to the coherent component of the ion saturation current.

3.3.3 Time-averaged measurements

We show direct measurements of the time-averaged density and electron temperature with a swept and translating Langmuir probe in Fig. 3.4. The density decreased monotonically from $\mathcal{O}(10^{18})$ to $\mathcal{O}(10^{17})$ m^{-3} with distance from the cathode while temperature increased monotonically from $1.5{-}2.2{\pm}0.2$ eV. We note that this temperature is relatively low compared to other measurements of similar cathodes. [3] The Debye length was on the order of $1-10\,\mu$m and the ion plasma frequency was between $100-200$ MHz. These results are consistent with other measurements of time-averaged plasma parameters in hollow cathodes [2, 74]. The time-dependent properties we subsequently report fluctuate against this steady-state background.

3.3.4 High-speed imaging

Following the technique in Sec. 3.2, we show in Fig. 3.5 results for variations in light intensity measured with the high-speed camera. These image stills show similar behavior to our previous results with this imaging technique. In particular, we can see that the oscillation

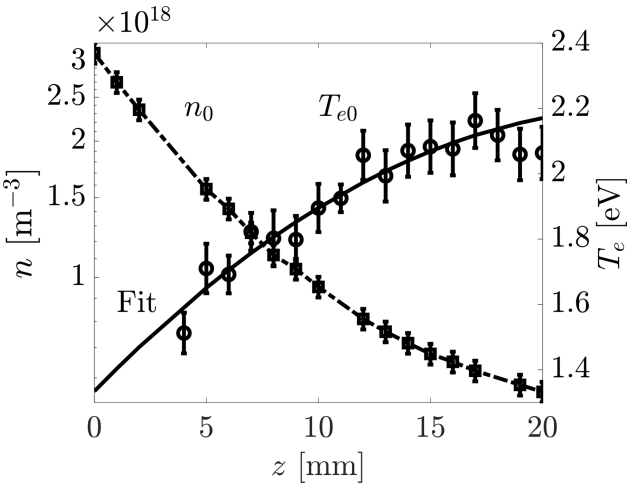

Figure 3.4: Steady-state density and electron temperature calculated from Langmuir probe traces. Position 0 [mm] is a the keeper surface (see Fig. 2.2)

appears to originate at a fixed spatial location near the cathode where light is periodically emitted at 36 kHz (a frequency also observed in the discharge current). It then propagates at 7 km/s towards the anode. This propagation speed is greater than the previous camera measurement by almost an order of magnitude; however, it is still relatively near the ion velocity as opposed to the electron drift, which on the order of 1000 km/s. Simulations [5] have also found similar wave velocities in comparable cathode configurations (with an applied magnetic field). Ultimately, this change in light intensity is indicative of relatively coherent density and/or temperature fluctuations in the plasma and is generally consistent with our previous measurements barring small changes that are likely due to differences in experimental setup and conditions.

3.3.5 Probe-based power spectra

To quantify this oscillatory behavior, we show in Figure 3.6 the power spectrum of the relative ion saturation current fluctuations, $(\tilde{I}/I_0)^2_\omega$, where I_0 is the time-averaged ion saturation current, $\tilde{I}$ is the fluctuation shown at three locations in the plume, and ω is the frequency. This figure indicates the presence of the two classes of instabilities that have been previously identified in the plasma generated by these cathodes: the low-frequency, coherent oscillations

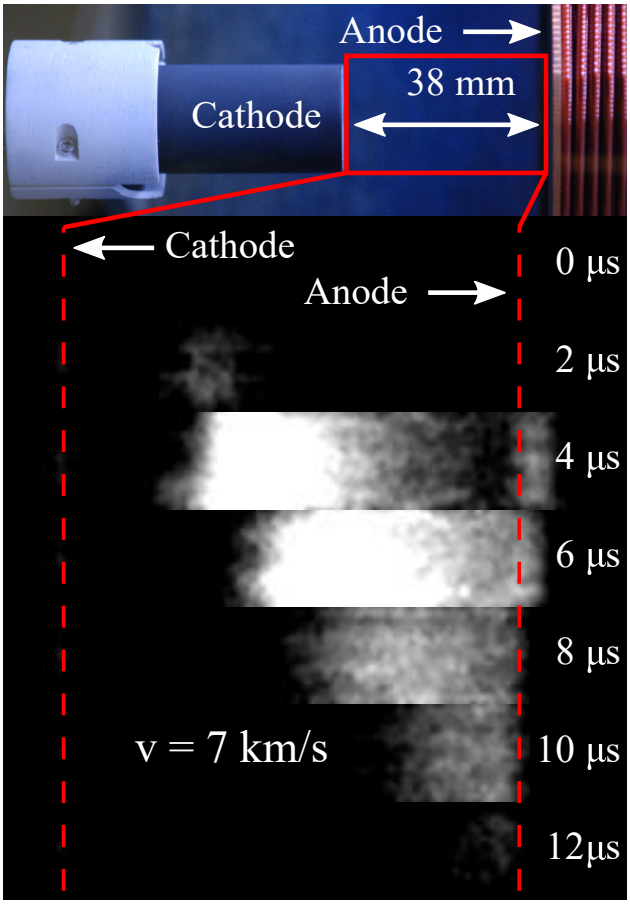

Figure 3.5: BaO hollow cathode in the vacuum facility. High-speed camera frames are captured at 480 kfps. One cycle of oscillation is 13 frames or ~ 36 kHz. 22.5 A, 10 sccm Xe.

of the plume mode instability and high-frequency, broadband waves that were linked with IAT [3,61,75,76]. Near the cathode, the plasma is dominated by the low-frequency oscillation. The spectrum is characterized by a series of monotonically decreasing harmonics with a fundamental frequency of $f_0 = 36$ kHz. This is indicative of the oscillation being non-sinusoidal. Downstream, the amplitude of the high-frequency oscillations (between 100 – 1500 kHz) rises. The dissipation of the wave amplitude at higher frequencies of these waves follows a power law dependence on frequency, with exponents between −1.5 and −2.7. These two trends are consistent with earlier work in Refs. [3, 61] on IAT in cathodes.

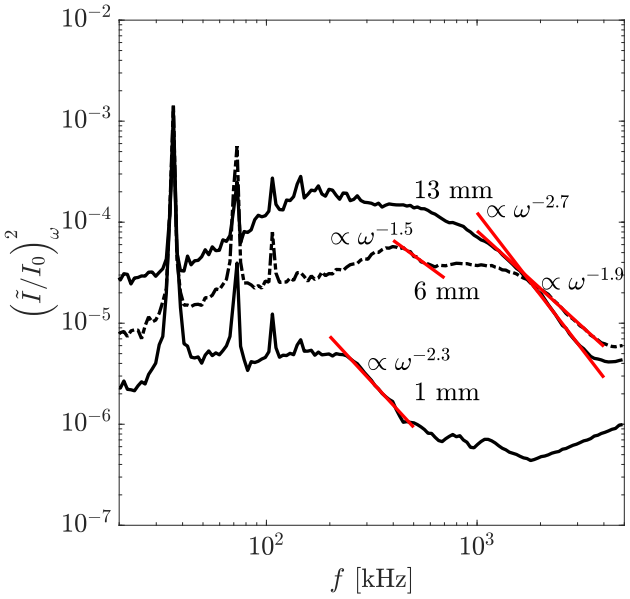

Figure 3.6: Power spectra of the ion saturation current at three positions in the plume showing turbulent waves and the coherent ionization instability. Curve fits show the frequency scaling for the dissipation of the turbulence.

3.3.6 Dispersion relations

To show that these high-frequency waves are indeed IAT, we use a cross-correlation technique [77, 78] to estimate the dispersion, $S(\omega, k)$, of the plasma and compare it to the quasilinear dispersion relation for current-driven IAT. Here, ω is the frequency and k is the wavenumber of a plane wave. This technique relies on taking a Fourier decomposition of the signals acquired from two spatially separated probes to estimate the wavenumber for each frequency in the spectrum. Explicitly, we calculate k using

$$k(\omega) = \frac{1}{\Delta x} \tan^{-1}\left(\frac{\Im\left(\mathcal{F}(\tilde{i}_{sat,2})\mathcal{F}^*(\tilde{i}_{sat,1})\right)}{\Re\left(\mathcal{F}(\tilde{i}_{sat,2})\mathcal{F}^*(\tilde{i}_{sat,1})\right)} \right), \tag{3.2}$$

We then bin the domain into frequency and wavenumber bins, 5 kHz and 20 m^{-1}, respectively, and assign the average Fourier amplitude to the bin. This calculation is conducted on 2000 data sets and averaged to elevate the signal above the noise. Ultimately, the analysis results in a two-dimensional histogram, in ω and k space, where the intensity is proportional to the

amplitude of each mode. [61, 78]

There are a number of physical and practical limitations to this approach in terms of the wavenumbers and frequencies that it can measure. For example, the ion saturation current can only be used to measure plasma fluctuations below the ion plasma frequency [79] and therefore we have restricted our measurements to frequencies an order of magnitude beneath this cutoff. We also note that the wavelength resolution of this probe technique is not capable of detecting waves smaller than the physical width of the probe (0.5 mm). Accordingly, we do not report measurements for wavelengths this small. Lastly, our technique can only unambiguously detect wavelengths greater than the probe spacing ($\lambda_{min} = 5.2$ mm $\rightarrow k_{max} = 604$ m^{-1}). Wavenumbers that exceed k_{max} are aliased, i.e. appearing as negative or smaller wavenumbers. Although this can lead to spurious results, we can under certain circumstances infer these potentially larger wavenumbers by extending the domain and using context to find patterns. We discuss the technique in greater detail in the following paragraph.

Keeping these caveats in mind, we use this technique to show in Figure 3.7 a dispersion plot at a location $z = 8$ mm downstream of the cathode. Physically, this figure is a statistical representation of the relative amplitude of propagating plane waves in the plasma at a given frequency and wavenumber. Here we note that we have corrected this plot for aliasing. This is done, following Ref. [61], by duplicating the dispersion plot, shifting the wavenumbers by $2\,k_{max}$, and concatenating the data set along the wavenumber axis. In Fig. 3.7 (a), the uncorrected measurement is highlighted in red. By extending the domain, patterns in the data emerge at higher frequency. We therefore take these modes to be shorter wavelengths spuriously aliased by our measurement technique.

The results from Figure 3.7 reveal properties of the two classes of oscillations we identified from the Fourier analysis in Fig. 3.6. First, we see that the high frequency modes exhibit a linear dispersion relation, i.e. a linear relationship between frequency and wavenumber. Moreover, the phase velocity of these higher frequency oscillations is given approximately by $v_{ph} = \omega/k = 4.0 \pm 0.5$ km/s. This value is commensurate with the ion sound speed in this

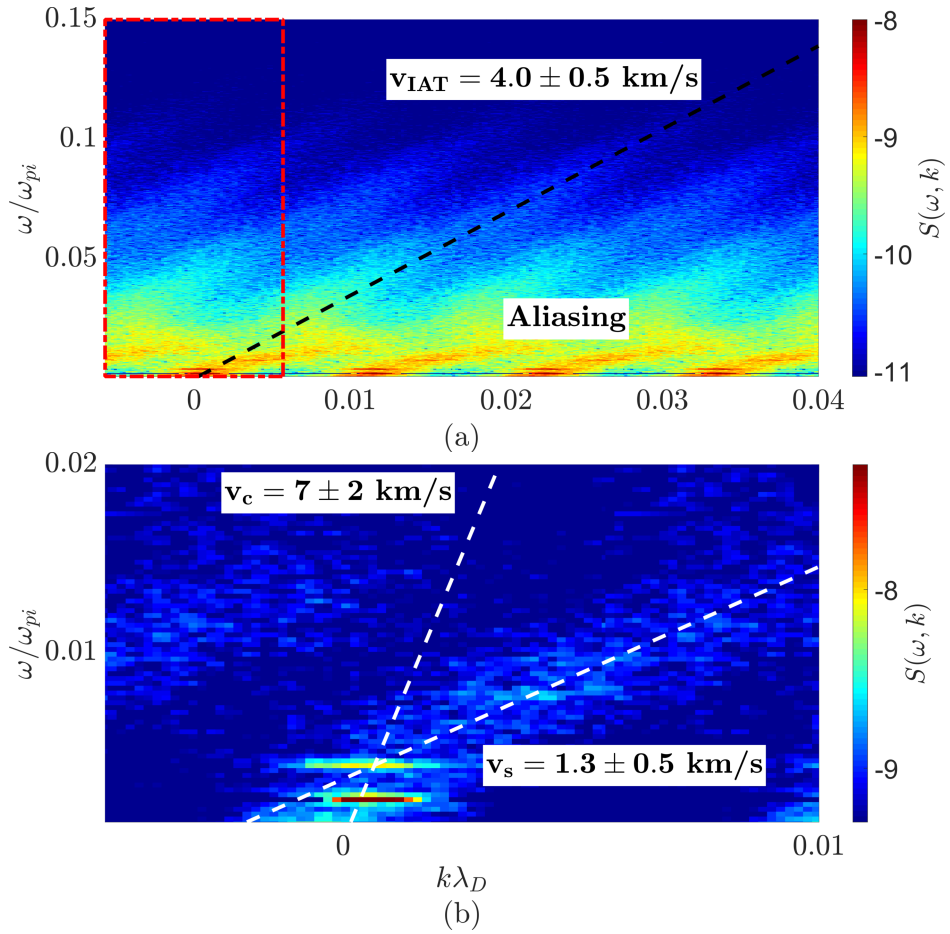

Figure 3.7: Measurement of the wave dispersion using cross-correlated ion saturation probes. Higher-frequency waves are anti-aliased by concatenating the data set. Red box indicates the original measurement. (a) Full dispersion. (b) Low frequency waves.

drifting plasma, consistent with previous work [3, 61] that this higher frequency component is a series of ion acoustic waves. Recall that the dispersion for IAT in the long wavelength limit is given by Eqn. 2.5 [69] where we have used the convention that a positive velocity is propagation towards the anode. For our measured electron temperatures we infer from the dispersion the ion drift velocity $u_i = 2.9$ km/s, which is commensurate with typical ion drift velocities for these plasmas ($2 - 4$ km/s [3, 66, 74]). This observation is consistent with other measurements in similarly configured cathodes [3, 61, 76]. We further note that we have measured the dispersion along the discharge axis and found that v_{IAT} is constant throughout the plume, within uncertainty.

In a departure from previous work [3,80], however, we present in Fig. 3.7 the first dispersion measurements of the lower frequency, plume mode oscillations. Here we see that there is explicit structure in the dispersion that exhibits a fundamental frequency, $f_0 = 36$ kHz, along with its first harmonic, consistent with our observations in Fig. 3.6. Using a trend line that connects the center of each harmonic with the origin, we find that these two modes have a group velocity of $v_c = 7 \pm 2$ km/s, which is consistent, qualitatively, with our observations of light emission from the high-speed camera. Significantly, we note that although the mode and its harmonics propagate, the coherent oscillation does not appear to be a resident mode of the cathode-to-anode cavity ($v_c/\ell \neq 36$ kHz). In addition to the dispersion of the coherent oscillations, Figure 3.7 (b) also shows faint evidence of slowly propagating waves (the smaller slope line) with an estimated group velocity $v_s = 1.3 \pm 0.5$ km/s. This oscillation is characterized by frequencies between the coherent oscillations and the IAT. Interestingly, this type of oscillation was not anticipated from the power spectra plots in Fig. 3.6 and is only revealed by the dispersion analysis. We return to a discussion of this feature in the next section.

In sum, physically, the dispersion and Fourier measurements suggest the following features for the propagating high and low-frequency modes. There is IAT propagating from the cathode to anode, which is known to be involved in non-classical heating of electrons, and it coexists with the coherent plume mode instability. The wave propagates quickly and its speed is correlated with the light emission from the camera and has similar propagation characteristics to expectations from numerical simulations. However, we have yet to identify if a clear link exists between these two phenomena.

3.3.7 Single-point correlation between IAT and the Plume Mode Oscillation

As discussed in Sec. 2.5, the IAT is known to be a critical driver for the electron dynamics in the plume of these devices. Given that we now have established that it coexists with

the coherent plume mode oscillations, we next turn to the possibility of a correlational link between the two types of waves raised by numerical simulations. To this end, we choose to represent the average "energy" of the IAT with a characteristic amplitude and monitor this parameter on the time-scale of the low-frequency oscillation as an indicator for variations in heating. For the ionization-like oscillation, we examine the coherent component of the ion saturation current. We then compare variations in the average IAT amplitude and ion saturation current in time to determine if these parameters are correlated.

As such, we define an average amplitude of the IAT contribution to the power spectrum, $\mathcal{A}$, as

$$\mathcal{A} = \sum_{\omega} \left(\frac{\tilde{I}}{I_0} \right)_{\omega}^{2} , \tag{3.3}$$

where we summed over the range of the power spectrum associated with the IAT ($f > 0.02\,\omega_{pi}$), excluding those lower frequency modes. We then evaluate the time evolution of the IAT amplitude by employing a series of sequential short-time Fourier transforms of the probe signal. In our analysis, we collect ion saturation probe data for one period of the lower frequency component at $f_0 = 36$ kHz and apply a high-pass filter. We then create a window of width $\tau = 1/(10 f_0)$ and slide it along the time axis, sampling the waveform 100 times. Within each window, we calculate the average ion saturation current, assign a value to $\langle I \rangle_{\tau}(t)$, and apply a Fourier transform to calculate the IAT amplitude, $\mathcal{A}(t)$ with time-averaged value A_0. We have employed triggered-averaging to increase the signal-to-noise ratio of each parameter. The discharge current to the cathode provided the trigger reference as it also exhibits the same characteristic oscillations. We bandpass filtered the discharge current and used the peaks as the trigger point to perform 5000 averages and generate our plots.

Figure 3.8 shows the results of the short-time Fourier transform for the high-frequency, broadband IAT modes at three different times over the cycle of the plume mode oscillation.

This illustrates the change in amplitude of the IAT modes on this time-scale. At certain times, there is very little IAT, while at others the waves are several orders of magnitude larger. Qualitatively, we find that the high-frequency components appear to grow first, which is consistent with Eqn. 2.5. Physically this indicates that the growth rate of high frequency modes (smaller wavelengths) is greater than lower frequencies. Ultimately this result suggests that the electron collision frequency, which depends on the sum of these modes, per Eqn. 2.9, is changing over a cycle of the plume mode oscillation.

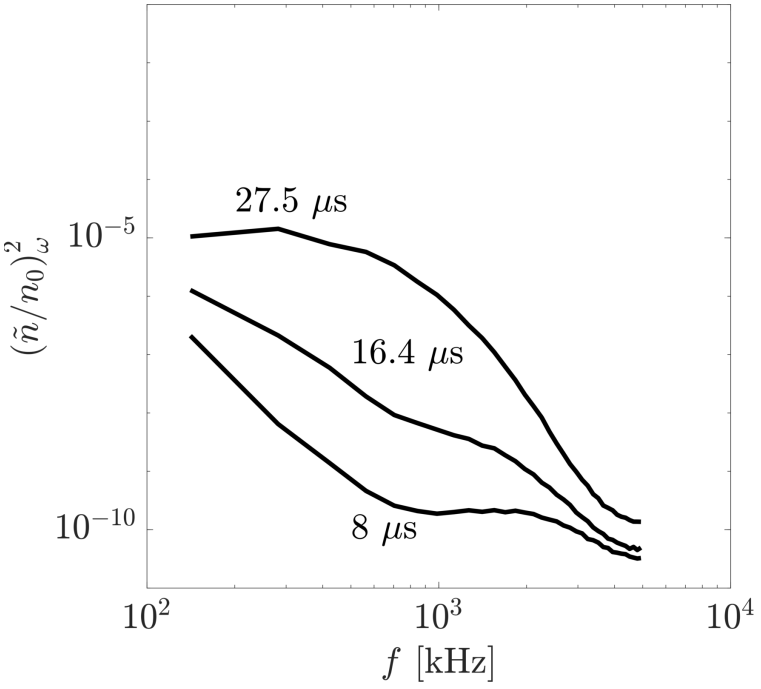

Figure 3.8: Time-resolved Fourier transform of the high-frequency IAT modes on the time-scale of the plume mode oscillation from the ion saturation current.

Representative results of this analysis are shown in Fig. 3.9 at z = 8 mm. This figure depicts both the time-dependence of the turbulent ($\tilde{\mathcal{A}}/\mathcal{A}_0$) and coherent ($\langle\tilde{I}\rangle_\tau/I_0$) components of the probe signal. Since our analysis only retains one period, we have concatenated three waveforms to better show the structure. A limitation of this triggered-averaging approach stems from the variance in phase and shape of the discharge current and ion saturation measurements between cycles. To reflect how this non-constant behavior can impact the averaged measurement, we also show the standard deviation as the gray bands in Fig. 3.9,

which is calculated from the variance in the 5000 points within each time bin. Allowing for this uncertainty, we note that our results demonstrate that the IAT and ion saturation current fluctuations are highly correlated in time. The peak-to-peak amplitude of the IAT relative fluctuation is an order of magnitude larger than the ion current and it unambiguously leads the current in phase. This relationship is valid throughout the plume where, on average, the IAT leads the density by $\theta = 75^\circ \pm 15^\circ$ as calculated by cross-correlation.

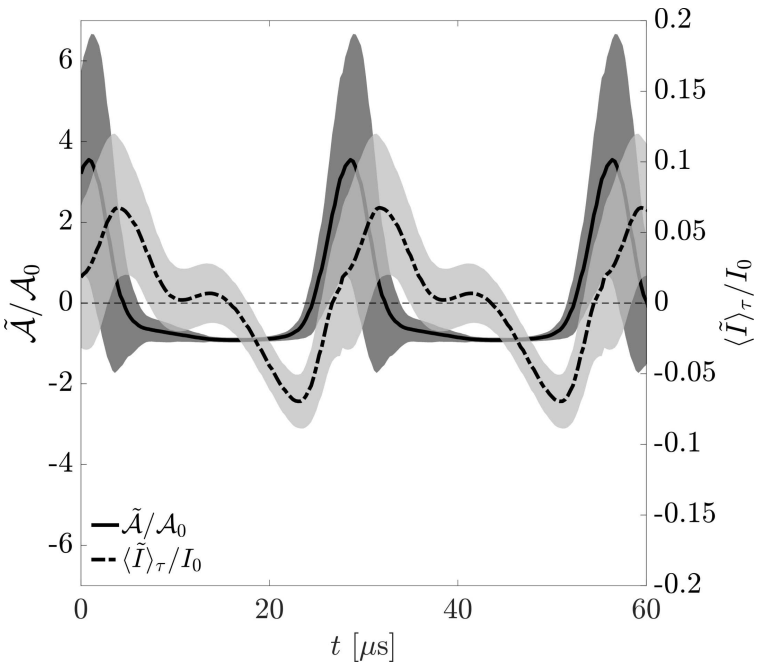

Figure 3.9: Fluctuations in IAT amplitude and ion saturation current determined from ion saturation probes.

Physically, this result shows for the first time, that the amplitude of the IAT modes is modulated in time at 36 kHz and is correlated with the characteristic coherent oscillation of the plume mode wave. With that said, these are single point measurements, and it remains to be seen if this correlation persists throughout the plume. To evaluate this, we turn in the next section to spatially resolved measurements of the these parameters and compare them with the light emission measured by the high-speed camera.

3.3.8 Spatial correlation between IAT and the Plume Mode Oscillation

Beyond this single point measurement, we employed the same triggering technique to reconstruct the spatio-temporal evolution of the relative fluctuations of the IAT and ion saturation current. We plot these results separately in Fig. 3.10 where we show (a) the fluctuations in IAT and (b) the ion saturation current over two cycles. The IAT average amplitude exhibits one dominant feature that propagates away from a maximum point (both towards the anode and cathode) at $z = 8$ mm downstream of the cathode exit with speed $v = 1.5 \pm 0.5$ km/s. The speed at which this change in IAT amplitude propagates is slower than the actual velocity of the underlying IAT spectrum, $v_{ph} = 4$ km/s (see Fig. 3.7). This discrepancy is a reflection of the fact that the parameter we plot is the periodic variation in the energy in the IAT modes, i.e. an amplitude modulation, which does not necessarily need to propagate at the same speed as the underlying IAT. Physically, it appears that this modulation is the critical parameter that is correlationally linked to the lower-frequency oscillations. Indeed, looking to Fig. 3.7 (b), we see that it is actually this modulation in energy of the IAT amplitude which is correlated with the response of the lower frequency, coherent mode. To this point, these coherent oscillations, $\langle \tilde{I} \rangle_\tau / I_0$, in ion saturation current in Fig. 3.10 (b) exhibit two features that appear to be linked in space in time with the IAT. The first is a perturbation that originates at $z = 8$ mm. And as the modulation in IAT amplitude propagates through the plasma, the density lags behind. This result further supports the correlational link between the IAT and the ionization mode throughout the entire length of the cathode plume. On the other hand, the ion saturation current exhibits a second feature not observed in the IAT plot: a faster moving branch which appears further downstream and moves at a higher speed (7 km/s). This component of the plasma oscillation is correlated with the more coherent harmonic structure (peaks in Fig. 3.6) and the high-velocity, coherent modes in the dispersion shown in Fig. 3.7. Indeed, it is this contribution that we visually associate with the coherent plume-mode oscillations from the high-speed camera.

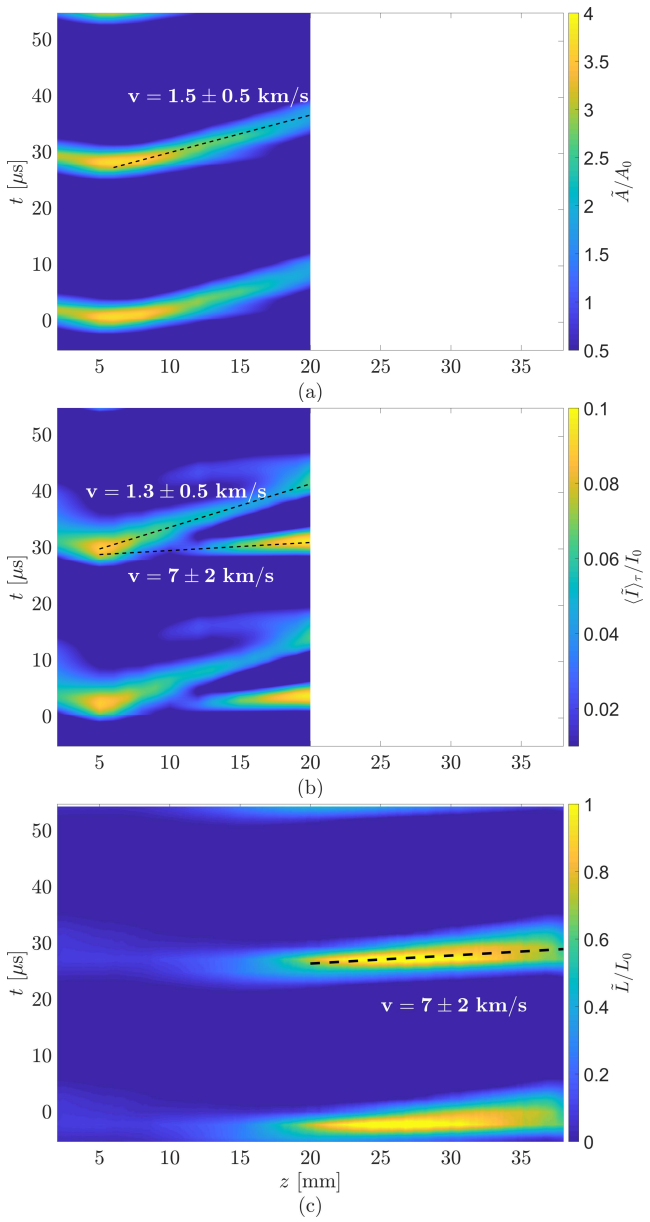

Figure 3.10: (a) Evolution of IAT fluctuations along the axis of the discharge. (b) Evolution of the coherent ion saturation current fluctuations along the axis of the discharge. (c) Evolution of the radially averaged light emission. Data is interpolated and saturated to better show trends. $z = 0$ [mm] is the keeper surface.

To illustrate this point, Fig. 3.5 shows that the evolution of this faster branch in $\langle \tilde{I} \rangle_\tau / I_0$, is markedly similar to the light emission captured by the high-speed camera. Figure 3.10 (c) shows similar trends in the relative fluctuations in light emission, $\tilde{L}/L_0$, where $\tilde{L}$ is the fluctuation in light emission and L_0 is the time-averaged light emission. To calculate these

parameters, we reconstructed a triggered-average cycle for each pixel in the image using 350 periods and averaged the result along the radial direction. To sync the camera with the probe measurements, we have set the maximum of the IAT modulation and light emission to occur at $t = 0$ μs. From the camera, we see that the perturbation generates light emission that propagates at 7 ± 2 km/s, in agreement with the velocity of the coherent structure in Fig. 3.7 (b) and the high-speed component in Fig. 3.10 (b). Notably, however, the slow branch found in the turbulence and density does not appear to generate measurable light emission. This may be due to experimental limitations in the sensitivity of the high-speed camera.

Together Figs. 3.10 (a), (b), and (c) support the correlation of the large-scale plume mode with oscillations in average IAT amplitude. Physically, these figures point to the plasma being perturbed by a modulation in the amplitude of the IAT modes at a fixed location, which then responds with a low-frequency, propagating structure that results in the observed light emission. As the region of high IAT amplitude propagates in the plasma, the plasma density responds in kind. This result points to the possibility that IAT driven heating of electrons may lead to a change in the plasma density through ionization.

3.3.9 Discussion

3.3.9.1 Connection Between IAT and Density

The results in Figs. 3.7 - 3.10 provide new, fundamental insight into the potential link between IAT and the plume mode oscillation. With measurements of the dispersion, we were able to show that indeed the ionization-like plume mode wave and IAT coexist in the cathode plasma, as predicted by numerical simulation. The time-resolved analysis of the probes, showed that the IAT fluctuates on the time-scale of the lower-frequency plume mode instability. This is perhaps not unexpected as the IAT depends on plasma parameters that are oscillating on that time-scale; however, we showed that the IAT amplitude leads the density in phase. This result suggests that there may be a causal link between the two,

possibly through ionization if the electron temperature varies as well. Despite this strong correlation, we still need to show that the electron temperature oscillates over a cycle of the plume mode to conclusively identify this as an ionization instability. This requires a more detailed experiment, which we describe later in Sec. 3.4.

3.3.9.2 Comparison to Simulation

Our experimental results showed that the plume mode is composed of multiple propagating structures. There is the oscillation in IAT wave amplitude that appears to cause the plasma density wave, which propagates at slow speed, and there is a second branch that travels at high-velocity in the density and light emission that is more commonly associated with the coherent properties of the wave and physically looks like a form of ionization front that propagates faster than the acoustic speed. The propagation characteristics of this high speed component are similar to that of numerical results, [5] which are reproduced in Fig. 3.11. Figures 3.10 and 3.11 are remarkably similar in their structure and propagation. Both results indicate a localized region where the plume mode wave begins, and find a comparable propagation velocity (around 10 km/s) that is several times greater than the ion acoustic speed. Furthermore, both the simulation and experiment show that there is a component of the wave that propagates back towards the cathode. The similarity between these independently generated results suggests that the simulations are capturing physically realistic results.

3.3.9.3 Summary

To summarize, through this experiment we have investigated the connection of the IAT to the plume mode instability. What we have found is that amplitude of the IAT is modulated on the time-scale of the low-frequency wave. The phase relationship between the IAT and the ion saturation current suggests a possible causal relationship between the turbulence and density fluctuations that could be consistent with an ionization process. From these results

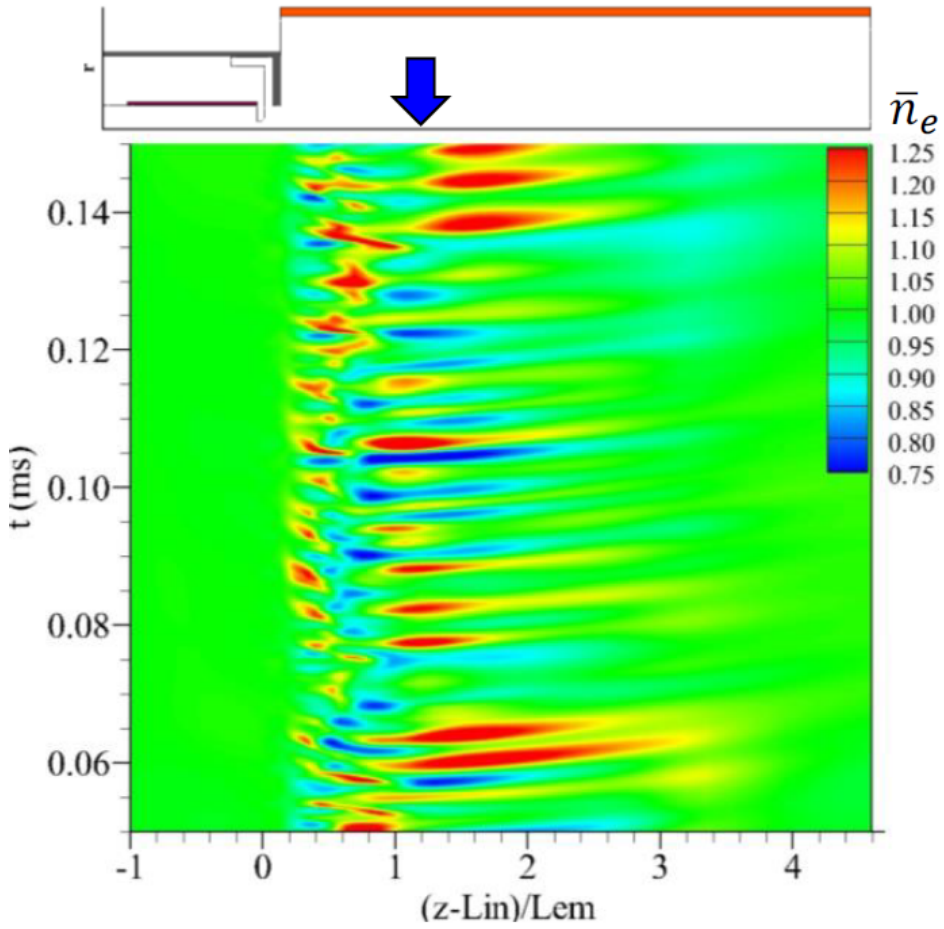

Figure 3.11: Simulation of the plume mode instability at 6 sccm. Reproduced with permission from Ref. [5].

a physical picture is beginning to emerge whereby changes in the turbulence lead to heating and variations in the ionization rate that causes the observed changes in plasma density (ion saturation current) In this picture, one key missing component is the connection of fluctuations in IAT to changes in electron temperature on the time-scale of the plume mode. This topic will be discussed in the following section.

3.4 Variation of Plasma Properties Over the Plume Mode Time-scale

For this final experiment, the goal is to look at the other plasma properties that vary on the time-scale of the ionization-like plume mode oscillations to inform our analytical treatment of that wave. With this aim in mind, we next use a collection of electrostatic plasma diagnostics to quantitatively examine the oscillations in plasma parameters, such as temperature, density and potential on the time-scale of the plume mode wave. Furthermore, we explore the possible connection to heating from IAT and how oscillations in the IAT wave energy may drive temperature changes in the plume. To this end, we first describe the experimental setup. Then we discuss the analysis technique used to extract the variations in plasma properties on the time-scale of the plume mode instability. Next is a presentation of the experimental results, which is followed by a discussion on how our results guide the development of our theory in Chapter 4. In particular, our goal is to show that the IAT wave energy, and consequently the anomalous collision frequency by Eqn 2.9, fluctuates in time and that this leads to variations in electron temperature in the cathode plume. Lastly we summarize the findings of this experiment.

3.4.1 Experimental Methods

We again operated a 20 A LaB_6 hollow cathode with a 3 mm tungsten orifice and a graphite keeper at a flow rate of 5 sccm of xenon gas. The plasma discharge was maintained at 20 A of discharge current to a cylindrical, water-cooled anode positioned 45 mm downstream of the keeper exit. Again, the lower the mass flow rate, the greater the amplitude of the low-frequency ionization-like plume mode wave. The cathode was used in a 0.5 m $\times$ 1 m vacuum chamber that achieved a base pressure of 0.1μTorr and an operating pressure of 20 μTorr-Xe through cryogenic pumping. To diagnose the plasma, we used three probes, an emissive probe, a floating probe, and an ion saturation current probe. Together these can be

used to extract quantities such as the plasma potential, electron temperature, and plasma density. Figure 3.12 shows the experimental setup, indicating the position of the probes, the cathode, and the anode. These three probes were measured at 10 MHz using an oscilloscope. This acquisition rate was selected to both capture many cycles of the low frequency wave of interest, while also resolving the high-frequency turbulence in the signals.

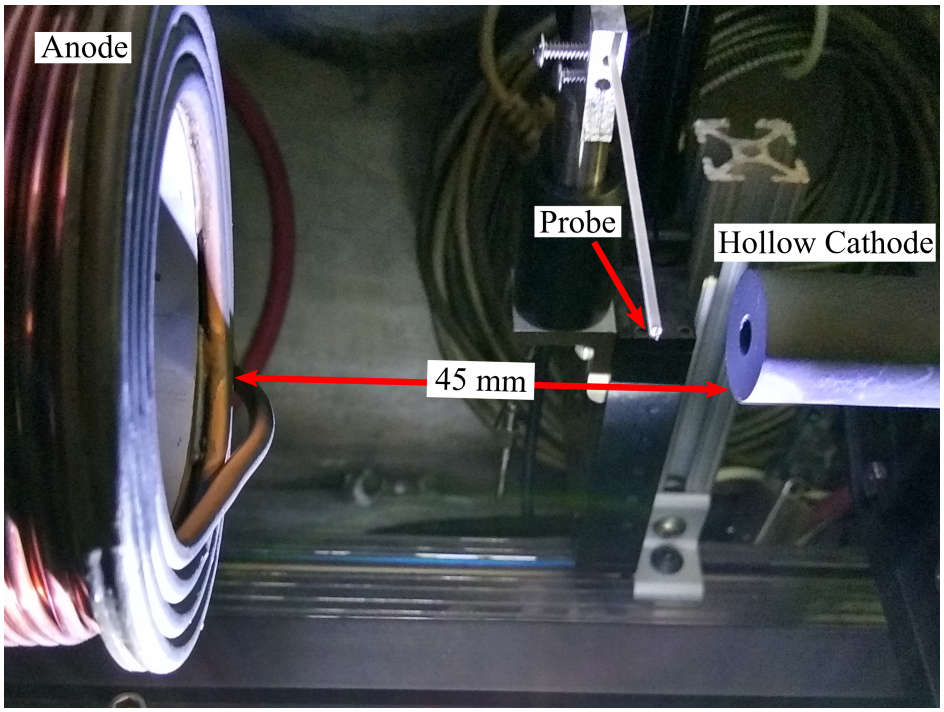

Figure 3.12: Experimental setup for high-speed probing, showing the emissive probe.

3.4.2 Analysis Techniques

We next present our technique to determine the density, temperature, electron drift velocity, and the IAT wave energy as a function of time. To calculate these plasma parameters, we follow the technique use in [81]. In brief we use the emissive, floating, and ion saturation probes to determine electric field, temperature, and density. These parameters are used to infer the electron drift velocity from the electron continuity equation using ionization as a source term and assuming a conical expansion of the plasma from the keeper orifice to the anode. Time resolution is achieved by using the discharge current as a reference and phase

averaging to determine how these parameters evolve as a function of phase angle, θ, with respect to the discharge current oscillation. The inherent assumption is that the processes that cause the oscillation are the same cycle to cycle. The equations necessary for this calculation are

$$E = -\nabla\Phi \ , \ T_e = \frac{2(\Phi - V_f)}{\ln\left(\frac{2}{\pi}\frac{m_i}{m_e}\right)} \ , \text{and } n = \frac{I_{sat}}{0.61 A_p c_s}, \tag{3.4}$$

where E is the electric field, Φ is the plasma potential, V_f is the floating voltage, I_{sat} is the ion saturation current and A_p is the probe surface area. These quantities can be used to evaluate the electron continuity equation to estimate the electron drift velocity

$$u_e(z,t) = \frac{\int_{z_0}^{z}\left(n(z,t)\nu_{ion}(z,t) - \frac{\partial n(z,t)}{\partial t}\right)A(z)dz}{n(z,t)A(z)} + \frac{n(0,t)}{n(z,t)}\frac{A(0)}{A(z)}u_e(0,t) \ , \tag{3.5}$$

where ν_{ion} is the ionization rate calculated from Ref. [6] and $A(z)$ is the cross-sectional area of the plasma, which we have assumed to expand conically from the orifice to the anode. The boundary condition for velocity is $u_e(0,t) = I_{dc}(t)/qn(0,t)A(0)$ and is applied to our closest measurement to the cathode. The total collision frequency of the plasma, ν_e, is then calculated using Ohm's law for the electrons:

$$\nu_e = -\frac{q}{m_e u_e}E - \frac{\nabla(nT_e)}{nm_e u_e} \ . \tag{3.6}$$

We estimate the wave energy by calculating the Fourier transform of the ion saturation current signal over a short time constant ($\tau = 1.75\ \mu$s) and summing of the IAT contributions of the spectrum (see Fig. 3.6). This technique has been previously used to analyze fluctuations in turbulence level in Refs. [81–83]. The anomalous collision frequency, ν_{an}, is then determined using Eqn. 2.10 on this time-scale. In the following sections, we will compare the calculation of the total collision frequency and the anomalous collision frequency.

3.4.3 Results

3.4.3.1 Time-average

Figure 3.13a shows the steady state plasma potential, electric field and temperature. In the plume, we find the characteristic plasma potential rise associated with the presence of IAT. Furthermore, the electron temperature rises from about 1 eV to around 5 eV towards the anode. The solid lines are cubic spline fits that are later used for calculating derivatives. We find in Fig. 3.13b that the Mach number is relatively constant as a function of position in the plume and is of order 1. The plasma density is monotonically decreasing with distance from the cathode. By curve fitting to an exponential, we find that $\nabla(n)/(n) \sim 300$ m^{-1}. Lastly, in Fig. 3.13d, we show the electron collision frequency, ν_e, the anomalous collision frequency ν_{an}^{IAT}, the sum of the classical collision frequencies, $\nu_{ei}+\nu_{en}$, the ionization rate, ν_{iz}, the electron transit frequency, u_e/L, where $1/L \sim \nabla(n)/(n)$ and the diffusion frequency, $\nu_D = \frac{T_e}{m_i \nu_{in} L^2}$ (ν_{in} is estimated following Ref. [3]). We find that the total collision frequency in the plume is driven by the presence of IAT, in agreement with previous observations. [3, 61, 68] The ionization frequency peaks near the cathode then drops steadily. The diffusion rate grows as a function position and the electron transit frequency is relatively constant. In the following chapter, we will use these values to simplify the governing equations for our first-principles theory. Next, we examine some of these parameters in time to determine the connection between the IAT and electron temperature fluctuations.

3.4.3.2 Time-resolved

Now, we examine the time dependent properties of the plume. Figure 3.14 shows the Fourier transform of the ion saturation current. Here the plume mode waves are visible at harmonics of its fundamental frequency, $f = 40$ kHz. Additionally, there exist some high-frequency, broadband waves that are consistent with our previous measurements of IAT in the cathode plume. We find that the wave amplitude is generally decreasing as a function of position.

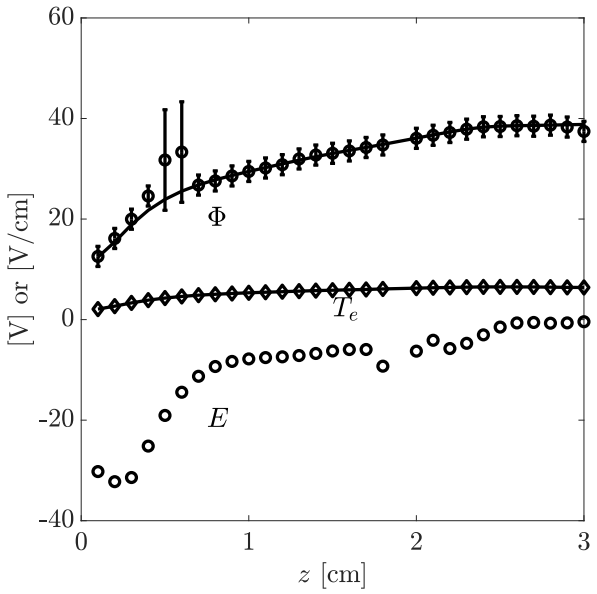

(a) Steady state plasma potential, electric field, and temperature profile determined from the emissive probe and floating probe.

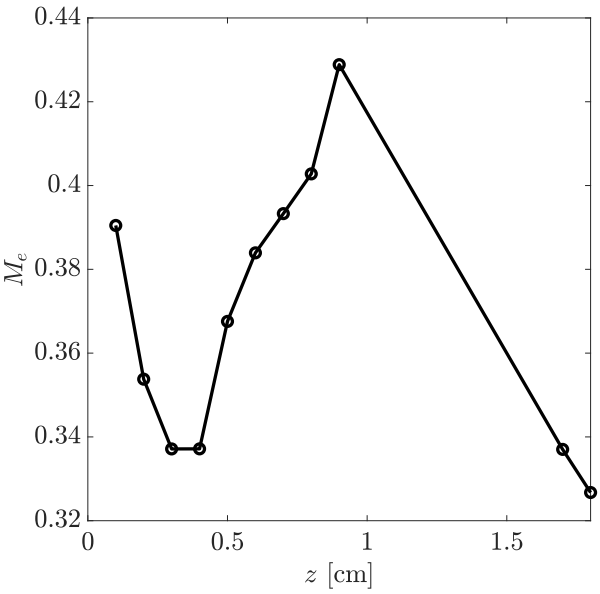

(b) Electron Mach number determined from the emissive probe, floating probe, and ion saturation probe using Eqn. 3.5.

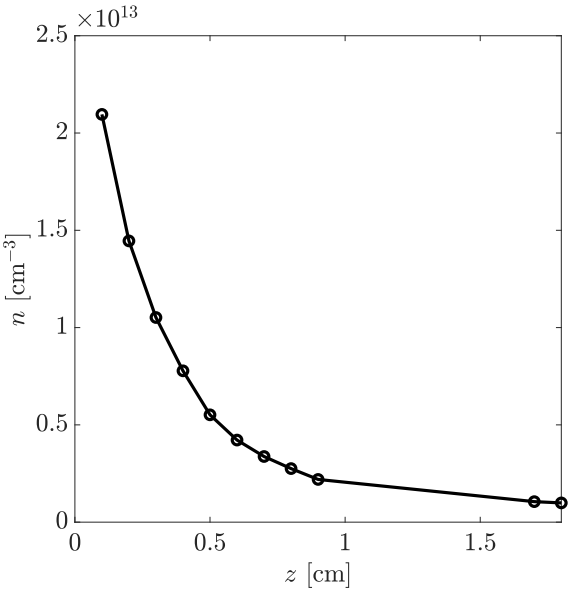

(c) Plasma density as a function of position determined from the ion saturation probe. Note we find that $\nabla(n)/n \sim 300$ m^{-1} by curve fitting with an exponential.

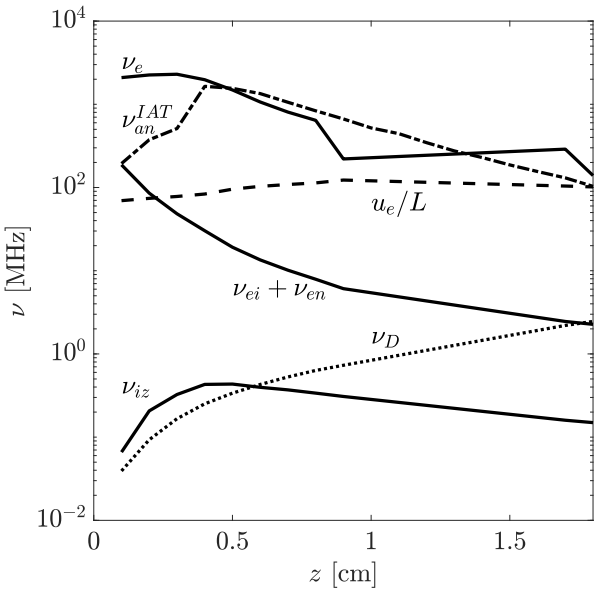

(d) Steady-state collision frequencies as a function of position. Note we have used a value of $\alpha_{IAT} = 2$ for the proportionality constant of the IAT, which is commensurate with the values in Ref. [4], we have used $L \sim \nabla(n)/n$.

Figure 3.13: Steady state plasma parameters in the plume. $z = 0$ [cm] is the keeper surface. ($I = 20$ A, $\dot{m} = 5$ sccm)

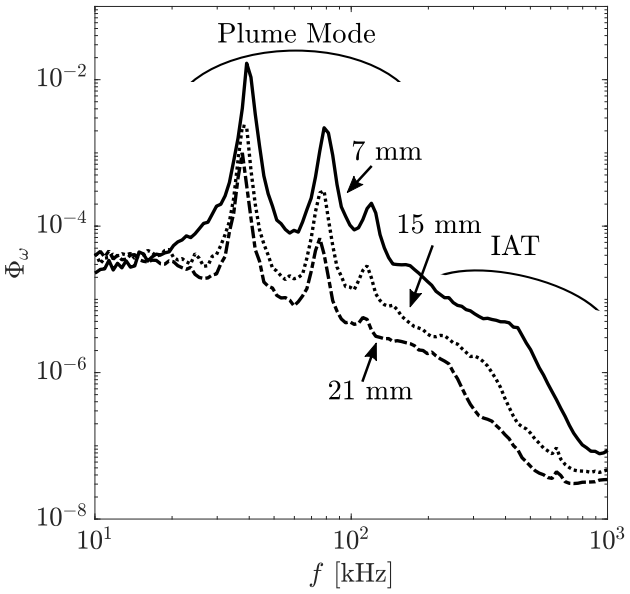

Figure 3.14: Fourier transform at 3 locations in the plume from the ion saturation probe.

Figure 3.15 is the peak-to-peak electron temperature fluctuations as a function of position. The electron temperature oscillation varies intensely by around 2 eV at a location near the cathode where the electric field is near its peak (see Fig. 3.13a). This is consistent with our observations from the camera, where a bright region periodically produces light. We conduct our time-resolved analysis at this peak location.

Next, we use our measurements of the time-dependent plasma parameters to calculate the time-dependent collision frequency in the plume by evaluating Ohm's law (Eqn. 3.6. This calculation is compared with estimates of the classical electron-neutral collision frequency [84] and Coulomb collision frequency [85] as well as the contribution from IAT determined through Eqn. 2.9. Comparing all of these frequencies, Fig. 3.16a shows that the IAT-driven collision frequency, ν_{an}^{IAT}, is the dominant contributor to changes in the total collision frequency, ν_e. To more closely examine the correlation between the total collision frequency and the anomalous collision frequency, we show in Fig. 3.16b a response plot where we plot ν_e against ν_{an}^{IAT}. If the two parameters are perfectly correlated, then all the points would line up on the dashed line. Since the points lie close to this line of perfect correlation, we conclude that the two are highly correlated, that the IAT is is the dominant contributor

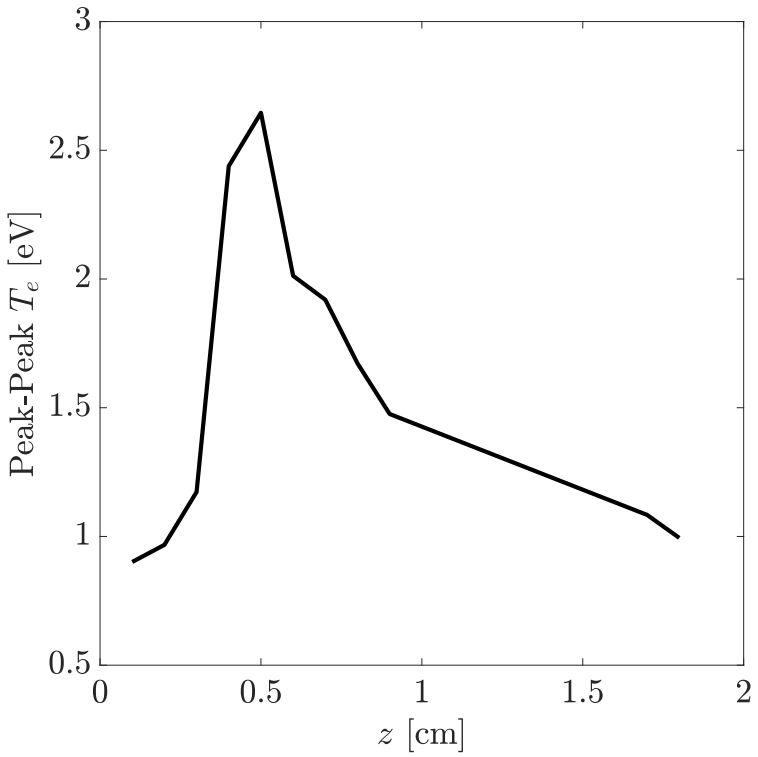

Figure 3.15: Peak to peak temperature fluctuations in the plasma localized near the cathode. Position $z = 0$ [cm] is the keeper surface.

to resistivity, and that variations in the IAT are dictating changes in the resistivity of the electrons.

The notion of IAT controlling the electron temperature is explored further in Fig. 3.17, where we plot the fluctuations in current, IAT wave energy, electron temperature and density relative to their mean values at $z = 5$ mm downstream of the cathode exit, the location of the peak electron temperature fluctuations. In this condition the discharge current oscillates at around 50% peak-to-peak of its average. The IAT wave energy is also fluctuating, as we have previously seen. In addition, we find that the temperature is lagging the IAT in phase and that the density lags the electron temperature by around 70°. A plausible physical interpretation of these results is that the IAT is heating the electrons, which subsequently leads to a rise in plasma density via ionization. The density and electron velocity are slightly out of phase, which allows for the discharge current oscillation. These trends point to a physical interpretation consistent with the numerical results discussed in Sec. 2.5. The large

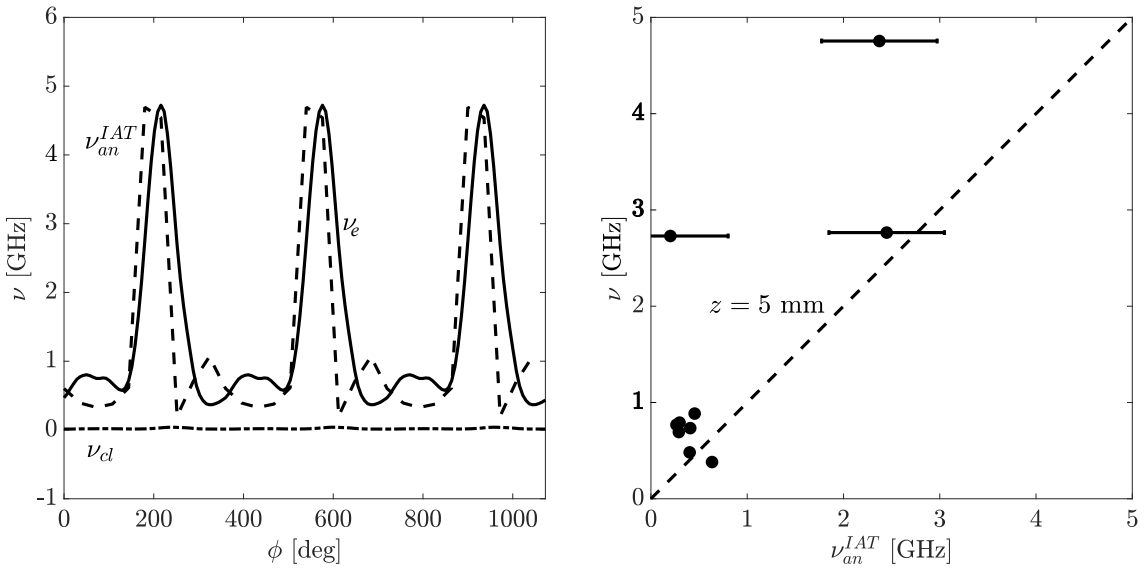

(a) Peak-to-peak temperature fluctuations in the plasma localized near the cathode at $z = 0.5$ cm as a function of phase angle with respect to the discharge current oscillation.

(b) Response curve of the collision frequency with anomalous collision frequency at $z = 0.5$ cm.

Figure 3.16: Comparison of total and anomalous collision frequencies. (5 sccm)

variation in resistivity (due to changes in IAT wave energy) agrees with the findings of *Sary et. al.* and could potentially be interpreted as the periodic saturation of the turbulence; however, the key finding that the temperature leads the density in phase indicates suggests that ionization is likely playing a role in the oscillation cycle, contrary to their conclusions in Ref. [57]. In summary, we propose that this could possibly be interpreted as a predator-prey wave that is ultimately driven unstable by temperature oscillations [38] that are the result of Ohmic heating from IAT.

3.4.4 Discussion

From this experiment, we have found new key insight into the time-varying properties of the plume mode wave. We showed in Fig. 3.15 that there indeed are electron temperature fluctuations in the plume and that they are localized near the cathode exit. Given the large temperature oscillations, relative to their mean value, this result suggests that the light emis-

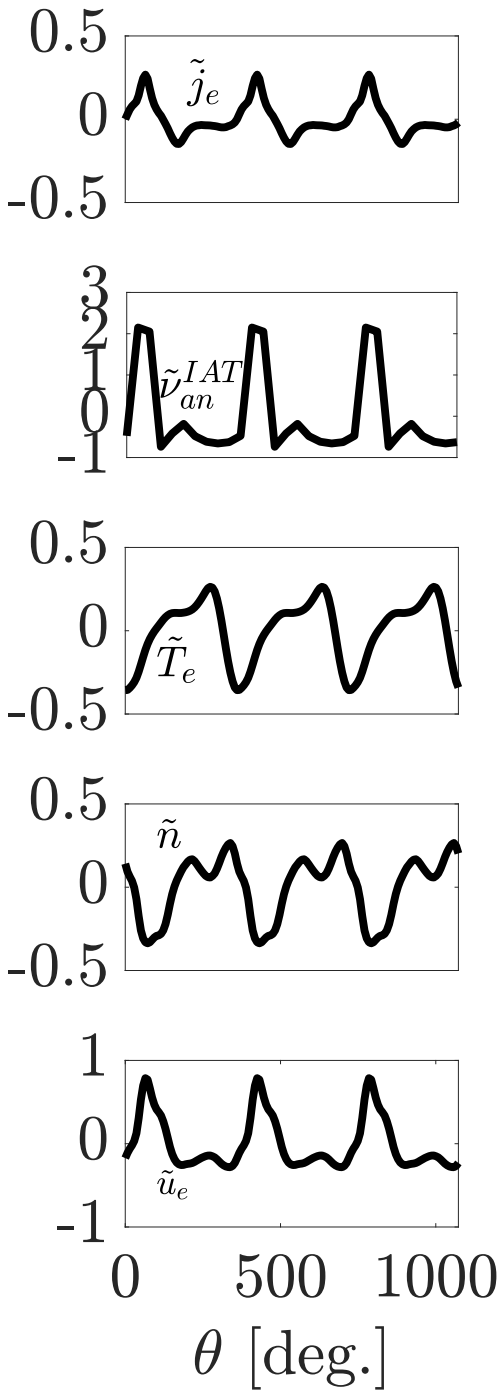

Figure 3.17: Oscillating plasma parameters normalized to their mean value as a function of phase angle with respect to the discharge current at $z = 5$ mm. (5 sccm)

sion we observe will be strongly tied to this parameter based on the exponential dependence on temperature in Eqn. 3.1. This explains the strong correlation between the light emission and the IAT and density. We have also showed in Fig. 3.16a that the changes in plasma resis-

tivity are driven by the IAT. This crucial finding, along with our time-resolved measurements in the plasma parameters in Fig. 3.17, is what links the IAT fluctuations to the temperature and ultimately density through ionization. In combination, these results primarily support the interpretation of numerical simulations by *Mikellides et. al.*, where Ohmic heating of the electrons is the critical process for the formation of the plume mode instability. Our novel interpretation is that changes in the turbulence modulate the temperature which is thought to drive a predator-prey mode unstable. In the following Chapter, we will use these results to build an intuitive physical description of the wave and to simplify the governing equations to ultimately derive a first principles theory for the plume mode instability.

3.5 Conclusions

In conclusion, we have conducted three experiments, using a high-speed camera and high-speed electrostatic probing techniques. The camera showed that the plume mode oscillation is a localized phenomenon, suggesting that it could be described in 0 dimensional manner. The second experiment examined the connection between acoustic turbulence and the plume mode wave. We found that the IAT amplitude was modulated on the same timescale. The phase between the IAT and ion saturation current measurements implied a possible causal relationship that is qualitatively consistent with an ionization wave. Finally, we investigated the time-dependent properties of the plasma and found that the IAT oscillations are highly correlated with the electron temperature and that the density lags the temperature, as would be expected from an ionization process. Together, these results point to the following experimentally informed insights.

1. The plume mode wave originates at one location in the plasma and propagates away from it. This potentially suggests that a 0 dimensional approach is appropriate if we are only interested in understanding what drives the wave unstable.

2. On the time-scale of the oscillations, the electron dynamics are non-classical and driven

primarily by the presence of IAT.

3. We have showed that following phase relationship between parameters: the IAT collision frequency leads the temperature, which leads the density, which is approximately out of phase with the electron velocity.

CHAPTER 4

Fluid Theory for Ionization Instability of the Cathode Plume

4.1 Introduction

In this Chapter, we develop a fluid theory based on the experimental evidence presented in Chapter 3. First we begin with a qualitative description of a proposed physical mechanism for the instability based on predator-prey oscillations. Then, we simplify the fluid equations (see Eqn. 2.12) by applying assumptions that are supported by our measurements while retaining the important physics. This is followed by a linear perturbation of the equations to arrive at the relationships between key experimental observables such as density, temperature, and velocity and discuss them for physical insight into our earlier results. Lastly, we solve the perturbed equations for a real frequency and growth rate that are then discussed in the context of our previous experimental results, the mechanism we have proposed, and observations from the literature.

4.2 Qualitative Description of Ionization Instability

Our proposed description for the plume mode oscillation combines previous analytical work on predator-prey modes in plasma propulsion devices and key insight from numerical simulations, notably that the effects of turbulence are necessary for onset, with our experimental

measurements in Chapter 3. An analysis of the equations that govern predator-prey oscillations in plasmas showed that this behavior is unconditionally damped by an influx of neutral atoms; [39] however, a linear analysis has suggested that fluctuations in electron temperature may be able to drive this process unstable. [39] The results of numerical models suggested that the presence of enhanced Ohmic heating of electrons from IAT is required for the presence of plume mode and our experimental measurements in Chapter 3 showed that the IAT amplitude varies and drives temperature fluctuations on the time-scale plume mode instability. The temperature is found to lead the density in phase by 70°, suggesting a causal relationship between the fluctuations in these parameters. A possible mechanism for this phase delay is through ionization. This evidence supports the conclusions of previous experimental and numerical investigations that this wave might be described by predator-prey behavior between the electrons and neutral gas. [2, 5]

In the cathode plume, there is predator-prey behavior between the plasma and neutral particles, which can be thought of as a "feast" and "famine" cycle for the electrons. The neutral density should lead the plasma density by 90° of phase because the ionization rate depends on the neutral density. When the neutral density is high, the electrons can "feast" on them, i.e. the ionization rate is high. When the neutral density is low, then the electrons are in "famine." In other words, the ionization rate is low. This cycle is a stable point of the Lotka-Volterra system of equations that describes this type of oscillation. [86] Meanwhile, the ionization rate also depends on temperature and can act as a destabilizing mechanism for this feast-famine behavior for the electrons, depending on the phase relationship between the temperature and the densities. If the temperature has an in phase component with the neutral density, then the feasting part of the cycle will be enhanced. The ionization rate will be higher during the growth part of the cycle, causing the plasma density to overshoot its peak value from the previous cycle. At a later time when the neutral density is low, the famine will also be greater. This means that the plasma density will undershoot its minimum density from the previous cycle. With every iteration of the cycle, the changes

in temperature will continue to enhance the electron density and lead to growth. This process is illustrated in Fig. 4.1a. Indeed, we have shown experimentally in Chapter 3 that the temperature leads the plasma density by 70°, which is consistent with this growth mechanism. However, these measurements also indicated that plasma diffusion likely also plays a role, a process which is also controlled by the electron temperature through the ambipolar electric field. Therein lies a possible onset criterion. If the plasma production through ionization exceeds the losses to diffusion and the neutral influx condition, then we could find instability. Figure 4.1b illustrates this mechanism by which the wave can driven unstable by temperature fluctuations.

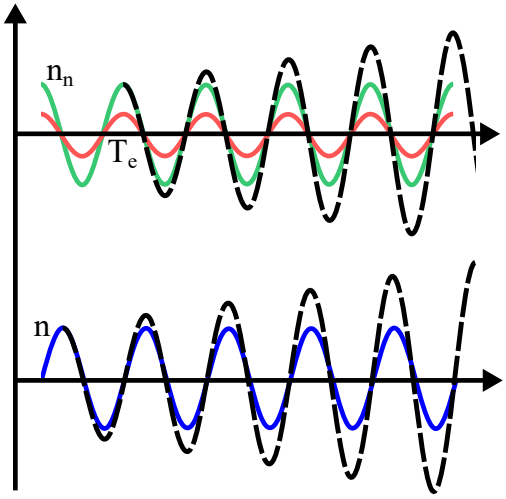

(a) Illustration of the predator-prey oscillation in the plasma density, neutral density, and electron temperature overtime.

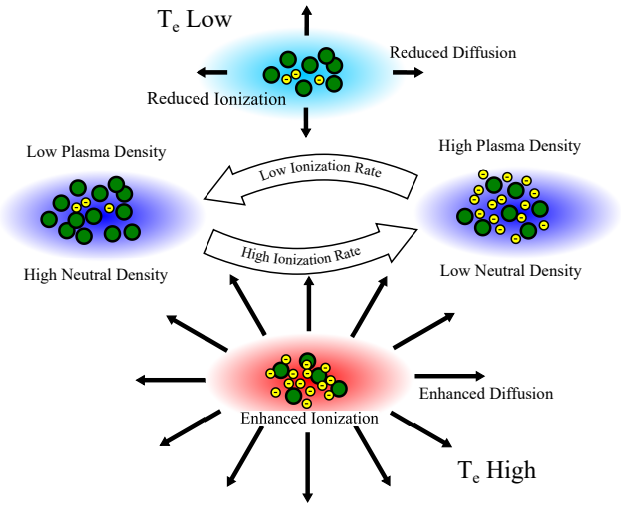

(b) Physical picture for the mechanism behind an ionization instability. Predator-prey action between the plasma and neutral gas is enhanced by temperature fluctuations if particle production through ionization is greater than diffusion losses.

Figure 4.1: Illustrations of the predator-prey process.

4.3 Simplification of the Fluid Equations

In this section, we work to simplify the general fluid equations and find a set of expressions that captures the underlying physics of the process we described qualitatively in Sec. 4.2.

4.3.1 Plasma Equations

Under the assumption that quasineutrality holds on the relatively long time-scales of this instability, the ion continuity equation is given by

$$\frac{\partial n}{\partial t} + \nabla \cdot (n u_i) = n \nu_{iz}(n_n, T_e) \ , \tag{4.1}$$

where ν_{iz} is the ionization rate of the plasma, which depends on the neutral density and electron temperature. This expression reflects the fact that the variations in plasma density are the result of changes in ion flux and ionization. We have assumed that ion losses through re-combination type processes are not a critical part of the mechanism that determines oscillation oscillation characteristics. Physically, this is justified by the low classical collision frequency between electrons and ions in the plume, along with the fact that there are no nearby surfaces in this region by which recombination can be mediated. Similarly, we write the electron continuity equation as

$$\frac{\partial n}{\partial t} + \nabla \cdot (n u_e) = n \nu_{iz} \ . \tag{4.2}$$

Combining the electron and ion continuity equations, we arrive at

$$\nabla \cdot (n u_e) = \nabla \cdot (n u_i) \ . \tag{4.3}$$

From our physical description, we suspect that the electrons are driving the wave. Therefore it is convenient to express the ion velocity in terms of other electron parameters and reduce the order of the problem. With this goal in mind, we examine the momentum equations to find such an expression for the ion velocity. We write the ion momentum equation as

$$m_i \frac{\partial n u_i}{\partial t} + m_i (u_i \nabla \cdot (n u_i) + n u_i \nabla \cdot (u_i)) = nqE - n m_i (u_i - u_n) \nu_{in} - n m_e (u_i - u_e) \nu_{ei} - \nabla (n T_i) \ . \tag{4.4}$$

Here m_i is the ion mass, q is the unit charge, E is the electric field, ν_{in} is the ion-neutral collision frequency, T_i is the ion temperature, and ν_{ei} is the electron-ion collision frequency. Equation 4.4 describes the change in ion momentum that is dictated by the acceleration due to electric fields and collisional effects. Collisions between ions and neutrals lead to a loss of ion momentum because the ions move quickly compared to the neutrals. Conversely, collisions between electrons and ions lead to an increase in ion momentum, although because of the disparity in the electron and ion mass, little momentum is generally transferred in this manner. The electron momentum is described by an Ohm's law, having neglected the electron inertia given their small mass:

$$0 = -nqE - \nabla(nT_e) - nm_e(u_e - u_i)\nu_{ei} - nm_e(u_e - u_n)\nu_{en} \ . \tag{4.5}$$

We simplify the momentum equations using a velocity hierarchy that is known to apply to the cathode plasma. [63] We assume that $u_n \ll u_i \ll u_e$, allowing us to simplify momentum equations to

$$m_i\frac{\partial nu_i}{\partial t} + m_i(u_i\nabla\cdot(nu_i) + nu_i\nabla\cdot(u_i)) = nqE - nm_iu_i\nu_{in} + nm_eu_e\nu_{ei} - \nabla(nT_i) \tag{4.6}$$

$$0 = -nqE - \nabla(nT_e) - nm_eu_e\nu_{ei} - nm_eu_e\nu_{en} \ . \tag{4.7}$$

Combining these two expressions, we can eliminate the electric field to find that

$$m_i\frac{\partial nu_i}{\partial t} + +m_i(u_i\nabla\cdot(nu_i) + nu_i\nabla\cdot(u_i)) = -\nabla(n(T_e + T_i)) + m_eu_e\nu_{en} - m_iu_i\nu_{in} \ . \tag{4.8}$$

With the ratio of the masses being $\mathcal{O}(10^{-6})$, we can neglect the effect of electron neutral collisions on the total ion momentum. Additionally, we know that the ion pressure is typically low compared to that of the electrons in these plasmas. [6] By combining with the ion

continuity equation, we find that

$$nm_i\frac{\partial u_i}{\partial t} + m_i u_i(\nu_{in} + \nu_{iz} + \nabla \cdot u_i) = -\nabla(nT_e) \tag{4.9}$$

Experimentally, we know that $\nu_{in} \sim 10^6$ Hz (calculated using the expression for the cross-section in Ref. [3] and measurements of the ion drift velocity [67]) and $\nu_{in} > \omega \sim \nu_{iz} \sim 10^5$ Hz. [2] Additionally, the drift velocity only changes slowly in plume, (see Ref [67]) giving $\nabla \cdot u_i \sim 0$. Therefore changes in ion inertia are small, so we neglect the time derivative in the ion velocity. Note that these assumptions are perhaps strong, given recent simulations that indicate that the ion inertia may be important. [68] This leaves us with

$$nm_i u_i \nu_{in} = -\nabla(nT_e) \tag{4.10}$$

$$\nabla \cdot (nu_i) = -\frac{\nabla^2(nT_e)}{m_i \nu_{in}} \tag{4.11}$$

Physically, this implies that the change in ion flux is the result of ambipolar diffusion. Note that by by neglecting the ion inertia we are contradicting some of the numerical results [68] that concluded the ion inertia is important. Substituting this back into the continuity equation, we find that

$$\boxed{\frac{\partial n}{\partial t} - \frac{\nabla^2(nT_e)}{m_i \nu_{in}} = n\nu_{iz}} \tag{4.12}$$

For the electrons, then we have from Eqn. 4.3

$$\boxed{\nabla \cdot (nu_e) = -\frac{\nabla^2(nT_e)}{m_i \nu_{in}}}\,. \tag{4.13}$$

Physically, these equations show that the plasma particle conservation is a balance between diffusion processes and ionization. This contrasts the predator-prey model in Hall thrusters, which is normally formulated using the convection of ions and neutrals. [37,39] Furthermore,

changes in the electron current are due to diffusion, which is linked to the ionization rate. For the cathode plume we have shown that diffusion of the particles is controlled by ambipolar fields established by electron pressure gradients. These processes are illustrated in Fig. 4.2.

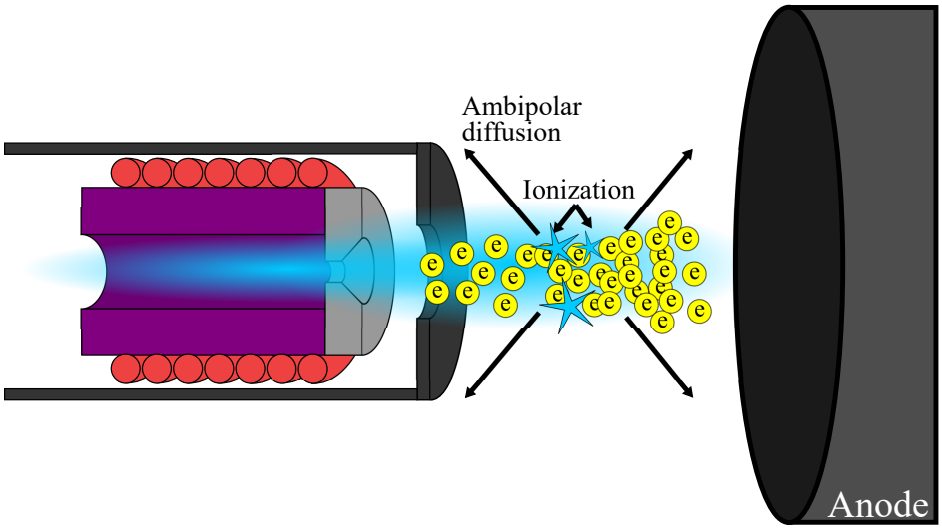

Figure 4.2: Plasma production through ionization is balanced by diffusion losses.

4.3.2 Neutral Equations

In addition to conserving the plasma particles, we must also conserve the neutral atoms. The continuity equation for this species is given by

$$\frac{\partial n_n}{\partial t} + \nabla \cdot (n_n u_n) = - n\nu_{iz} \ , \tag{4.14}$$

where n_n is the neutral density and u_n is the neutral drift velocity. Again, we have neglected any recombination source terms because in the plume region there are no walls to mediate this process and collisions between ions and electrons are relatively infrequent. Physically, this expression is balancing the influx of neutral particles with losses due to ionization, which is illustrated in Fig. 4.3. Here we have ignored the radial diffusion of the atoms, which is justified since the gas is cold and relatively collisionless. Furthermore numerical simulations often treat neutral particles ballistically, meaning they are not subject to any forces and do

not diffuse, and are still able to capture the ionization instability. [5]

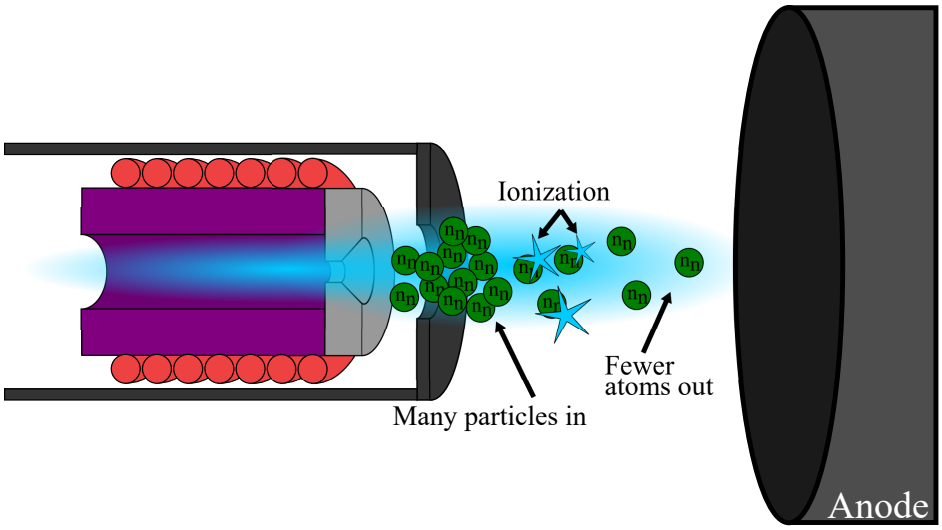

Figure 4.3: Neutral influx is balanced by ionization losses.

4.3.3 Electron Energy

The electron energy equation is

$$\frac{3}{2}\frac{\partial nT_e}{\partial t} + \frac{5}{2}\nabla\cdot(nu_eT_e) - u_e\cdot\nabla(nT_e) = nm_eu_e\left((u_e-u_i)\nu_{ie} + (u_e-u_n)\nu_{en}\right) - n\epsilon_{iz}\nu_{iz}\ , \tag{4.15}$$

where ϵ_{iz} is the energy lost due to inelastic ionization collisions. We have ignored heat conduction because our experimental measurements indicate that the temperature rises approximately linearly in the plume (see Fig. 3.4). We have also ignored collisional heat transfer because it scales with $m_e/m_i \ll 1$. Again applying our velocity hierarchy to simplify this expression, we have

$$\frac{3}{2}\frac{\partial nT_e}{\partial t} + \frac{5}{2}\nabla\cdot(nu_eT_e) - u_e\cdot\nabla(nT_e) = nm_eu_e^2\nu_e - n\epsilon_{iz}\nu_{iz}\ , \tag{4.16}$$

By substituting Eqn. 4.2 and combining, we can show that

$$\frac{3}{2}\frac{\partial T_e}{\partial t} + \frac{3}{2}T_e\nu_{iz} + \frac{3}{2}u_e \cdot \nabla(T_e) + T_e\nabla \cdot (u_e) = m_e u_e^2 \nu_e - \epsilon_{iz}\nu_{iz} \ , \tag{4.17}$$

Making the simplifying assumption that $T_e < \epsilon_{iz}$, as has been shown experimentally (see Fig. 3.4), the equation becomes

$$\boxed{\frac{3}{2}\frac{\partial T_e}{\partial t} + \frac{3}{2}u_e \cdot \nabla(T_e) + T_e\nabla \cdot (u_e) = m_e u_e^2 \nu_e - \epsilon_{iz}\nu_{iz}} \ . \tag{4.18}$$

Physically, this equation is balancing the change in heat flux with Ohmic heating and inelastic ionization collisions. By enhancing the electron collision frequency, ν_e, with an anomalous term from the IAT, we can see that this will lead to greater steady state temperatures and can lead to temperature variations in time. These processes are illustrated in Fig. 4.4

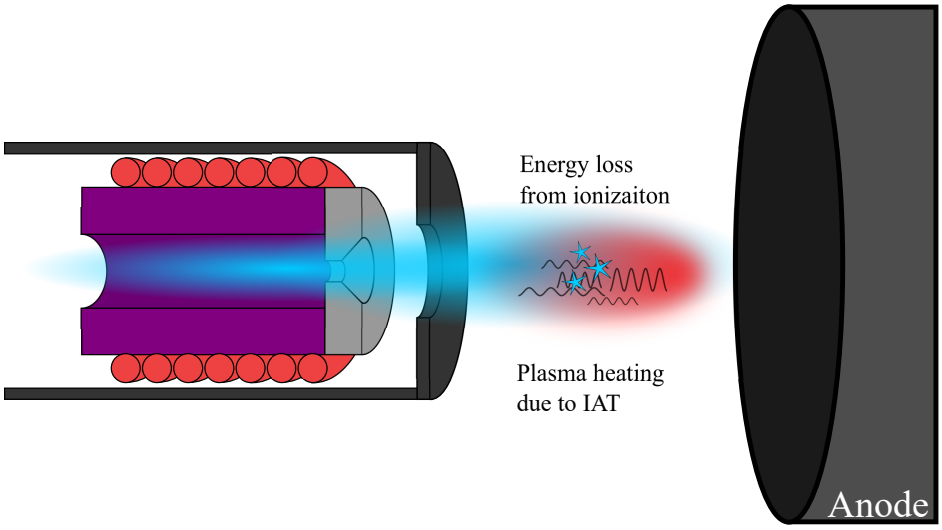

Figure 4.4: The thermal flux is balanced by wave-driven heating and ionization losses.

4.3.4 0 Dimensional Assumption

Experimentally, we have found that the plume mode instability is a localized phenomenon. We use this fact as grounds to simplify the problem further with a 0 dimensional approxima-

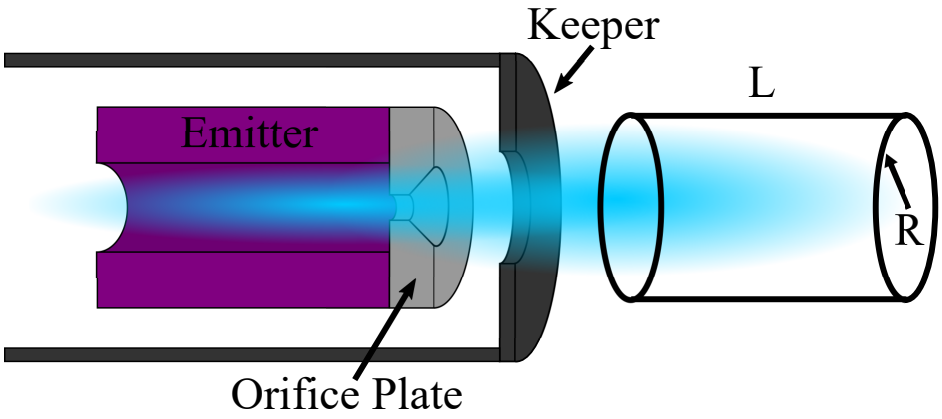

Figure 4.5: Volume of integration for the 0 dimensional plume model.

tion. This is done by integrating the equations over a volume $V = \pi R^2 L$, where A represents the cross sectional area and L is the length, around the "active region" of the plume. This integration volume is illustrated in Fig. 4.5. We define the inlet conditions via the subscript x_{in} and outlet conditions as x. We write our conservation equations for the outlet conditions, which is equivalent to a right-handed Riemann sum approximation. Experimental results from Ref. [2] suggest that the oscillation exists exclusively in the plume, not in the internal cathode plasma. We therefore assume that the inlet conditions do not vary in time while the outlet conditions do.

First examining the ion continuity equation, we find by integrating

$$\iiint_V \frac{\partial n}{\partial t} dV - \iiint_V \frac{\nabla \cdot \nabla(nT_e)}{m_i \nu_{in}} dV = \iiint_V n\nu_{iz} dV \tag{4.19}$$

We approximate the integral as a right hand Riemann sum such that

$$\pi R^2 L \frac{\partial n}{\partial t} - \iiint_V \frac{\nabla \cdot \nabla(nT_e)}{m_i \nu_{in}} dV = \pi R^2 L n \nu_{iz}. \tag{4.20}$$

Applying the divergence theorem, the expression expands to

$$\pi R^2 L \frac{\partial n}{\partial t} - \oiint_S \frac{\nabla(nT_e)}{m_i \nu_{in}} \cdot \hat{n} dS = \pi R^2 L n \nu_{iz} \ , \tag{4.21}$$

Where $\hat{n}$ is the normal vector for our cylindrical surfaces, S. Evaluating this expression at all three surfaces, we find that

$$\pi R^2 L\frac{\partial n}{\partial t} - \pi R^2\frac{\nabla_z(nT_e - T_{e,in}n_{in})}{m_i\nu_{in}} - 2\pi RL\frac{\nabla_r(nT_e)|_{r=R}}{m_i\nu_{in}} = \pi R^2 Ln\nu_{iz}\ . \tag{4.22}$$

We approximate the gradients as $\nabla_z = -1/L$ and $\nabla_r = -1/R$, which reflects the fact that the pressure is dropping axially and radially from the cathode orifice.

$$\pi R^2 L\frac{\partial n}{\partial t} + \pi R^2\frac{(nT_e - T_{e,in}n_{in})}{m_i\nu_{in}L} + 2\pi RL\frac{nT_e}{m_i\nu_{in}R} = \pi R^2 Ln\nu_{iz} \tag{4.23}$$

$$\frac{\partial n}{\partial t} + \frac{(nT_e - T_{e,in}n_{in})}{m_i\nu_{in}L^2} + 2\frac{nT_e}{m_i\nu_{in}R^2} = n\nu_{iz} \tag{4.24}$$

This expression for the continuity of ions tells us that radial losses by diffusion are balanced by the difference in the diffusive ion flux and ionization. Furthermore, through this process we have tied our lengthscales, in other words our integration volume, to the gradient lengthscales of the electron pressure.

Next, we examine the electron continuity equation. Applying the volume integral, we find that

$$\iiint_V \nabla\cdot(nu_e)dV = -\iiint_V \frac{\nabla\cdot\nabla(nT_e)}{m_i\nu_{in}}dV \tag{4.25}$$

$$\oiint_S nu_e\cdot\hat{n}dS = -\oiint_S \frac{\nabla(nT_e)}{m_i\nu_{in}}\cdot\hat{n}dS \tag{4.26}$$

We assume that the electrons near cathode centerline are primarily moving in the axial direction and have little bulk radial velocity, meaning $u_{e,r} \sim 0$. This is corroborated by measurements of the velocity distribution function through Thomson scattering. [87] This allows us to simply evaluate the equation as:

$$\pi R^2(nu_e - n_{in}u_{e,in}) = -\oiint_S \frac{\nabla(nT_e)}{m_i\nu_{in}}\cdot\hat{n}dS \tag{4.27}$$

The right hand side, we have previously solved. Applying this relation, we arrive at

$$\pi R^2(nu_e - n_{in}u_{e,in}) = \pi R^2 \frac{(nT_e - T_{e,in}n_{in})}{m_i \nu_{in} L} + 2\pi RL \frac{nT_e}{m_i \nu_{in} R} \tag{4.28}$$

$$\frac{(nu_e - n_{in}u_{e,in})}{L} = \frac{(nT_e - T_{e,in}n_{in})}{m_i \nu_{in} L^2} + 2\frac{nT_e}{m_i \nu_{in} R^2} \ . \tag{4.29}$$

This expression shows that the change in the axial electron current density in the control volume is due to changes in the axial and radial diffusion of electrons. Alternatively, by substituting this back into Eqn. 4.2 this tells us that the change in electron density is due to the balance of ionization and diffusion into the volume against the axial and radial diffusion losses at the outlet. Additionally, the dependence of the current density on temperature can result in a slight phase lag between the plasma density and electron velocity. This agrees with the experimental finding in Fig. 3.17, where we showed a small phase delay between the velocity and density, which produces the time-varying currents we associate with the plume mode oscillation.

Now we examine the neutral continuity equation. Again, we integrate over this control volume and find

$$\iiint_V \frac{\partial n_n}{\partial t} dV - \iiint_V \nabla \cdot (n_n u_n) dV = - \iiint_V n\nu_{iz} dV \ . \tag{4.30}$$

As is done in some fluid codes, we neglect forces on the neutrals. [62] The atoms that escape this part of the plasma are relatively collimated and experience relatively few collisions in the plume. As such, we neglect the bulk radial motion of the neutrals and prescribe a fixed neutral velocity such that

$$\frac{\partial n_n}{\partial t} = \frac{n_{in} - n_n}{L} u_n - n\nu_{iz} \tag{4.31}$$

This is the same expression as used for a predator-prey description of the Hall thruster channel. [39]

Lastly, we analyze the electron energy equation by applying the same right-hand Riemann sum technique and integration by parts to approximate the integral over our control volume. This gives

$$\iiint_V \frac{3}{2}\frac{\partial T_e}{\partial t}dV + \iiint_V \frac{3}{2}u_e \cdot \nabla(T_e) + T_e\nabla \cdot (u_e)dV = \iiint_V m_e u_e^2 \nu_e - \epsilon_{iz}\nu_{iz}dV \tag{4.32}$$

$$\pi R^2 L\frac{3}{2}\frac{\partial T_e}{\partial t} + \oiint_S T_e u_e \cdot \hat{n}dS + \frac{1}{2}\iiint_V u_e \cdot \nabla(T_e)dV = \pi R^2 L\left(m_e u_e^2 \nu_e - \epsilon_{iz}\nu_{iz}\right) \tag{4.33}$$

$$\pi R^2 L\frac{3}{2}\frac{\partial T_e}{\partial t} + \left(T_e u_e - T_{e,in}u_{e,in}\right)\pi R^2 + \frac{1}{2}\iiint_V u_e \cdot \nabla(T_e)dV = \pi R^2 L\left(m_e u_e^2 \nu_e - \epsilon_{iz}\nu_{iz}\right) \tag{4.34}$$

$$\frac{3}{2}\frac{\partial T_e}{\partial t} + \frac{T_e u_e - T_{e,in}u_{e,in}}{L} + \frac{1}{2}u_e\frac{T_e - T_{e,in}}{L} = m_e u_e^2 \nu_e - \epsilon_{iz}\nu_{iz}\ . \tag{4.35}$$

Here, we have assumed that the bulk radial velocity of the electrons coming out of the cathode is negligible. This simplification is justified by experimental measurements of the radial electron velocity distribution function in the radial direction through Thomson scattering. [87] From a physics standpoint, this expression represents how the convection of thermal energy is balanced by heating of the electrons and losses to inelastic ionization collisions.

4.3.5 Summary of Equations and Assumptions

Here we present the complete set of equations that we will perturb in order to describe the ionization wave associated with the cathode plume mode. In this model, the plasma and neutral particle interactions are related through the ion and neutral continuity equations. Changes in density and temperature are connected through the electron continuity equation and the energy equation. All together, the primary effects that we are considering here are Ohmic heating of electrons, ionization, and diffusion, which will ultimately form the basis for the ionization instability.

$$
\begin{aligned}
\frac{\partial n}{\partial t} + \frac{(nT_e - T_{e,in}n_{in})}{m_i\nu_{in}L^2} + 2\frac{nT_e}{m_i\nu_{in}R^2} &= n\nu_{iz} \\
\frac{(nu_e - n_{in}u_{e,in})}{L} &= \frac{(nT_e - T_{e,in}n_{in})}{m_i\nu_{in}L^2} + 2\frac{nT_e}{m_i\nu_{in}R^2} \\
\frac{\partial n_n}{\partial t} &= \frac{n_{in} - n_n}{L}u_n - n\nu_{iz} \\
\frac{3}{2}\frac{\partial T_e}{\partial t} + \frac{T_e u_e - T_{e,in}u_{e,in}}{L} + \frac{1}{2}u_e\frac{T_e - T_{e,in}}{L} &= m_e u_e^2\nu_e - \epsilon_{iz}\nu_{iz}
\end{aligned}
\tag{4.36}
$$

To arrive at this set of equations, we have made the assumption that the problem can be represented with a 0 dimensional model with influx and outflux conditions and that the influx is constant in time. This is justified by the localized nature of the plume mode (see Fig. 3.2) and that the plasma in the emitter region is not fluctuating. [2] The neutral particle velocity is considered to change slowly across our 0 dimensional volume, an assumption that follows those used in numerical models that are also able to recover the instability. [5] Furthermore, we have associated our control volume with the density gradient lengthscales. Lastly, we have applied the hierarchy in Tab. 4.1 to reduce the initially complicated set of equations.

Table 4.1: Assumptions used in the development of governing equations for an ionization instability that describes the plume mode.

Parameters	Hierarchy
Velocity	$u_n \ll u_i \ll u_e$
Frequency	$\nabla \cdot u_i < \omega \sim \nu_{iz} < \nu_{in}$
Energy	$T_n \ll T_i \ll T_e \ll \epsilon_{iz}$

4.4 Linear Perturbation Analysis

Now, we conduct our linear perturbation analysis of Eqns. 4.36. We expand the outlet condition, using the convention $x = x_0 + x_1 e^{-i\omega t}$, where x_0 is the steady state condition and x_1 represents a small fluctuation on top of that steady state value. Consistent with the measurements in Chapter 3, we recognize that the density, electron temperature, electron

drift velocity, and anomalous collision frequency vary in time. We therefore allow these to be perturbed in the governing equations. We similarly note that the ionization and ion-neutral collision frequencies are an explicit function of density and cross section, which depends on electron temperature for ionization. These too are perturbed. First we establish the steady-state criteria, then we perturb each individual expression. The equations are then combined to determine the characteristic polynomial for the oscillation. This is analyzed and simplified, using the assumptions in Tab. 4.1.

4.4.1 Steady-state Conditions

Here we examine the steady state criteria and discuss them in the context of the mechanism we have proposed for the instability. First we begin with the ion continuity equation. We have that

$$\frac{n_0 T_0 - T_{e,in} n_{in}}{m_i \nu_{in,0} L^2} + 2\frac{n_0 T_{e0}}{m_i \nu_{in,0} R^2} = n_0 \nu_{iz,0} \ . \tag{4.37}$$

For the electron continuity equation we find

$$\frac{n_0 u_{e0} - n_{in} u_{e,in}}{L} = \frac{n_0 T_0 - T_{e,in} n_{in}}{m_i \nu_{in,0} L^2} + 2\frac{n_0 T_{e0}}{m_i \nu_{in,0} R^2} \tag{4.38}$$

$$\frac{n_0 u_{e0} - n_{in} u_{e,in}}{L} = n_0 \nu_{iz,0} \tag{4.39}$$

$$\frac{n_0 u_{e0}}{L} = n_0 \nu_{iz,0} + \frac{n_{in} u_{e,in}}{L} \ . \tag{4.40}$$

We interpret $n_{in} u_{e,in}$ as the current drawn from the plasma in the orifice region and $n_0 u_{e0}$ and the current demanded by the anode. This result implies that steady ionization in the plasma is able to supplement the current out of the cathode to meet the steady-state current required by the power supply. For the neutral continuity, we find that

$$\frac{n_{n,in}}{L} u_n = n_0 \nu_{iz} + \frac{n_{n0}}{L} u_n \ , \tag{4.41}$$

which states that the inlet neutral gas must be equal to the sum of the outlet and the losses to ionization. Alternatively, we can substitute in the steady-state electron continuity equation to show that

$$\frac{n_{n,in} - n_{n0}}{L} u_n = \frac{n_0 u_{e0} - n_{in} u_{e,in}}{L} \ . \tag{4.42}$$

This implies that neutral gas is consumed by ionization if the electron current demanded by the power supply is greater than the internal cathode plasma can provide. Lastly, examining the steady-state electron energy equation, we find that

$$\frac{T_{e0} u_{e0} - T_{e,in} u_{e,in}}{L} + \frac{1}{2} T_{e0} \frac{u_{e0} - u_{e,in}}{L} = m_e u_{e0}^2 \nu_{e0} - \epsilon_{iz} \nu_{iz,0} \ . \tag{4.43}$$

This result tells us that the outlet heat flux of the volume will be greater than the inlet heat flux if the electrons experience sufficient Ohmic heating to exceed the ionization losses.

In summary, the steady-state conditions we use for our perturbation are

$$\begin{aligned}
\frac{T_{e0} n_0 - T_{e,in} n_{in}}{m_i \nu_{iz,0} L^2} + 2 \frac{n_0 T_{e0}}{m_i \nu_{in,0} R^2} &= n_0 \nu_{in,0} \ , \\
\frac{n_0 u_{e0} - n_{in} u_{e,in}}{L} &= n_0 \nu_{iz,0} \ , \\
\frac{n_{n0} - n_{n,in}}{L} u_n &= n_0 \nu_{iz,0} \ , \\
\frac{T_{e0} u_{e0} - T_{e,in} u_{e,in}}{L} + \frac{1}{2} T_{e0} \frac{u_{e0} - u_{e,in}}{L} &= m_e u_{e0}^2 \nu_{e0} - \epsilon_{iz} \nu_{iz,0} \ .
\end{aligned} \tag{4.44}$$

Overall, these results make physical sense for the cathode plasma. Ionization is balanced by diffusion and is necessary to increase the current density in the plasma to maintain the discharge current. Conversely this can be expressed as the rate at which neutral gas must be consumed to ensure current continuity. This interpretation of the equations physically links the oscillations in discharge current to those in neutral density through the predator-prey mechanism. Lastly, the heat flux across the volume can be increased (as we found experimentally) if sufficient Ohmic heating occurs in the plasma to overcome losses due to

ionization.

4.4.2 Ion Continuity

Starting with the linear perturbation of the ion continuity equation,

$$\frac{\partial n}{\partial t} + \frac{nT_e - T_{e,in}n_{in}}{m_i\nu_{in}L^2} + 2\frac{nT_e}{m_i\nu_{in}R^2} = n\nu_{iz} \tag{4.45}$$

$$\nu_{in}\frac{\partial n}{\partial t} + \frac{nT_e - T_{e,in}n_{in}}{m_iL^2} + 2\frac{nT_e}{m_iR^2} = n\nu_{iz}\nu_{in} \tag{4.46}$$

$$-i\omega\nu_{in,0}n_1 + \left(\frac{n_1}{n_0} + \frac{T_{e1}}{T_{e0}}\right)\frac{n_0T_{e0}}{m_iL^2} + 2\frac{n_0T_{e0}}{m_iR^2}\left(\frac{n_1}{n_0} + \frac{T_{e1}}{T_{e0}}\right) = n_0\nu_{iz,0}\nu_{in,0}\left(\frac{n_1}{n_0} + 2\frac{n_{n1}}{n_{n0}} + \frac{\gamma_{iz}}{\nu_{iz,0}}\frac{T_{e1}}{T_{e0}}\right) . \tag{4.47}$$

Here we have defined $\gamma_{iz} \equiv T_{e0}\partial\nu_{iz}/\partial T_e$, which in physical terms represents the change in the ionization rate due to temperature variations. Mathematically, it is the result of a Taylor expansion of the ionization rate near the steady state temperature ($\nu_{iz} = \nu_{iz,0} + \frac{\partial\nu_{iz}}{\partial T_e}(T_e - T_{e0})$). Dividing by the ion-neutral collision rate, we find that

$$-i\omega n_1 + \left(\frac{n_1}{n_0} + \frac{T_{e1}}{T_{e0}}\right)\frac{n_0T_{e0}}{m_i\nu_{in,0}L^2} + 2\frac{n_0T_{e0}}{m_i\nu_{in,0}R^2}\left(\frac{n_1}{n_0} + \frac{T_{e1}}{T_{e0}}\right) = n_0\nu_{iz,0}\left(\frac{n_1}{n_0} + 2\frac{n_{n1}}{n_{n0}} + \beta\frac{T_{e1}}{T_{e0}}\right) , \tag{4.48}$$

where $\beta \equiv \gamma_{iz}/\nu_{iz,0}$ is a non-dimensional parameter. When $|\beta| \gg 1$, then temperature fluctuations are important i.e. the ionization rate has a greater than linear dependence on electron temperature, where as $|\beta| \ll 1$, then temperature fluctuations are not as important. For a low temperature xenon plasma, $\beta \sim \mathcal{O}(1-10)$. Greater T_e leads to smaller β. We apply the steady state condition and divide out by the outlet density.

$$-i\omega\frac{n_1}{n_0} + \left(\frac{n_1}{n_0} + \frac{T_{e1}}{T_{e0}}\right)\frac{n_{in}}{n_0}\frac{T_{e,in}}{m_i\nu_{in,0}L^2} = \nu_{iz,0}\left(2\frac{n_{n1}}{n_{n0}} + (\beta-1)\frac{T_{e1}}{T_{e0}}\right) \tag{4.49}$$

Now we will define $D_i = T_{e,in}/m_i\nu_{in,0}$, and $\nu_D = D_i/L^2$ is the diffusion rate of the plasma due to the ambipolar electric field balancing against the drag of ion-neutral collisions.

$$-i\omega\frac{n_1}{n_0} + \left(\frac{n_1}{n_0} + \frac{T_{e1}}{T_{e0}}\right)\frac{n_{in}}{n_0}\nu_D = \nu_{iz,0}\left(2\frac{n_{n1}}{n_{n0}} + (\beta - 1)\frac{T_{e1}}{T_{e0}}\right) \tag{4.50}$$

Dividing by the ionization rate to non-dimensionalize the equation, and defining $\zeta_i \equiv n_{in}\nu_D/n_0\nu_{iz,0}$ and $x = \omega/\nu_{iz,0}$ such that

$$\frac{n_1}{n_0}(-ix + \zeta_i) = 2\frac{n_{n1}}{n_{n0}} + \frac{T_{e1}}{T_{e0}}(\beta - 1 - \zeta_i) \tag{4.51}$$

Physically, when $\zeta_i \gg 1$ then the then diffusion losses are much greater than ionization and when $\zeta_i \ll 1$ then plasma production due to ionization is greater than the diffusion losses. Notably, in expression we find that if $\beta > \zeta_i + 1$, then changes in electron temperature will enhance the changes plasma density.

4.4.3 Electron Continuity

Conducting the perturbation of the electron continuity equation, we find

$$\frac{(nu_e - n_{in}u_{e,in})}{L} = \frac{nT_e - T_{e,in}n_{in}}{m_i\nu_{in}L^2} + 2\frac{nT_e}{m_i\nu_{in}R^2} \tag{4.52}$$

$$\nu_{in}\frac{(nu_e - n_{in}u_{e,in})}{L} = \frac{nT_e - T_{e,in}n_{in}}{m_iL^2} + 2\frac{nT_e}{m_iR^2} \tag{4.53}$$

$$\nu_{in,0}\left(\frac{n_0u_{e0} - n_{in}u_{e,in}}{L}\right)\left(\frac{n_{n1}}{n_{n0}}\right) + \nu_{in,0}\frac{n_0u_{e0}}{L}\left(\frac{n_1}{n_0} + \frac{u_{e1}}{u_{e0}}\right) = \left(\frac{n_1}{n_0} + \frac{T_{e1}}{T_{e0}}\right)\left(\frac{n_0T_{e0}}{m_iL^2} + 2\frac{n_0T_{e0}}{m_iR^2}\right). \tag{4.54}$$

Applying the steady state condition for the electron continuity equation simplifies the result to

$$\nu_{in,0}\left(\frac{n_0u_{e0} - n_{in}u_{e,in}}{L}\right)\left(\frac{n_{n1}}{n_{n0}} - \frac{T_{e1}}{T_{e0}}\right) + \nu_{in,0}\frac{n_0u_{e0}}{L}\left(\frac{u_{e1}}{u_{e0}}\right) + \nu_{in,0}\frac{n_{in}u_{e,in}}{L}\frac{n_1}{n_{in}} = \left(\frac{n_1}{n_0} + \frac{T_{e1}}{T_{e0}}\right)\frac{n_{in}T_{e,in}}{m_iL^2} \tag{4.55}$$

Now we nondimensionalize the expression by dividing by $\nu_{in} n_{in} u_{e,in}/L$ to find that

$$\left(\frac{n_0 u_{e0}}{n_{in} u_{e,in}} - 1\right)\left(\frac{n_{n1}}{n_{n0}} - \frac{T_{e1}}{T_{e0}}\right) + \frac{n_0 u_{e0}}{n_{in} u_{e,in}}\left(\frac{u_{e1}}{u_{e0}}\right) + \frac{n_1}{n_0} = \left(\frac{n_1}{n_0} + \frac{T_{e1}}{T_{e0}}\right)\frac{T_{e,in}}{m_i \nu_{in,0} L^2}\frac{L}{u_{e,in}} \ . \tag{4.56}$$

Multiplying through by $qA = q\pi R^2$, we can identify $\frac{n_0 u_{e0}}{n_{in} u_{e,in}} = \frac{I_0}{I_{in}} \equiv \iota$ where I_0 is the outlet current and I_{in} is the inlet current. The outlet current should be equal to the discharge current, by current continuity and the inlet current is the current that can be sourced from within the cathode tube. This is assumed to be constant because the plasma properties in this region do not oscillation. [2]

$$(\iota - 1)\left(\frac{n_{n1}}{n_{n0}} - \frac{T_{e1}}{T_{e0}}\right) + \iota\left(\frac{u_{e1}}{u_{e0}}\right) = \frac{n_1}{n_0}\left(\frac{T_{e,in}}{m_i \nu_{in} L^2}\frac{L}{u_{e,in}} - 1\right) \ . \tag{4.57}$$

Examining the first term on the right hand side, if we multiply by $u_{e,in}/u_{e,in}$, then we can write this in terms of the inlet electron Mach number, $M^2_{e,in} \equiv \frac{m_e u^2_{e,in}}{T_{e,in}}$ and the electron diffusion mean-free path, $\lambda_{Diff} \equiv u_{e,in}/\nu_{in}$. This gives

$$(\iota - 1)\left(\frac{n_{n1}}{n_{n0}} - \frac{T_{e1}}{T_{e0}}\right) + \iota\left(\frac{u_{e1}}{u_{e0}}\right) = \frac{n_1}{n_0}\left(\frac{m_e}{m_e}\frac{T_{e,in}}{m_i \nu_{in} L^2}\frac{u_{e,in} L}{u^2_{e,in}} - 1\right) \tag{4.58}$$

$$(\iota - 1)\left(\frac{n_{n1}}{n_{n0}} - \frac{T_{e1}}{T_{e0}}\right) + \iota\left(\frac{u_{e1}}{u_{e0}}\right) = \frac{n_1}{n_0}\left(\frac{u_{e,in}}{L\nu_{in}}\frac{1}{M^2_{e,in}}\frac{m_e}{m_i} - 1\right) \tag{4.59}$$

$$(\iota - 1)\left(\frac{n_{n1}}{n_{n0}} - \frac{T_{e1}}{T_{e0}}\right) + \iota\left(\frac{u_{e1}}{u_{e0}}\right) = \frac{n_1}{n_0}\left(\frac{\lambda_{Diff}}{L}\frac{1}{M^2_{e,in}}\frac{m_e}{m_i} - 1\right) \ . \tag{4.60}$$

Here, the first term is ultimately the result of fluctuations in the ionization rate, the second is due to changes in electron velocity and the last is due to changes in density. We can interpret this in terms of a circuit model, as illustrated in Fig. 4.6, where ionization acts as a current source in the plume and the IAT driven collisions act as an effective resistance for the electrons. Mathematically, we showed that if the inlet current is equal to the outlet current, i.e. $\iota = 1$, then the ionization term vanishes and the velocity and density are out of phase, meaning current is conserved in time. Physically, this makes sense because under

these conditions the cathode is producing exactly the current required by the anode and so no ionization is necessary in the plume. However, if there is a difference between the inlet and outlet currents, in other words the current produced by the cathode is insufficient to meet the current demanded by the power supply, then there must be some ionization in the plume. This can affect the phase between the density and velocity. In this manner, ionization can result in discharge current oscillations like those we observe experimentally even with only a small phase delay.

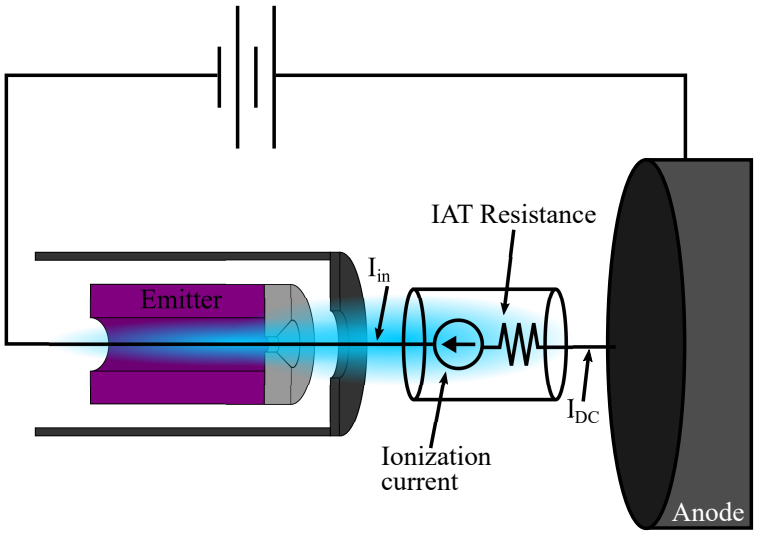

Figure 4.6: Circuit model of the cathode showing ionization as an additional current source for the system and a resistance driven by IAT driven collisions.

We can express this equation differently by applying the steady state condition again. It can be shown that $\iota - 1 = L/\lambda_{iz}$, where $\lambda_{iz} \equiv u_{e,in}/\nu_{iz}$ is the electron ionization mean free path. Therefore the result simplifies

$$\frac{L}{\lambda_{iz}}\left(\frac{n_{n1}}{n_{n0}} + \frac{u_{e1}}{u_{e0}} - \frac{T_{e1}}{T_{e0}}\right) + \frac{u_{e1}}{u_{e0}} = \frac{n_1}{n_0}\left(\frac{\lambda_{in}}{L}\frac{1}{M_{e,in}^2}\frac{m_e}{m_i} - 1\right) . \tag{4.61}$$

Experimentally, we know the electron Mach number is $\mathcal{O}(1)$, the ratio λ_{in}/L is between $10^2 - 10^3$ and $m_e/m_i \sim 10^{-6}$ (See Chapter 3), therefore, we can neglect this term and simplify

our expression to

$$\epsilon\left(\frac{n_{n1}}{n_{n0}}+\frac{u_{e1}}{u_{e0}}-\frac{T_{e1}}{T_{e0}}\right)+\frac{u_{e1}}{u_{e0}}=-\frac{n_1}{n_0}\ . \tag{4.62}$$

Here we have defined the nondimensional parameter $\epsilon = L/\lambda_{iz}$, which we know experimentally should be small for the cathode plasma, $\mathcal{O}(10^{-2} - 10^{-3})$.

4.4.4 Neutral Continuity

Now perturbing the neutral continuity equation,

$$\frac{\partial n_n}{\partial t}+\frac{n-n_{in}}{L}u_n=-n\nu_{iz} \tag{4.63}$$

$$\frac{n_{n1}}{n_{n0}}\left(-i\omega+\frac{u_n}{L}+\frac{n_0}{n_{n0}}\nu_{iz,0}\right)=-\frac{n_0}{n_{n0}}\nu_{iz,0}\left(\frac{n_1}{n_0}+\frac{\gamma_{iz}}{\nu_{iz}}\frac{T_{e1}}{T_{e0}}\right) \tag{4.64}$$

Applying the steady state condition for the neutral continuity equation and defining $\alpha \equiv n_0/n_{n0}$ and $\nu_{tn} \equiv u_n/L$, we find that

$$\frac{n_{n1}}{n_{n0}}\left(-i\omega+\frac{n_n^{in}}{n_{n0}}\nu_{tn}\right)=-\alpha\nu_{iz,0}\left(\frac{n_1}{n_0}+\frac{\gamma_{iz}}{\nu_{iz}}\frac{T_{e1}}{T_{e0}}\right) \tag{4.65}$$

Now applying previous definitions

$$\frac{n_{n1}}{n_{n0}}\left(-ix+\frac{n_n^{in}}{n_{n0}}\frac{\nu_{tn}}{\nu_{iz,0}}\right)=-\alpha\left(\frac{n_1}{n_0}+\beta\frac{T_{e1}}{T_{e0}}\right)\ . \tag{4.66}$$

Finally, we define $\Gamma_n \equiv \frac{n_n^{in}}{n_{n0}}\frac{\nu_{tn}}{\nu_{iz,0}}$, such that

$$\boxed{\frac{n_{n1}}{n_{n0}}\left(-ix+\Gamma_n\right)=-\alpha\left(\frac{n_1}{n_0}+\beta\frac{T_{e1}}{T_{e0}}\right)}\ . \tag{4.67}$$

Examining this equation, we see that when $\Gamma_n \gg 1$ then the influx of neutral gas greatly exceeds the losses by ionization, when $\Gamma_n \ll 1$, then ionization losses of neutral particles

exceeds the influx. When $\alpha \ll 1$ then the there are few plasma particles compared to neutrals and the fluctuations in temperature and density do not greatly affect the neutral density. If $\alpha \sim 1$ then the plasma is around 50% ionized, in which case plasma oscillations can affect the neutral density and vice-versa. Lastly, if $\alpha \gg 1$, then plasma density and temperature fluctuations can greatly influence the neutral density, but neutral density will only weakly affect the plasma. For there to be strong coupling between the neutrals and the plasma $\alpha \sim 1$. This has been observed numerically in some regions of the plume. [5] From a physics perspective, this expression indicates that large neutral density fluctuations can only be driven through ionization if the ratio of the plasma to neutral density is $\mathcal{O}(1)$ or greater.

4.4.5 Electron Energy

Now conducting our final perturbation on the electron energy equation.

$$\frac{3}{2}\frac{\partial T_e}{\partial t} + \frac{T_e u_e - T_{e,in}u_{e,in}}{L} + \frac{1}{2}u_e\frac{T_{e0} - T_{e,in}}{L} = m_e u_e^2 \nu_e - \epsilon_{iz}\nu_{iz} \tag{4.68}$$

$$-i\omega\frac{3}{2}T_{e1} + \left(\frac{T_{e1}}{T_{e0}} + \frac{u_{e1}}{u_{e0}}\right)\frac{u_{e0}T_{e0}}{L} + \frac{1}{2}\frac{u_{e1}}{u_{e0}}u_{e0}\frac{T_e - T_{e,in}}{L} + \frac{1}{2}\frac{T_{e1}}{T_{e0}}\frac{u_{e0}T_{e0}}{L} = m_e u_{e0}^2\nu_0\left(2\frac{u_{e1}}{u_{e0}} + \frac{\nu_1}{\nu_0}\right) - \epsilon_{iz}\nu_{iz,0}\left(\frac{n_{n1}}{n_{n0}} + \beta\frac{T_{e1}}{T_{e0}}\right), \tag{4.69}$$

where ν_1 is fluctuation in the collision frequency. Here we have allowed the electron collision frequency to fluctuate i.e. $\nu_1 \neq 0$. In later sections we will analyze this term to determine how different models for electron collisionality affect the the stability criterion. Applying the steady state conditions we find that

$$-i\omega\frac{3}{2}T_{e1} + \left(\frac{3}{2}\frac{T_{e1}}{T_{e0}} + \frac{u_{e1}}{u_{e0}}\right)\frac{u_{e,in}T_{e,in}}{L} = m_e u_{e0}^2\nu_0\left(\frac{u_{e1}}{u_{e0}} + \frac{\nu_1}{\nu_0} + \frac{T_{e1}}{T_{e0}}\right) - \epsilon_{iz}\nu_{iz,0}\left(\frac{n_{n1}}{n_{n0}} + (\beta - 1)\frac{T_{e1}}{T_{e0}} + \frac{u_{e1}}{u_{e0}}\right) \tag{4.70}$$

Now dividing out by $T_{e0}u_{e0}/L$ to nondimensionalize the equation, we arrive at

$$-i\frac{\omega}{u_{e0}/L}\frac{3}{2}\frac{T_{e1}}{T_{e0}}+\left(\frac{3}{2}\frac{T_{e1}}{T_{e0}}+\frac{u_{e1}}{u_{e0}}\right)\frac{u_{e,in}T_{e,in}}{u_{e0}T_{e0}}=M_e^2\frac{L}{\lambda_e}\left(\frac{u_{e1}}{u_{e0}}+\frac{\nu_1}{\nu_0}+\frac{T_{e1}}{T_{e0}}\right)-\frac{\epsilon_{iz}}{T_{e0}}\frac{L}{\lambda_{iz}}\left(\frac{n_{n1}}{n_{n0}}+(\beta-1)\frac{T_{e1}}{T_{e0}}+\frac{u_{e1}}{u_{e0}}\right), \tag{4.71}$$

where $\lambda_e = u_{e0}/\nu_0$ is the electron mean free path and $M_e \equiv u_{e0}/v_{e0}$ is the electron Mach number. We recall our previous definition, $x = \omega/\nu_{iz,0}$, and apply this such that

$$-ix\frac{L}{\lambda_{iz}}\frac{3}{2}\frac{T_{e1}}{T_{e0}}+\left(\frac{3}{2}\frac{T_{e1}}{T_{e0}}+\frac{u_{e1}}{u_{e0}}\right)\frac{u_{e,in}T_{e,in}}{u_{e0}T_{e0}}=M_e^2\frac{L}{\lambda_e}\left(\frac{u_{e1}}{u_{e0}}+\frac{\nu_1}{\nu_0}+\frac{T_{e1}}{T_{e0}}\right)-\frac{\epsilon_{iz}}{T_{e0}}\frac{L}{\lambda_{iz}}\left(\frac{n_{n1}}{n_{n0}}+(\beta-1)\frac{T_{e1}}{T_{e0}}+\frac{u_{e1}}{u_{e0}}\right). \tag{4.72}$$

From our experimental measurements we can estimate these lengths scales and show that L/λ_{iz} is very small compared to L/λ_e and $u_{e,in}T_{e,in}/u_{e0}T_{e0}$, therefore we neglect these terms

$$\left(\frac{3}{2}\frac{T_{e1}}{T_{e0}}+\frac{u_{e1}}{u_{e0}}\right)\frac{u_{e,in}T_{e,in}}{u_{e0}T_{e0}}=M_e^2\frac{L}{\lambda_e}\left(\frac{u_{e1}}{u_{e0}}+\frac{\nu_1}{\nu_0}+\frac{T_{e1}}{T_{e0}}\right) \tag{4.73}$$

Multiplying the left hand side by $Aqn_{in}n_0/Aqn_{in}n_0$, we can rewrite this as

$$\left(\frac{3}{2}\frac{T_{e1}}{T_{e0}}+\frac{u_{e1}}{u_{e0}}\right)\iota\frac{T_{e,in}}{T_{e0}}\frac{n_0}{n_{in}}=M_e^2\frac{L}{\lambda_e}\left(\frac{u_{e1}}{u_{e0}}+\frac{\nu_1}{\nu_0}+\frac{T_{e1}}{T_{e0}}\right) \tag{4.74}$$

$$\left(\frac{3}{2}\frac{T_{e1}}{T_{e0}}+\frac{u_{e1}}{u_{e0}}\right)\left(\frac{L}{\lambda_{iz}}+\frac{T_{e,in}}{T_{e0}}\frac{n_0}{n_{in}}\right)=M_e^2\frac{L}{\lambda_e}\left(\frac{u_{e1}}{u_{e0}}+\frac{\nu_1}{\nu_0}+\frac{T_{e1}}{T_{e0}}\right) \tag{4.75}$$

$$\left(\frac{3}{2}\frac{T_{e1}}{T_{e0}}+\frac{u_{e1}}{u_{e0}}\right)\left(\epsilon+\frac{T_{e,in}}{T_{e0}}\frac{n_0}{n_{in}}\right)=M_e^2\frac{L}{\lambda_e}\left(\frac{u_{e1}}{u_{e0}}+\frac{\nu_1}{\nu_0}+\frac{T_{e1}}{T_{e0}}\right). \tag{4.76}$$

Experimentally, we know that the inlet temperature is lower than the outlet and the inverse is true for the density. Therefore we define two parameters $\delta \equiv \frac{T_{e,in}}{T_{e0}}\frac{n_0}{n_{in}}$ and $\eta \equiv M_e^2\frac{L}{\lambda_e}$. From our previous experimental measurements, we know that in the presence of IAT driven electron collisions $\epsilon \ll \delta < \eta$; however, if the collision frequency were treated classically, then the hierarchy $\epsilon \ll \delta \sim \eta$ likely applies. In the following sections, we use these inequalities in our analysis to examine the stability criterion under different plasma conditions. Applying this

simplification, we arrive at our final expression for the perturbed electron energy equation:

$$\boxed{\left(\frac{3}{2}\frac{T_{e1}}{T_{e0}}+\frac{u_{e1}}{u_{e0}}\right)(\epsilon+\delta)=\eta\left(\frac{u_{e1}}{u_{e0}}+\frac{\nu_1}{\nu_0}+\frac{T_{e1}}{T_{e0}}\right)}. \tag{4.77}$$

4.4.6 Summary of Equations and Assumptions

Equation 4.78 shows the set of perturbed equations that we combine to solve for the dispersion.

$$\begin{aligned}
\frac{n_1}{n_0}(-ix+\zeta_i) &= 2\frac{n_{n1}}{n_{n0}}+\frac{T_{e1}}{T_{e0}}(\beta-1-\zeta_i)\\
\epsilon\left(\frac{n_{n1}}{n_{n0}}+\frac{u_{e1}}{u_{e0}}-\frac{T_{e1}}{T_{e0}}\right)+\frac{u_{e1}}{u_{e0}} &= -\frac{n_1}{n_0}\\
\frac{n_{n1}}{n_{n0}}(-ix+\Gamma_n) &= -\alpha\left(\frac{n_1}{n_0}+\beta\frac{T_{e1}}{T_{e0}}\right)\\
\left(\frac{3}{2}\frac{T_{e1}}{T_{e0}}+\frac{u_{e1}}{u_{e0}}\right)(\epsilon+\delta) &= \eta\left(\frac{u_{e1}}{u_{e0}}+\frac{\nu_1}{\nu_0}+\frac{T_{e1}}{T_{e0}}\right)
\end{aligned} \tag{4.78}$$

Table 4.2 shows all of the nondimensionalized parameters used in our analysis. The estimates in the nondimensional parameters are derived from experimental measurements in Chapter 3 and numerical simulations from Refs. [3–5, 55–57]. The complete list of estimates we have used is detailed in the table caption.

Table 4.2: Table of nondimensional parameters used in the derivation of the perturbed conservation equations. List of estimates: $L \sim \nabla n/n \simeq 0.01$ m, $T_{e,in} \sim 2$ eV, $T_{e0} \sim 5$ eV, $n_{in} \sim 10^{19}$ m^{-3}, $n_0 \sim 10^{18}$ m^{-3}, $n_{n,in} \sim 10^{20}$ m^{-3}, $n_{n0} \sim 10^{19}$ m^{-3}, $M_e \sim 1$, $u_n \sim \sqrt{k_B T_n/m_i} = 350$ m/s with $T_n \sim 2000$ K is the emitter temperature, $\nu_{iz} \sim 10^3 - 10^5$ Hz, $\lambda_{iz} \sim 10^1 - 10^3$ m, and $\nu_e \sim 10^6 - 10^9$ Hz.

Parameter	Definition	Estimate
ϵ	L/λ_{iz}	$\mathcal{O}(10^{-3} - 10^{-2})$
δ	$n_0 T_{e,in}/n_{in} T_{e,0}$	$\mathcal{O}(10^{-1})$
η	$M_e^2 L/\lambda_e$	$\mathcal{O}(10^{-1} - 10^{1})$
Γ_n	$n_{n,in} u_n/n_{n0}\nu_{iz} L$	$\mathcal{O}(10^{-1} - 10^{1})$
β	$\frac{\partial \nu_{iz}}{\partial T_e} T_{e0}/\nu_{iz}$	$\mathcal{O}(10^{0} - 10^{1})$
ζ_i	$n_{in}\nu_{Di}/n_0\nu_{iz}$	$\mathcal{O}(10^{-2} - 10^{2})$
α	n_0/n_{n0}	$\mathcal{O}(10^{-1} - 10^{1})$

4.5 Oscillation and Growth

In this section, we examine how different models for the electron collision frequency affect the stability of the system of equations in Eqn. 4.78. We analyze three models that could be relevant to this problem and are consistent with the assumptions that we have made in the development of the governing equations. These cases are

- Coulomb collisions
- Large constant collisions
- Saturated anomalous collisions Sagdeev

Within each of the following sections we use appropriate limits for the various non-dimensional parameters to simplify the problem and gather new insight into the result.

4.5.1 Coulomb Collisions

Although the conditions in the laboratory will not allow Coulomb collisions to dominate, (the IAT is always excited in the experiment and is the dominant form of resistivity in the plume) we first analyze the case where the electron collision frequency is low but dominated by this process. This example serves to illustrate the importance of an enhanced collision for the onset of the plume mode ionization wave.

In the classical limit, Coulomb collisions are $\nu_{ei} \propto nT_e^{-3/2}$, therefore the electron energy equation in Eqn. 4.78 is modified to be

$$\left(\frac{3}{2}\frac{T_{e1}}{T_{e0}} + \frac{u_{e1}}{u_{e0}}\right)(\epsilon + \delta) = \eta\left(\frac{u_{e1}}{u_{e0}} + \frac{n_1}{n_0} - \frac{1}{2}\frac{T_{e1}}{T_{e0}}\right) . \tag{4.79}$$

We used an algebraic solver (Mathematica) to manipulate and concurrently solve this system of equations, thereby arriving at a second order characteristic polynomial, i.e. the dispersion relation, for this problem. For the classical collision case, we set $\epsilon \ll 0.1 \sim \delta \sim \eta$. This

is consistent with fact that when the collision frequency is low, there is little heating and the ionization rate remains low in the plume. This keeps ϵ small and $\delta, \eta < 1$. To simplify the final expression and investigate the driving physics, we have explicitly set $\delta = \eta$. The trends we find generally hold for $\delta > \eta$, i.e. a collisionless plasma. Note $\delta < \eta$ can only be achieved with enhanced collisionality in the plume, per our estimates in Tab. 4.2, and will be discussed later. The result of this calculation is

$$D(x) = x^2 + ix\left(\Gamma_n + \zeta_i\right) - 2\alpha - \Gamma_n\zeta_i. \tag{4.80}$$

We can expand the dispersion assuming the real part is much larger than the imaginary part to solve for the real and imaginary frequencies

$$\epsilon_r(x_r) \simeq 0\ , \qquad x_i \simeq -\left.\frac{\epsilon_i(x)}{\frac{d\epsilon_r}{dx}}\right|_{x=x_r} \tag{4.81}$$

where ϵ_r and ϵ_i are the real and imaginary parts of the dispersion, respectively and x_r and x_i are the real and imaginary parts of the frequency. Solving this system of equations

$$\begin{aligned} x_r &= \sqrt{2\alpha + \Gamma_n\zeta_i} \\ x_i &= -\frac{\Gamma_n + \zeta_i}{2}\ . \end{aligned} \tag{4.82}$$

From Eqn. 4.82, we find that there is indeed a real component and an imaginary component with a growth rate. Solving for this in terms un-normalized parameters, we find that the real frequency, ω_r, and growth rate, γ, are

$$\omega_r = \sqrt{2\alpha\nu_{iz,0}^2 + \frac{n_{n,in}}{n_{n0}}\frac{u_n}{L}\frac{n_{in}}{n_0}\nu_D} \tag{4.83}$$

$$\gamma = -\frac{1}{2}\left(\frac{n_{n,in}}{n_{n0}}\frac{u_n}{L} + \frac{n_{in}}{n_0}\nu_D\right)\ . \tag{4.84}$$

The first term in the expression for the oscillation frequency is the same result as found by

Fife et. al. [37]. The second term is always positive and is related to the inlet of neutrals by convection and ions by diffusion. The real frequency scales with the ionization rate and inlet properties, as we might expect from predator-prey process between the neutrals and electrons. Using our experimental estimates, we find that $f = \omega_r/(2\pi)$ is between $1-100$ kHz and is consistent with our observations of the wave. The calculated growth rate indicates that the wave is always damped by diffusion and the atom influx. Using the estimates from Tab. 4.2, we find that $\gamma \sim -40$ kHz to -1000 kHz, meaning it is strongly damped. Physically, for every cycle of the predator-prey oscillation a positive perturbation in the plasma density will diffuse outwards and ultimately decay in time and a negative perturbation of the neutral density will be filled in by the inlet of neutral gas. This is a similar situation to what has been found in predator-prey models of Hall thrusters where the influx of neutral gas also unconditionally damps the oscillation. An interesting implication of our result is that it predicts that any classical simulation of the cathode plasma will be unable to resolve the plume mode instability. Historically, this has been the case in numerical simulations of hollow cathodes that do not take into account the effects of IAT in the plume region.

To summarize this analysis, we have found by assuming that electrons are primarily subject to classical, Coulomb collisions that we can predict the existence of an ionization instability with a real frequency that scales with the ionization rate and follows established predator-prey trends. This result is consistent with our experimental expectations. Under these conditions, however, we find that the mode is always damped out by diffusion and the atom influx, which means that the instability cannot be classically predicted.

4.5.2 Anomalous Collisions: Constant

Comparisons of simulations with experiments have indicated that the collision frequency in the plume is in fact much larger than the Coulomb collision frequency. One could possibly choose to model this phenomenon as a large, constant collision frequency. In this case $\nu_e = C$, which implies $\nu_1 = 0$. Furthermore with a relatively large collision frequency, we can apply

the hierarchy $\epsilon \ll \delta < 1 \ll \eta$. In this situation, the electron energy equation in Eqn. 4.78 becomes

$$0 = \left(\frac{u_{e1}}{u_{e0}} + \frac{T_{e1}}{T_{e0}} \right) . \tag{4.85}$$

Physically this expression is saying when the steady state energy flux through the volume is small compared to the heating from collisions, the temperature and velocity will fluctuate out of phase with each other. Now we use this expression to solve for the dispersion using computational symbolic manipulation tools. The result is

$$D(x) = x^2 - ix\left(\beta - 1 - \Gamma_n - 2\zeta_{iz}\right) - 2\alpha\left(1 + \beta\right) - 2\left(1 + \zeta_i\right)\Gamma_n \ . \tag{4.86}$$

Assuming that the complex part of the dispersion is much smaller than the real part, we find that

$$x_r = \sqrt{2\alpha(1+\beta) + (1 - \beta + 2\zeta_i)\Gamma_n} \tag{4.87}$$

$$x_i = \frac{\beta}{2} - \frac{1 + \Gamma_n}{2} - \zeta_i \ . \tag{4.88}$$

Unpacking this expression in terms of an oscillation frequency and growth rate, we find that

$$\omega_r = \sqrt{2\alpha(\nu_{iz,0}^2 + \gamma_{iz}\nu_{iz,0}) + \left(\nu_{iz} - \gamma_{iz} + 2\frac{n_{in}}{n_0}\nu_{D0}\right)\frac{n_{n,in}}{n_{n0}}\frac{u_n}{L}} \tag{4.89}$$

$$\gamma = \frac{\gamma_{iz}}{2} - \frac{\nu_{iz,0}}{2} - \frac{1}{2}\frac{n_{n,in}}{n_{n0}}\frac{u_n}{L} - \frac{n_{in}}{n_0}\nu_{D0} \ . \tag{4.90}$$

As with the Coulomb collision case, we found that the frequency of oscillation scales with ionization processes, which is consistent with experimentally derived scaling for the frequency of oscillation. [2] Using the estimates in Tab. 4.2, the real frequency of oscillation, $f = \omega_r/(2\pi)$, is between 1 and 1000 kHz. The wide range is largely due to nonlinear dependence of the ionization frequency on electron temperature over our expected range. The growth rate now

has an onset criterion, where if the plasma production due to temperature fluctuations is large compared to diffusion and the influx of neutral gas, then the wave becomes unstable. Using the estimates in Tab. 4.2, we find that the growth rate is around $\gamma \sim 10^5$ Hz at $T_e = 5$ eV while $\gamma \sim -10^5$ Hz at $T_e = 2$ eV. An interesting feature of our onset criterion is that if we remove electron temperature fluctuations, then $\gamma_{iz} \to 0$ and the wave is damped by diffusion and ionization. This underscores the importance of including temperature fluctuations for resolving this type of instability and supports the physical interpretation shown in Sec 4.2.

4.5.3 Anomalous Collisions: Sagdeev

More recent numerical simulation of hollow cathodes [5] a saturated model for the turbulence derived by Sagdeev,

$$\nu_{an} = \alpha_{IAT} \omega_{pe} M_e \frac{T_e}{T_i} \tag{4.91}$$

where α is a constant of order 10^{-2}. Including in the energy equation, under the assumption that the ion temperature does not fluctuate strongly, we find that

$$\left(\frac{3}{2}\frac{T_{e1}}{T_{e0}} + \frac{u_{e1}}{u_{e0}}\right)(\epsilon + \delta) = \eta\left(2\frac{u_{e1}}{u_{e0}} + \frac{1}{2}\frac{n_1}{n_0} + \frac{3}{2}\frac{T_{e1}}{T_{e0}}\right) . \tag{4.92}$$

This is only a slight modification of the energy equation from what we found with the previous Sagdeev model. Making the same assumption that electrons experience many collisions ($\eta \gg \delta \gg \epsilon$) and solving for the dispersion, we arrive at

$$D(x) = x^2 - ix\,(\beta - 1 - \Gamma_n - 2\zeta_{iz}) - 2\alpha\,(1 + \beta) - 2\,(1 + \zeta_i)\,\Gamma_n \ . \tag{4.93}$$

The frequency and growth rate in the limit that the imaginary component of the dispersion is small compared to the real component are

$$\omega_r = \sqrt{2\alpha(\nu_{iz,0}^2 + \gamma_{iz}\nu_{iz,0}) + \left(\nu_{iz} - \gamma_{iz} + 2\frac{n_{in}}{n_0}\nu_{D0}\right)\frac{n_{n,in}}{n_{n0}}\frac{u_n}{L}} \tag{4.94}$$

$$\gamma = \frac{\gamma_{iz}}{2} - \frac{\nu_{iz,0}}{2} - \frac{1}{2}\frac{n_{n,in}}{n_{n0}}\frac{u_n}{L} - \frac{n_{in}}{n_0}\nu_{D0}\ . \tag{4.95}$$

The result is identical to the large, constant collision frequency case. This shows that we simply require that the collision frequency be large enough, such that the plasma can be effectively Ohmically heated to overcome diffusion losses and the influx of neutral gas that resulted in damping for the Coulomb collision case. This is to say that enhanced Ohmic heating due to IAT is a real physical mechanism that can lead to the destabilization of the plasma by modulating the electron temperature.

4.5.4 Evaluation of the Onset Criterion

Next we seek to evaluate our wave properties, the frequency and growth rate, by using our measurements from Chapter 3. We choose to use Eqns. 4.94 and 4.95 for this assessment, because when we evaluate ϵ, δ, and η, we find that $\eta \gg \delta, \epsilon$. When applying the results in Fig. 3.13d, our model predicts a frequency of 57 kHz and a growth rate of 15 kHz at the location of peak electron temperature fluctuations. Given the measured frequency of oscillation is 40 kHz, we have found good agreement between our first-principles models and the experiment. Overall, using our previous experimental results, we find that the theory both qualitatively and quantitatively describes the properties of the hollow cathode plume mode instability.

4.6 Onset in Experimental Context

Now, our goal to interpret this onset criterion in Eqn. 4.95 in an experimental context to see how our derived criterion compares with the known empirical dependence on discharge current and mass flow rate. The expression in Eqn. 4.95 is rather complicated and depends on the electron temperature, neutral density, neutral velocity, and density gradients. To arrive at some insight, we will need to simplify this expression by making assumptions on the dominant damping mechanisms. We know that $\nu_{iz} \ll \gamma_{iz}$ for the electron temperatures in the plume. Examining the third and fourth terms in Eqn. 4.95 using the experimental measurements from Chapter 3, we find that these could be comparable. For the sake of simplicity we take two limits, one where damping by neutral influx dominates and the other where diffusion dominates.

4.6.1 Diffusion Damping

If we assume that damping by diffusion dominates, then the expression for onset reduces to

$$\frac{\partial \nu_{iz,0}}{\partial T_e} > 2\frac{n_{in}}{n_0}\frac{1}{m_i \nu_{in} L^2} \tag{4.96}$$

$$\nu_{iz,0} > 2\frac{n_{in}}{n_0}\nu_{D0} \tag{4.97}$$

The ionization rate and diffusion rate primarily depend on temperature and neutral density and therefore we suspect that this leads to a critical temperature for the onset of the ionization oscillation that depends on the neutral density. We use a closed form expression for the ionization rate [6] given by

$$\nu_{iz,0} = n_{n0}\sigma_0 \left(3.97 + 0.643 T_{e0} - 0.0368 T_{e0}^2\right) e^{-\epsilon_{iz}/T_{e0}} \sqrt{\frac{8}{\pi}\frac{T_{e0}}{m_e}} \tag{4.98}$$

to solve for this temperature. Combining with Eqn. 4.97, leaves us with a transcendental equation for the critical electron temperature, T_e^{crit}, for onset. To simplify the problem, we

curve fit in expression in Eqn. 4.98 with the form

$$\nu_{iz,0} \simeq n_{n0} a \sqrt{T_{e0}} \sigma_0 e^{-\epsilon_{iz}/T_{e0}} \sqrt{\frac{8}{\pi} \frac{T_{e0}}{m_e}} \ . \tag{4.99}$$

The result is $a = 2.88 \pm 0.2$, when we restrict the curve fit to temperatures between $0-5$ eV. Combining with Eqn. 4.97, and solving for the critical electron temperature we find that

$$T_{e0}^{crit} = \frac{\epsilon_{iz}}{\ln\left(n_{n0} \frac{n_0}{n_{in}} \nu_{in,0} a \sigma_0 \sqrt{\frac{8}{\pi} \frac{m_i}{q m_e}} \sqrt{m_i} L^2\right)} \tag{4.100}$$

In Fig. 4.7 we plot this parameter as a function of neutral density and find that lower neutral densities leads to a greater critical temperature. For most of the range, of densities, the onset temperature is between 1 and 10 eV. From this expression there is a critical neutral density above which there exists an onset temperature. From our estimates in Tab. 4.2, we find this neutral density to be 1.5×10^{19} m^{-3}. If we Taylor expand this expression to 0^{th} order, and take the limit that we are relatively far from this critical density, then we find that $T_e^{crit} \sim \epsilon_{iz}/4 \sim 3$ eV. A constant critical electron temperature may be found if the wave is excited near the orifice, where the atom density is high.

Ultimately, what we have found at is that the electron temperature and neutral density are the critical plasma parameters that dictate the onset of the ionization wave. We interpret this result as a critical temperature for a given mass flow rate to the cathode for the onset of the plume mode. This concept will be explored in a later section. Physically, this makes sense for an ionization wave in the context a predator-prey mechanism. The more energy (T_e) in the system, the less fuel (n_n) you need for the wave to onset. Conversely, when more fuel (n_n) is available less energy (T_e) is necessary for instability. This tells us that a cold plasma and few atoms tend to be more stable than a hot plasma with dense neutrals. An interesting feature of our result is that if the neutral gas can be rarefied below a critical threshold, then the plasma is always stable. We can think of the plasma as having insufficient fuel for the

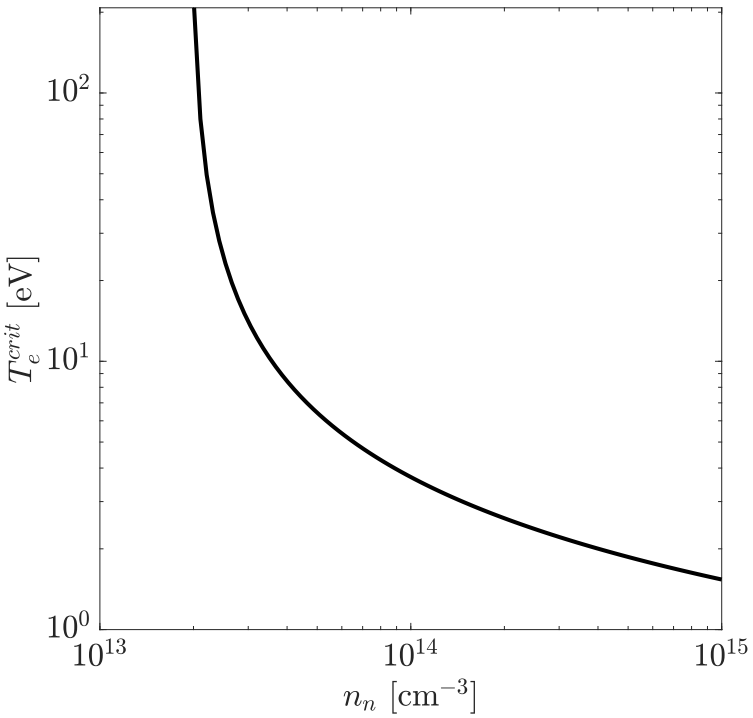

Figure 4.7: Estimation of the critical electron temperature for onset as a function of neutral density under the assumption that damping by diffusion dominates.

instability to grow, regardless of the temperature.

4.6.2 Neutral Influx Damping

Alternatively, we could assume that the dominant form of damping is the influx of neutral particles to the plume from the cathode. In this scenario,

$$\frac{\partial \nu_{iz,0}}{\partial T_e} > \frac{n_{n,in}}{n_{n0}} \frac{u_n}{L} \frac{1}{T_e} \tag{4.101}$$

$$\nu_{iz,0} > \frac{n_{n,in}}{n_{n0}} \frac{u_n}{L} \ln(T_e) \tag{4.102}$$

Given the expression for the ionization rate in Eqn. 4.98, this is yet another transcendental equation. To simplify the problem, we curve fit in expression in Eqn. 4.98 with the form

$$\nu_{iz,0} \simeq n_{n0} b \ln(T_{e0}) \sigma_0 e^{-\epsilon_{iz}/T_{e0}} \ , \tag{4.103}$$

where b is a fit parameter. The result of the regression is $b = (6 \pm 0.01) \times 10^6$, when we restrict the curve fit to temperatures between $1 - 5$ eV. This allows us to solve the equation for a critical electron temperature as a function of neutral density:

$$T_e^{crit} = \frac{\epsilon_{iz}}{\ln\left(n_{n0}\frac{n_{n0}}{n_{n,in}}\frac{Lb\sigma_0}{u_n}\right)} \tag{4.104}$$

We have arrived at a similar expression to Eqn. 4.100 where the critical temperature is a fraction of the ionization energy. In this expression there are a few key points that we would like to make. First, is that $n_{n0}/n_{n,in}$, L, b, and u_n are all likely weak functions of operating parameters such as discharge current and mass flow rate. The second is that this new expression has a weaker dependence on n_{n0}. This property is illustrated by Fig. 4.8 where over the domain of the neutral density (two orders of magnitude), the critical electron temperature only changes by less than a factor 10 compared to the three orders of magnitude in Fig. 4.7. Under the assumption that the damping of the wave is primarily due to the influx of atoms, we find that the critical temperature is much less sensitive to the actual neutral density. Therefore if this condition holds, we can conclude that in the region near the orifice, where the wave tends to onset and where the atom density is relatively high, the critical electron temperature for onset is approximately independent of the neutral density. This is an interesting finding which we explore further in the following sections.

4.6.3 Interpretation of the Critical Electron Temperature

Based on Figs. 4.7 and 4.8, at higher neutral density, like those found near the cathode, the onset criterion for the plume mode wave can be expressed as

$$T_e > T_e^{crit} \ . \tag{4.105}$$

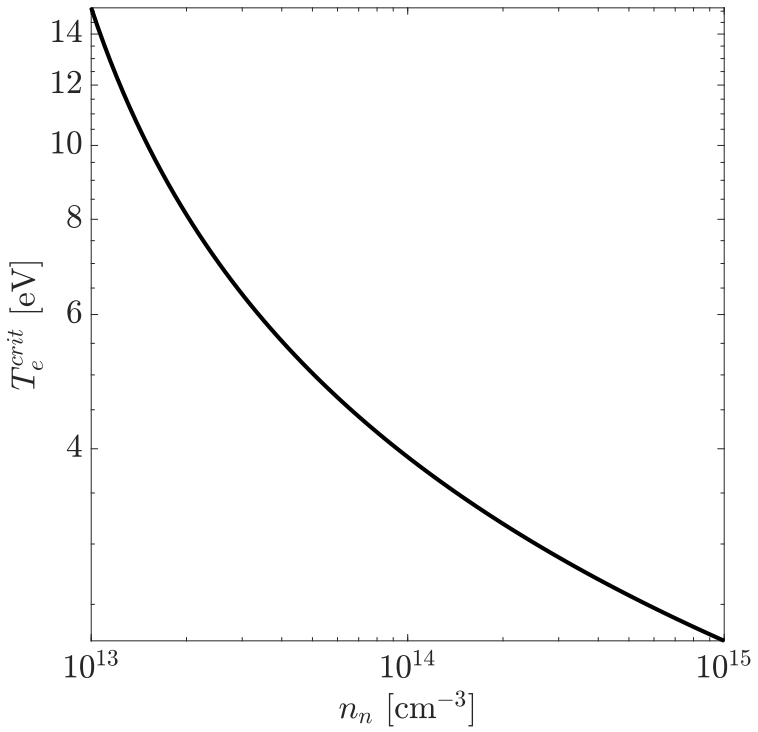

Figure 4.8: Estimation of the critical electron temperature for onset as a function of neutral density under the assumption at damping from neutrals dominates.

Using Eqn. 4.44 we can show that if the inlet temperature and velocity are much smaller than the outlet, and ionization losses are minimal, then

$$\frac{T_{e0}u_{e0} - T_{e,in}u_{e,in}}{L} + \frac{1}{2}T_{e0}\frac{u_{e0} - u_{e,in}}{L} = m_e u_{e0}^2 \nu_{e0} - \epsilon_{iz}\nu_{iz,0} \tag{4.106}$$

$$\frac{3}{2}\frac{T_{e0}u_{e0}}{L} \simeq m_e u_{e0}^2 \nu_{e0} \tag{4.107}$$

Using the electron momentum equation (Eqn. 4.7), under the assumption that anomalous collisions are dominant in the plume, we find that

$$\frac{3}{2}T_{e0}\frac{u_{e0}}{L} = (m_e u_{e0}\nu_{an})\,u_{e0} \tag{4.108}$$

$$\frac{3}{2}T_{e0}\frac{u_{e0}}{L} = (-E_0 - T_{e0})\,u_{e0} \tag{4.109}$$

$$\frac{3}{2}T_{e0}\frac{1}{L} = \left(\frac{\Delta V}{L} - T_{e0}\right) \tag{4.110}$$

$$\frac{5}{2}T_{e0} = \Delta V \tag{4.111}$$

where ΔV is the voltage difference across the gradient lengthscale. Our estimates place the critical electron temperature is around $2-3$ eV, therefore the critical voltage difference across the length scale is around $5-7.5$ V. Combining this finding with our measurements in Fig. 3.4 we estimate the critical electric field for growth to be between -15 to -20 V/cm. In Fig. 3.13a, we find that this condition is only met near the cathode, notably in the region where peak-to-peak electron temperature fluctuations are rising in Fig. 3.15.

Returning to our goal of re-expressing the critical electron temperature in terms of discharge parameters, we know that the anode is typically placed only a few gradient lengthscales away from the cathode. Therefore we can rewrite Eqn. 4.111 as

$$\frac{5}{2}T_e^{crit} = \Delta V^{crit} \tag{4.112}$$

$$\frac{\ell_{ca}}{L}\frac{5}{2}T_e^{crit} = V_{dc}^{crit}\ , \tag{4.113}$$

where ℓ_{ca} is the cathode to anode distance and the ratio ℓ_{ca}/L is of order $3-10$ based on the measurements in Chapter 3. Using the lower bound and our estimate of the onset temperature, we find that the critical discharge voltage will be on the order of 20 V. This implies that we can express the onset criterion in terms of the discharge voltage.

$$V_{dc} > V_{dc}^{crit} \tag{4.114}$$

Physically, this result suggests that the electron temperature scales with voltage (expected for Ohmic heating) and temperature needs to exceed a certain value for onset of the mode. We have arrived at an onset criterion that is in terms of discharge parameters, however, typically we operate hollow cathodes in current control, meaning we do not explicitly set the discharge voltage. In most cases, we can control the discharge current and the mass flow rate to the device. As such, we rewrite the expression for onset as

$$I_{dc}R_{dc} > V_{dc}^{crit} \tag{4.115}$$

$$I_{dc}\frac{\rho \ell_{ca}}{A_o} > V_{dc}^{crit} \ , \tag{4.116}$$

where ρ is the average resistivity of the plasma, ℓ_{ca} is the cathode to anode distance and A_o is the area of the orifice. Although different from the empirical stability criterion, $I/\dot{m} > \mathcal{C}$, our result has similar features. For example, by increasing the discharge current and cathode to anode distance is known to lead to instability. Consistent with known design laws, this suggests that reducing the orifice size with also lead to a more unstable cathode. What is harder to determine is the influence of the propellant flow rate on the condition. We know the resistivity of the plasma depends primarily on the anomalous collision frequency and ν_{an}. Previous analyses have shown that the anomalous collision frequency roughly scales as $\nu_{an} = (W/nT_e)\omega_{pe}$ (Eqn. 2.3), where again W is the wave energy density of the turbulence. Previous experimental results show that by decreasing mass flow rate to the cathode, we can increase the amplitude of the turbulence and therefore the resistivity; however, this effect is not immediately apparent in Eqn. 2.3. To be able to capture this effect, we examine a nonlinear saturation model for the IAT where saturation is assumed to be the result of nonlinear ion Landau damping. This is a modified version of the Sagdeev scaling from Ref. [88]. The IAT wave energy for a given mode is determined by

$$\frac{\partial W_k}{\partial t} \simeq W_k\left(\omega_r M_e - \frac{1}{2}\nu_{in}\right) - \frac{T_i}{T_e}\omega_r \frac{W_k^2}{nT_e} \ , \tag{4.117}$$

When the wave energy saturates, the left hand side of the equation vanishes such that

$$W_k = \frac{\omega_r M_e - \frac{1}{2}\nu_{in}}{\omega_r}\frac{T_e}{T_i} n T_e \tag{4.118}$$

Summing over modes, the total saturated wave energy is

$$W_{sat} \simeq \left(M_e - \frac{1}{2}\frac{\nu_{in}}{\omega_{pi}} \right) \frac{T_e}{T_i} n T_e \ . \tag{4.119}$$

By substituting into our expression for the anomalous collision frequency we find that

$$\nu_{an}^{sat} \simeq \omega_{pe} \left(M_e - \frac{1}{2}\frac{\nu_{in}}{\omega_{pi}} \right) \frac{T_e}{T_i} \tag{4.120}$$

$$\nu_{an}^{sat} \simeq \nu_{an} - \psi \nu_{in} \ , \tag{4.121}$$

where ψ is a non-dimensional parameter. This is ultimately a modification to the result used by Mikellides and tells us that by limiting the growth rate of the IAT, ion neutral collisions are able to reduce the saturated wave energy and therefore collision frequency. Since ion-neutral collisions depend on the neutral density, this result indicates that the resistivity of the plasma will ultimately depend on the mass-flow rate to the cathode, background pressure, and the anode location – global experimental parameters that influence the local neutral density in the plume. Now, in terms of global discharge parameters, the resistivity and onset criterion are

$$\rho = \frac{m_e \nu_{an}^{sat}}{q^2 n} = \frac{m_e \nu_{an} - m_e \psi \nu_{in}}{q^2 n} = \frac{m_e \nu_{an} - m_e \Psi \frac{\dot{m}}{m_i}}{q^2 n} = \rho_{an} + \rho_{in}(\dot{m}) \tag{4.122}$$

$$I_{dc} \frac{(\rho_{an})\, \ell_{ca}}{A_o} > V_{dc}^{crit} + V_{in} \ , \tag{4.123}$$

where ρ_{in} and V_{in} are the reduced electron resistivity and enhanced critical voltage due to ion-neutral collisions damping the turbulence. In this expression, we find that increasing the mass flow rate will lead to a reduction in the overall resistance in the plasma by ultimately

reducing the IAT amplitude. This can be interpreted as some additional voltage that must be achieved for the onset of the wave. Looking more closely at the anomalous resistivity we can also show that it depends on the mass flow rate, under certain assumptions. Examining the Mach number,

$$\rho_{an} = \frac{m_e \nu_{an}^{sat}}{q^2 n} = \frac{m_e M_e \omega_{pe}}{q^2 n} = \frac{m_e \omega_{pe}}{q^2 n} \frac{u_e}{v_e} \frac{qnA_o}{qnA_o} = \frac{m_e \omega_{pe}}{q^2 n} \frac{I_{dc}}{I_{th}} \tag{4.124}$$

assuming that the density ratio, α, is relatively fixed, we can write

$$\rho_{an} = \frac{m_e \omega_{pe}}{q^2 \alpha n_n} \frac{I_{dc}}{I_{th}} = \frac{m_e \omega_{pe}}{q^2 \alpha n_n} \frac{I_{dc}}{I_{th}} \frac{A_o m_i u_n}{A_o m_i u_n} = \frac{m_e m_i A_o u_n \omega_{pe}}{q^2 \alpha \dot{m}} \frac{I_{dc}}{I_{th}} \tag{4.125}$$

Therefore, we find that the onset criterion can be expressed as

$$\frac{I_{dc}}{I_{th}} \frac{I_{dc}}{\dot{m}} > q^2 \left(V_{dc}^{crit} + V_{in} \right) \frac{\alpha}{m_e m_i \omega_{pe} u_n \ell_{ca}} , \tag{4.126}$$

Here we have recovered from our theoretical expression the typical scaling for the plume mode instability, but is modified by the ratio of the discharge current to the thermal current. This result is reminiscent of the current imbalance hypothesis discussed in Chapter 2. If the discharge current exceeds the thermal current then the ionization instability onsets.

In conclusion, we are able to show that the onset criterion we have derived is largely consistent with previous experimental indications for the plume mode onset and empirical design principles. Furthermore, the interpretation of the stability criterion is similar to previous descriptions such as predator-prey, striations, and current imbalance. With experimental validation, the new derived scaling law may prove useful for evaluating novel designs that can mitigate the plume mode oscillation.

4.7 Conclusions

To summarize our theoretical analysis, we started with a predator-prey picture that we argued could be destabilized by the presence of electron temperature oscillations in a manner that is consistent with our experimental measurements in Chapter 3. From this interpretation of the experimental results, we developed a three-fluid model for the electrons, ions, and neutrals assuming quasineutrality and allowing for temperature fluctuations to influence the ionization rate. We simplified the equations using a velocity, frequency, and energy hierarchy and applied a 0 dimensional approximation that is consistent with our experimental observations and those of others. We perturbed these equations allowing the electron collision frequency to vary. We analyzed different models for how the frequency changes based on background plasma parameters and showed that without sufficient collisions, diffusion and the neutral influx to the plume will damp any perturbation in plasma density. However, in the presence of an IAT-driven resistivity the wave will oscillate near the ionization frequency and can grow if the temperature is sufficiently high and allowed to fluctuate. Physically, the oscillation can be described as a predator-prey oscillation where out-of-phase temperature variations lead to instability. If plasma production by ionization exceeds the losses from diffusion, then with each cycle the plasma density increases. Here, the IAT plays two important roles for stability. First, it enhances the electron temperature and second, it provides a mechanism by which the temperature of the electrons can vary in time. This criterion was shown to be equivalent to a critical discharge voltage that depends weakly on the neutral density and is necessary for onset of the plume mode. Furthermore we manipulated the expression for onset and found that it can be re-expressed as the ratio of the discharge current to the mass flow rate, scaled by the ratio of the discharge current to thermal current. This finding is largely in agreement with previous interpretations of the instability.

CHAPTER 5

Experimental Evaluation of the Stability Criterion

5.1 Introduction

In this Chapter, we discuss our experimental evaluation of the predator-prey oscillation we derived in Chapter 4. The real frequency of oscillation and stability criterion can be calculated from Eqns. 4.94 and 4.95. To do this, we must primarily evaluate the electron temperature, the gradient lengthscale, neutral velocity, and neutral density in the plume. Without sophisticated diagnostics for the neutrals, we will need to estimate the their velocity and their density using a model derived from continuity. To this end, first we describe our experimental methods and then present the results. We show the steady-state plasma parameters and wave properties and a function of discharge current, mass flow rate, and position. These values are then used to assess the theory over this wide parameter sweep and the results are discussed in context of the numerical simulations of others.

5.2 Experimental Methods

For this experiment, we used a 20 A LaB_6 hollow cathode with a 3 mm tungsten orifice and a graphite keeper electrode. We varied the xenon mass flow rate to the device between 20 sccm and 5 sccm to observe the mode transition (see Fig. 2.8). The anode was placed 45 mm

downstream of the cathode exit and the discharge current was also varied between 15 and 35 A with 5 A resolution. Figure 5.1 shows the experimental setup for this investigation. The cathode test facility base pressure was 0.7 μTorr, which is achieved by cryogenic pumping. During the experiment, the background pressure in the facility was between 50 and 500 μTorr-Xe, depending on the operating condition. To measure the steady state plasma properties, we used a Langmuir probe made of tungsten that was 2 mm long and 0.1 mm in diameter. The bias voltage was measured and swept using a Keithley sourcemeter. This probe was also used to measure the ion saturation current at 10 MHz to examine the amplitude of the IAT. The probes were moved along the discharge axis over a range of 20 mm with a spatial resolution of 2 mm. From the I-V trace we are able to extract important parameters such as the electron temperature and plasma density. These are used to compute Eqns. 4.94 and 4.95. These theoretical values are compared to the wave properties of the discharge current oscillations that were measured using an oscilloscope.

5.3 Results

Here, we present the results of the experiment by first examining qualitative trends. Then, we determine the plasma parameters and evaluate the our proposed onset criterion for the plume mode near the cathode. These results are compared to the frequency and amplitude of global discharge current oscillations.

5.3.1 Qualitative Results

Figure 5.2 shows qualitatively that by manipulating the discharge current and mass flow rate, we are able to induce the spot-to-plume mode transition. For a given current, the transition is induced by lowering the flow rate to the cathode. At intermediate flow rates near the transition from spot to plume mode, the power-supply begins to interact with the discharge. This is largely unavoidable with the current experimental setup and may require additional

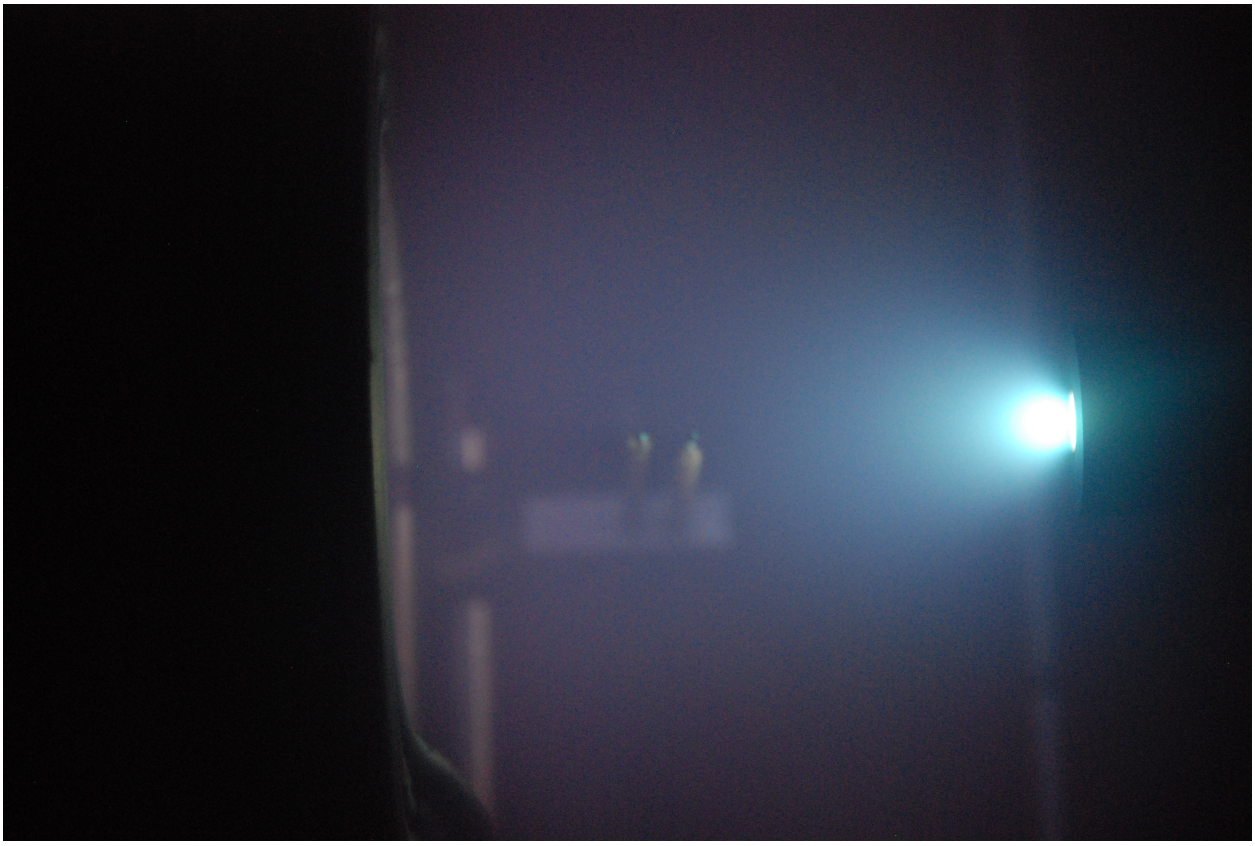

Figure 5.1: Experimental setup showing the cathode, anode, and two Langmuir probes.

filtering of the discharge using capacitors and inductors. While we are able to measure steady state plasma parameters for these conditions, they may be affected by the power-supply interaction. Below a certain flow rate (typically below 5 sccm Xe), the discharge enters a different mode, where the entire vacuum chamber is bright. We interpret this as an excited and more diffuse mode, where all the neutral gas in the chamber is excited, possibly through an interaction with the wall. This is accompanied with the same low-frequency oscillation that is associated with the plume mode, however, it has a larger amplitude and is more coherent.

5.3.2 IAT Wave Energy

Figure 5.3 shows the IAT amplitude as a function position, mass flow rate, and discharge current. The IAT amplitude has been estimated by calculating the Fourier transform of the

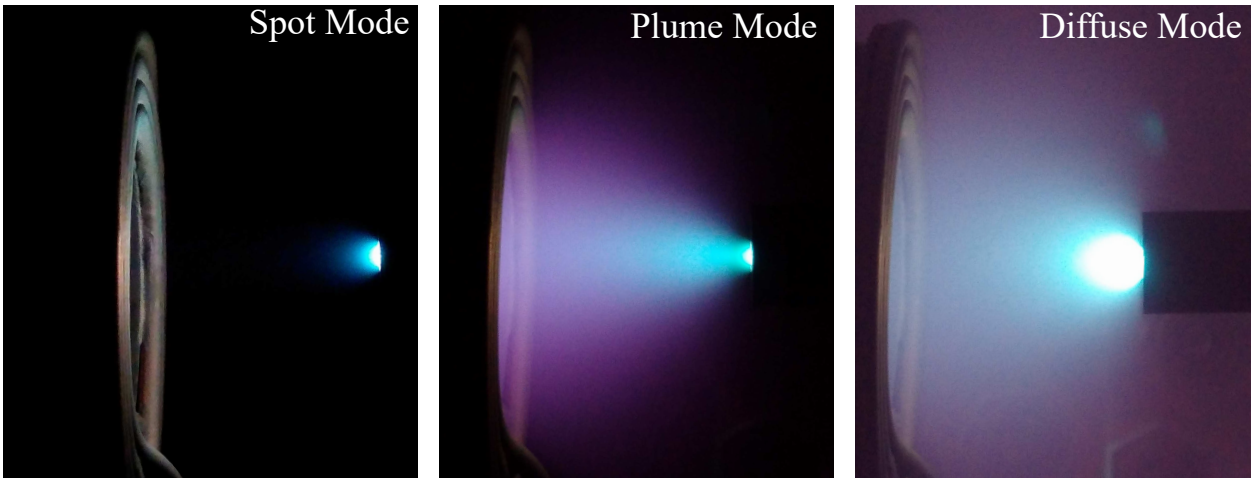

Figure 5.2: Images showing qualitatively that we have observed the transition from spot to plume mode.

ion saturation current measurement and summing over modes associated with the IAT.

$$A_{IAT} = \sum_{IAT} \left(\frac{\tilde{n}}{n_0} \right)_{\omega}^{2} , \tag{5.1}$$

where $(\tilde{n}/n_0)_\omega$ is the Fourier amplitude at frequency ω. The regions shown in red indicates the conditions where the plasma discharge was interacting with the power supply and affected the amplitude of the IAT. We have removed these points and interpolated between the edges to fill in the plot. In Fig. 5.3 there are a number of distinct trends. At fixed current, we find that this parameter tends to increase with decreasing flow rate. This is consistent with our expectation that reduced gas flow lowers the neutral density and therefore the collisional damping of the IAT. Additionally, we find the IAT amplitude tends to increase with increasing current. This is consistent with previous measurements of IAT in cathodes and is indicative of the increase in electron velocity associated with larger currents. [3] In the context of the previous results in Chapter 3, we know that this IAT will result in increased Ohmic heating of the plasma, leading to changes in temperature across the length of the plume.

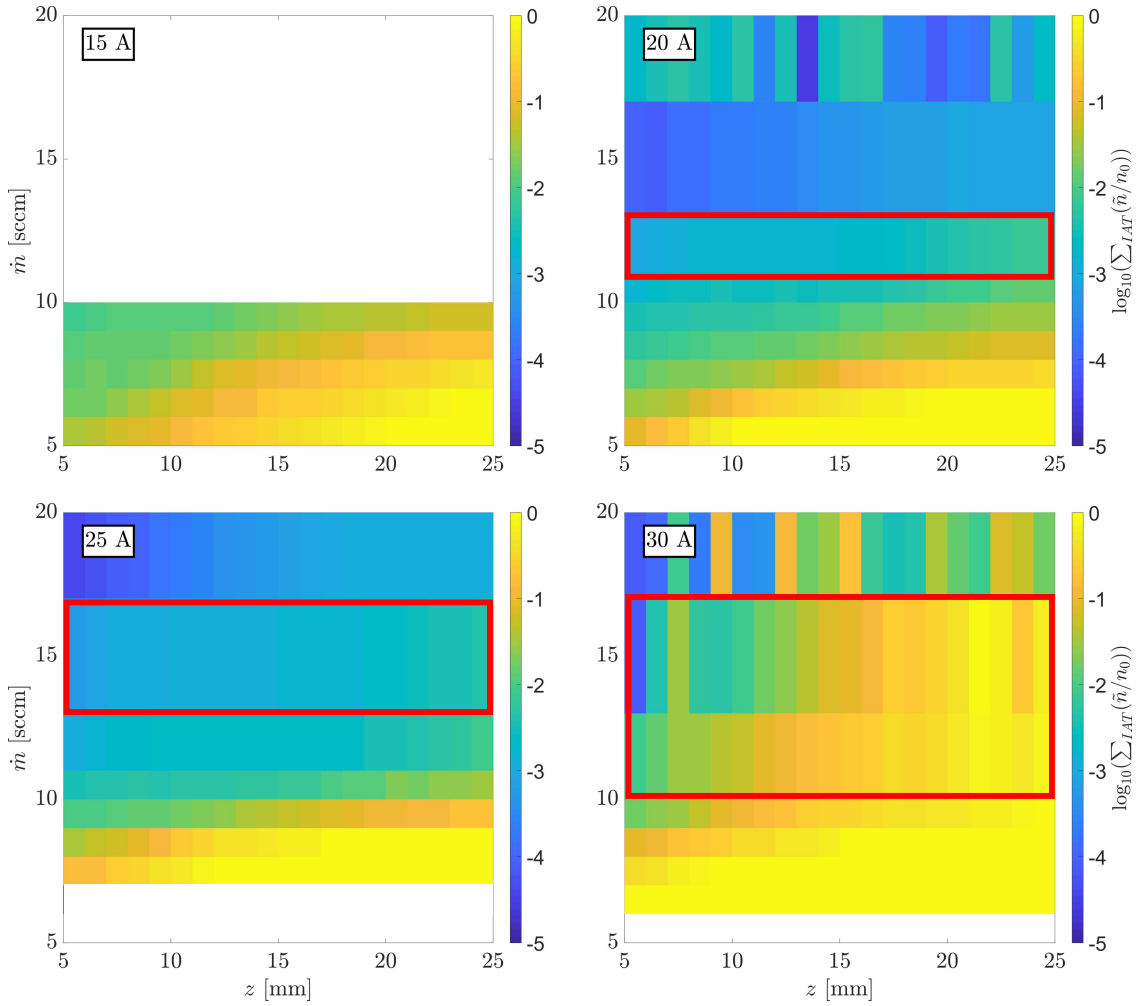

Figure 5.3: IAT amplitude as a function of position, mass flow rate, and discharge current.

5.3.3 Electron Temperature

The electron temperature is estimated using the conventional Langmuir probe (LP) theory from Ref. [89].

$$T_e = \frac{1}{\frac{\partial \ln(I - I_{sat})}{\partial V_{probe}}} , \tag{5.2}$$

where I is the probe current, I_{sat} is the ion saturation current, and V_{probe} is the probe voltage. Figure 5.4 shows an example of the Langmuir probe analysis. The data in the red region is curve fit with a first degree polynomial and the slope is used to estimate the electron

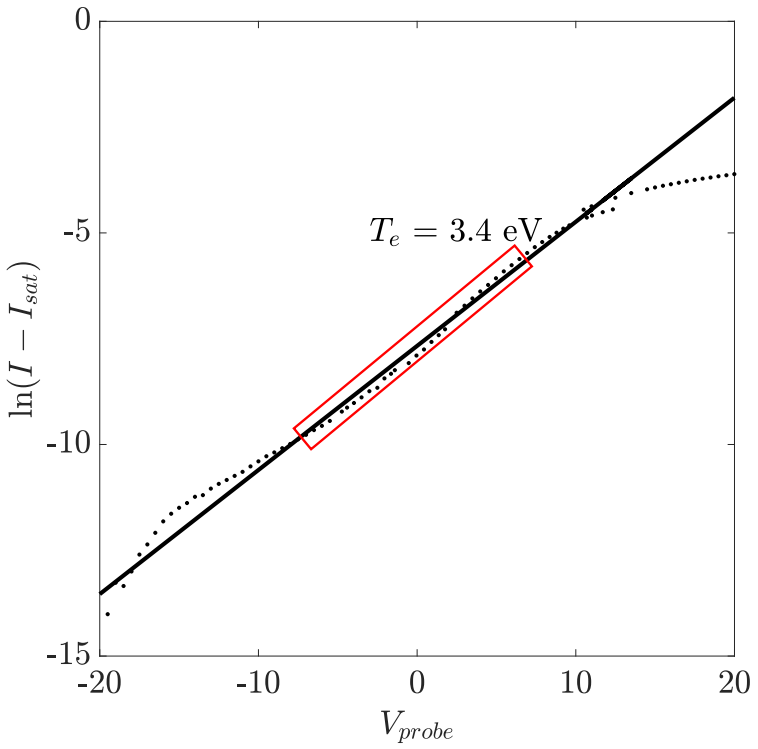

Figure 5.4: Example of the electron temperature calculation from the LP.

temperature using Eqn. 5.2.

Figure 5.5 shows the electron temperature for each of our various operating conditions. The resulting thermal energy of the electrons follows a key trend. The electron temperature tends to follow the IAT wave energy shown in Fig. 5.3. We can understand this important feature in the data using the background theory for IAT presented in Chapter 2, notably Eqn. 2.3. At lower propellant flow rate, the neutral density decreases, the collision damping of the IAT is reduced, and therefore the amplitude of the IAT rises. At higher currents the electron drift velocity tends to rise. This enhances the growth rate of the IAT and also leads to greater wave amplitude. As the IAT wave energy increases, the anomalous collision frequency rises and strengthens the Ohmic heating of electrons, which in turn amplifies the electron temperature. As such, the electron temperature should trend with the IAT wave amplitude, because non-classical, wave-driven heating is the dominant source of energy transfer as we showed in Chapter 3.

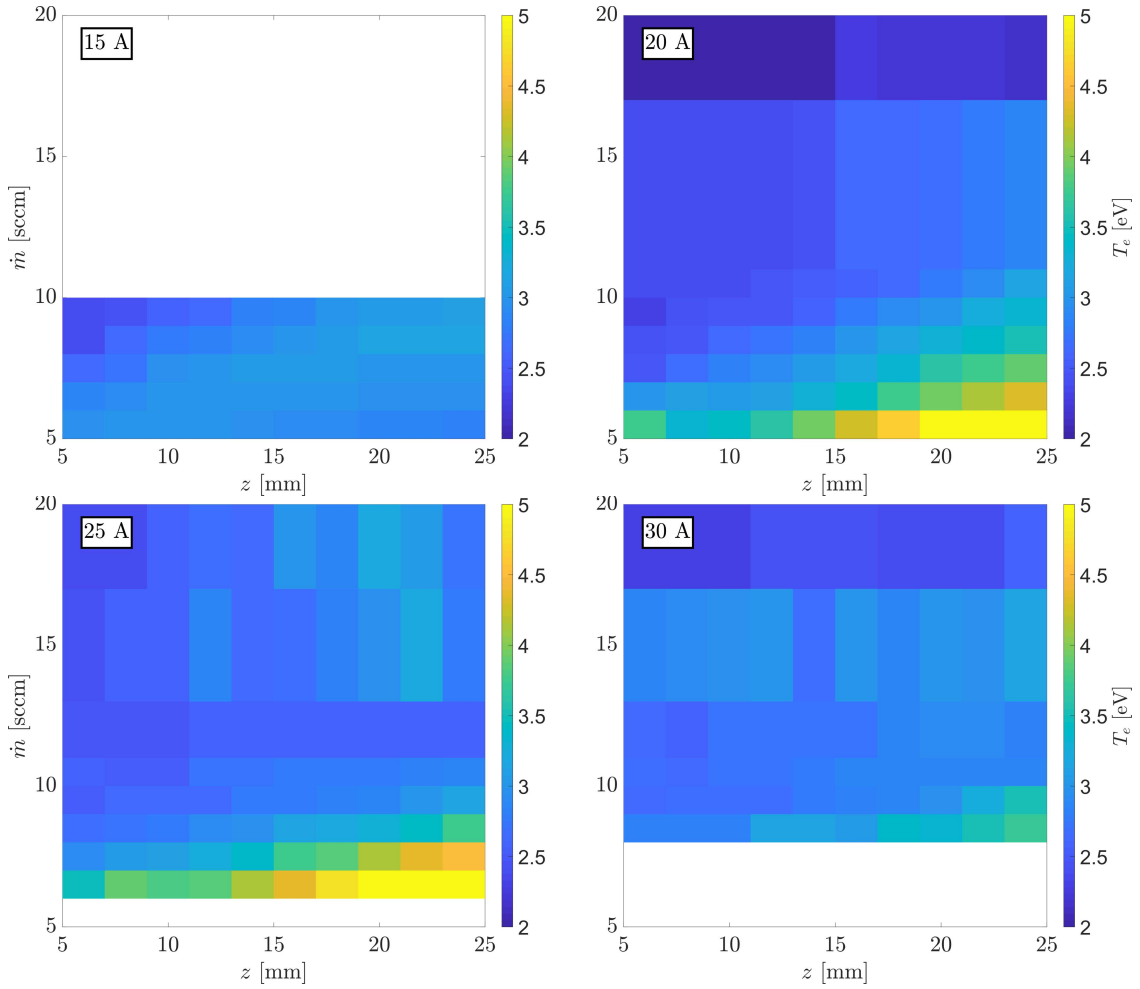

Figure 5.5: Electron temperature as a function of position, mass flow rate, and discharge current. White space are flow-rates where data was not collected.

5.3.4 Density Ratio

Having determined the electron temperature, the density is calculated using a standard thin sheath Langmuir probe analysis technique [89]

$$n = \frac{I_{sat}}{0.61 q A_p \sqrt{q T_e / m_i}} , \tag{5.3}$$

where A_p is the probe size. The results of this analysis are shown in Fig. 5.6. We find that the density drops off monotonically away from the cathode, as previously observed. We find that the density tends to rise with increasing current and flow rate.

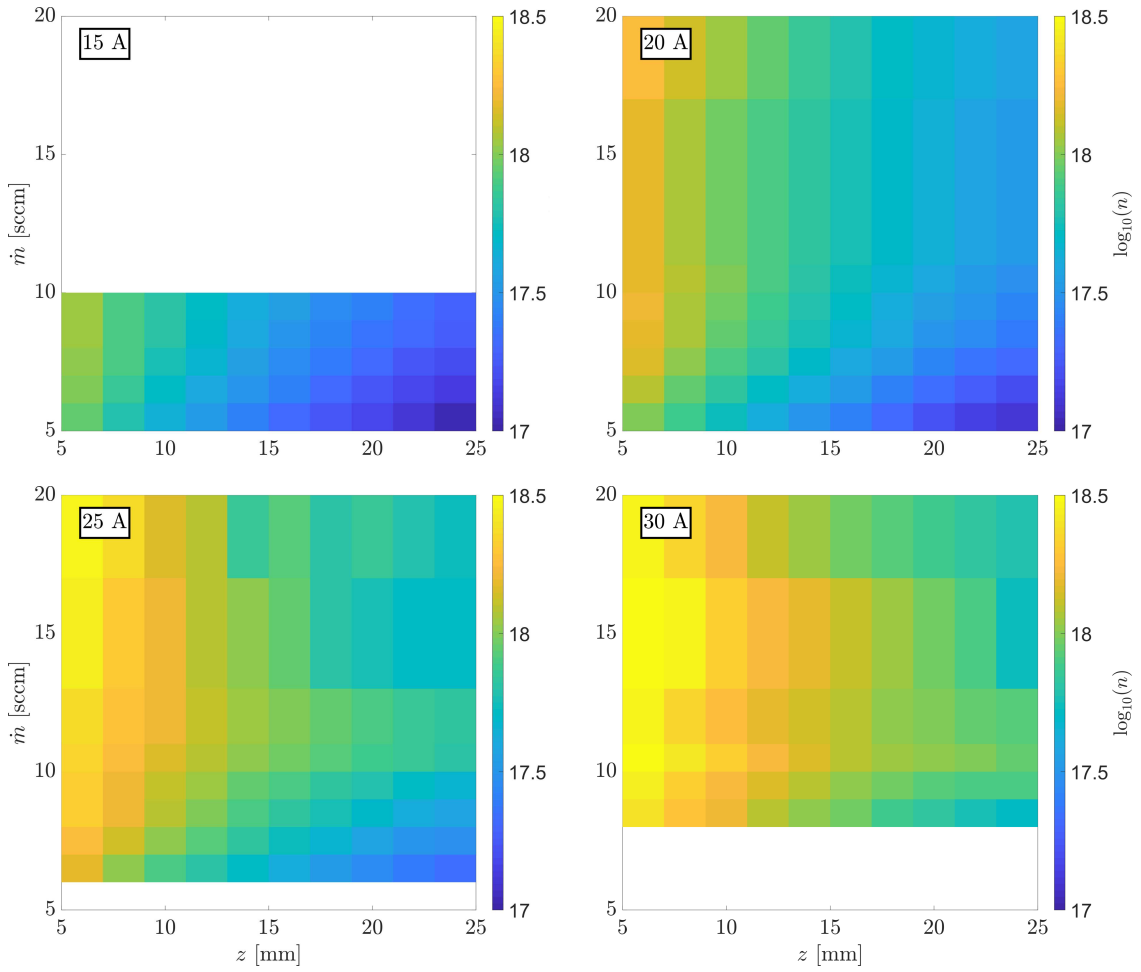

Figure 5.6: Plasma density as a function of position, mass flow rate, and discharge current.

The neutral density is determined by integrating the neutral continuity equation, assuming an expansion of the gas from the keeper orifice to the anode at a constant velocity.

$$n_n = \frac{n_{nk} A_k}{A(z)} - \frac{\int_0^z n \nu_{iz} A(z) dz}{A(z) v_n} , \tag{5.4}$$

where n_{nk} is the neutral density at the keeper orifice, A_k is the area of the keeper orifice, $A(z)$ is area of the plume at position z downstream from the cathode, and v_n is the thermal speed where we assume the neutrals are thermalized to the emitter temperature, which is on the order of 2000 K . [6] We calculate the orifice neutral density as $n_{no} = \dot{m}/(v_n A_o)$. We determine the plume area $A(z) = \pi (r_k + 0.3z)^2$, where r_k is the keeper radius and $r_A/\ell_{c-a} = 0.3$ is the

aspect ratio of the anode radius to the cathode-anode gap. [6] We justify this choice by the shape of the plume where we see that the light emission connects conically to the anode in a plume mode discharge. The result of this calculation is shown in Fig. 5.7. We find that the neutral density tends to increase with mass flow rate and is insensitive to the discharge current. Overall we find that the plasma density is 1 to 2 order of magnitude less than the neutral density.

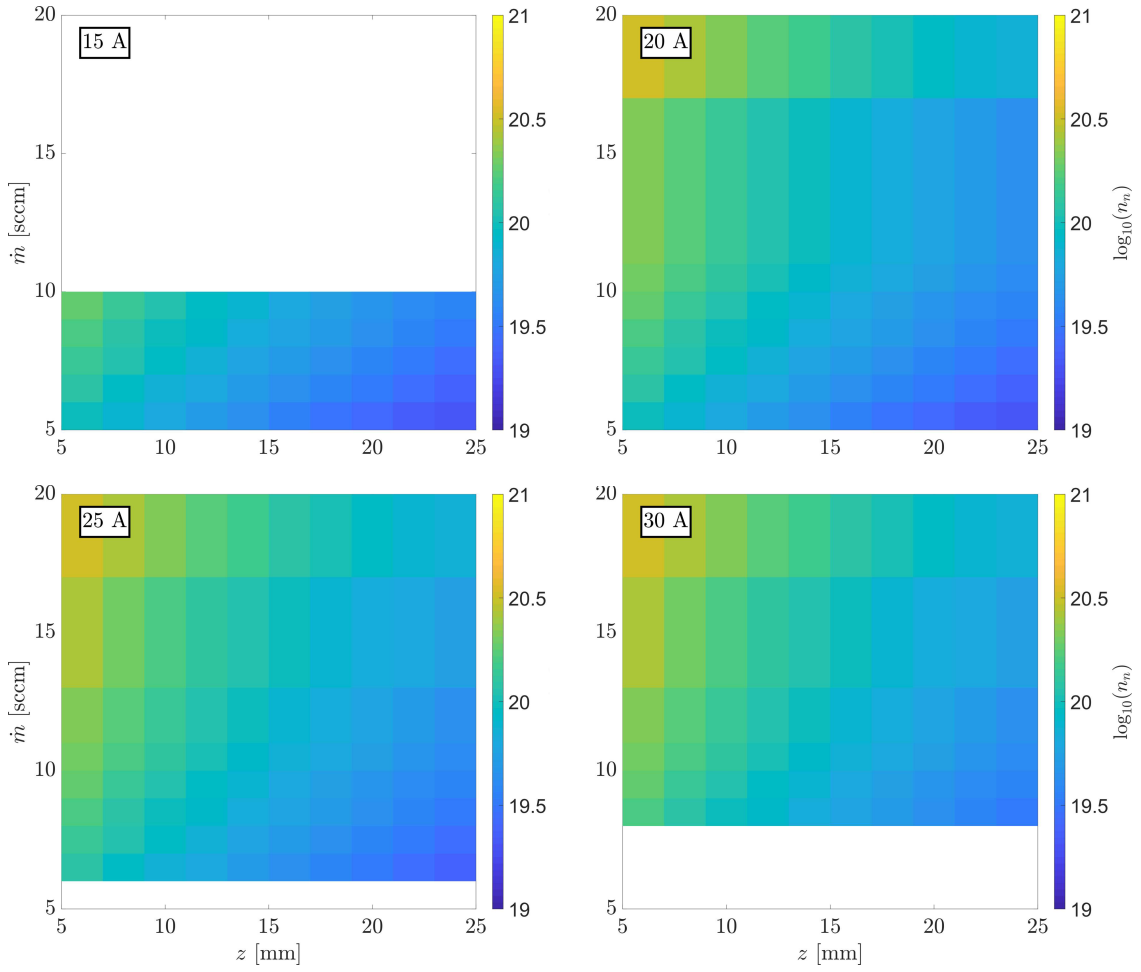

Figure 5.7: Neutral density as a function of position, mass flow rate, and discharge current.

Figure 5.8 shows the parameter $\alpha \equiv n/n_n$, which can roughly be interpreted as an ionization fraction, as a function of position and mass flow rate. We find that α tends to be between 0.1% and 2% ionized. The ionization fraction tends to rise with discharge current, distance from the cathode, and with lower flow rates. Our estimated ionization fraction is

one to two order of magnitude lower than is estimated by others. Ref. [2] claims around 40% ionization and numerical results claim ~99% ionization at certain locations. [5] This under prediction could be due to a few reasons. The first is the Langmuir probe analysis technique we have used to estimate the plasma parameters. In our analysis, we have inherently assumed that the plasma is Maxwellian, with no bulk drift velocity; however, we know that the electrons and ions are drifting quite rapidly, both possibly up to Mach ~1. Because our probe is oriented transversely to the plasma flow (the flow crosses the long side of the cylindrical probe), we collect additional current due to the drifting component which leads to uncertainty in our estimate of the temperature, collected ion current, and consequently plasma density. As a result, these probe measurements are primarily useful for finding trends in the data as a function of discharge current and mass flow rate. Comparing with numerical simulations, [5] we find that the simulated plasma density is typically a order of magnitude larger in the plume than our measurement. The second possibility is that we have over predicted the neutral density with our simple model. Under a similar comparison, we find that our estimate of the atom density can be around order of magnitude larger than anticipated by numerical simulations. Therefore, we adjust α by a factor of 10 in our evaluation of the theory. Notably, this only affects the calculation of the real frequency of oscillation, ω_r, and not than the growth rate, γ.

5.3.5 Evaluation of the Frequency and Growth Rate

Now, using the experimental results from Figs. 5.5 - 5.8 we will evaluate our onset criterion given by Eqn. 4.95 and the real component given by Eqn. 4.94. These depend on the ionization frequency and the diffusion rate. Since our model is 0 dimensional, only the source region (see Fig. 3.5) can be described. From our measurements, it appears the the plume mode wave is originating very close to the cathode. As such, we evaluate our theory at this location in the plume and compare it against global oscillatory properties like the frequency and amplitude of the discharge current fluctuations.

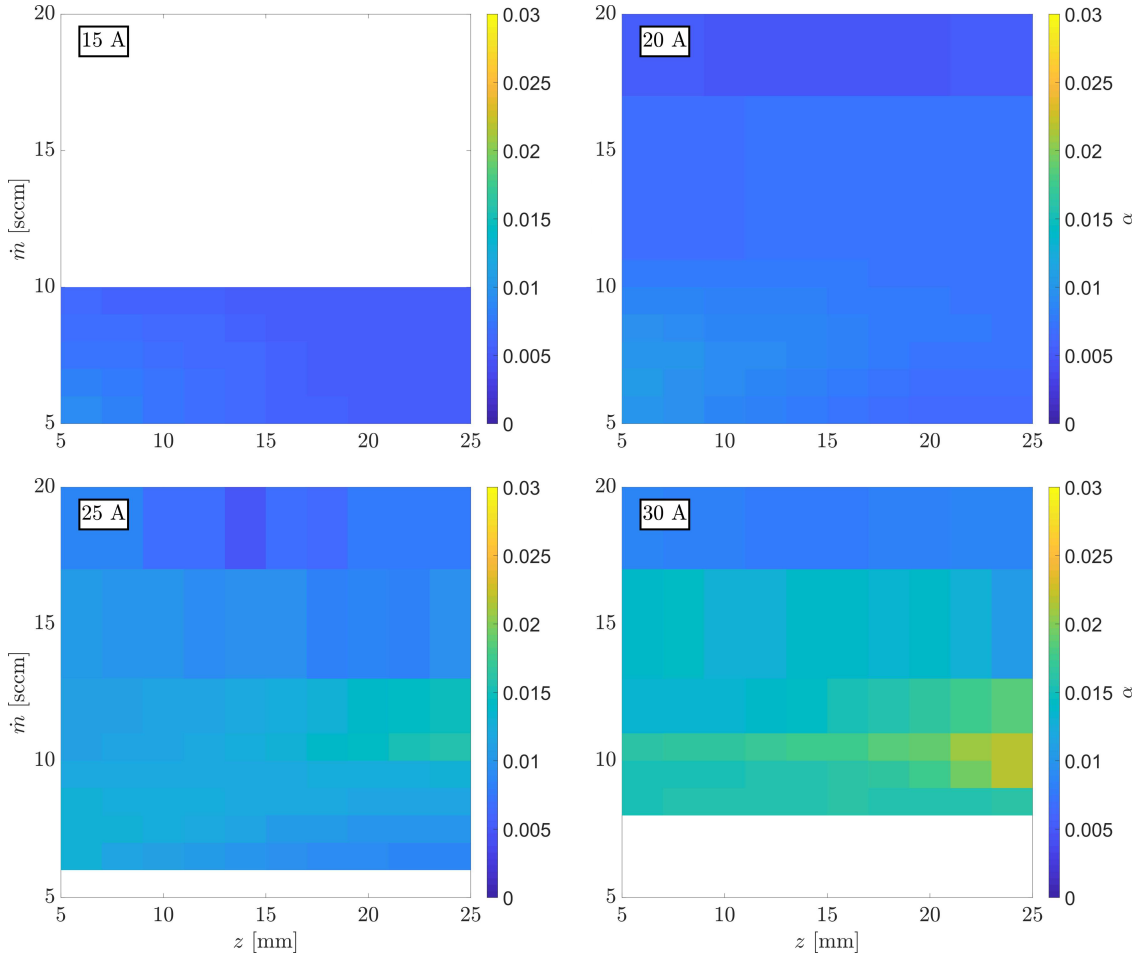

Figure 5.8: Density ratio as a function of position, mass flow rate, and discharge current.

We calculate the plume mode wave amplitude from the discharge current as

$$A_{dc,iz} = \sum_{\omega} \left(\frac{\tilde{I}_{dc}}{I_{dc,0}} \right)_{\omega} , \tag{5.5}$$

where $\tilde{I}_{dc}$ is the discharge current fluctuation around its mean value and we are summing over values of ω associated with this ionization mode (10-100 kHz). The result of this analysis is plotted in Fig. 5.9a. The arrow illustrates the overall trend in the data and the empty points are conditions that data was not captured. We find that the measured wave amplitude increases with greater current and lower flow rate. Interestingly, this is the trend we found in the electron temperature, which our analysis in Chapter 4 suggested is the critical parameter

for onset.

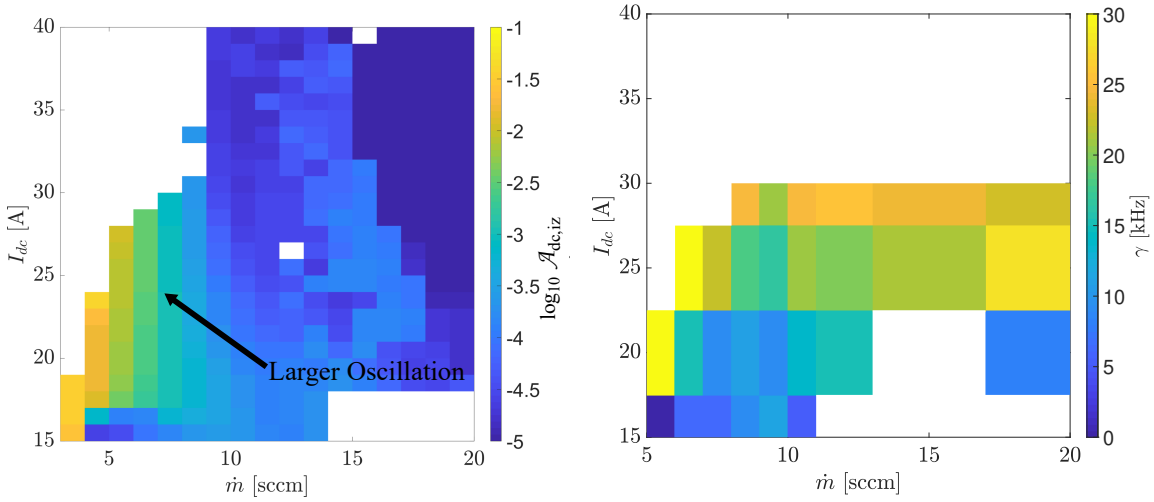

(a) Plume mode discharge current oscillation amplitude as a function of current and flow rate to the cathode. Arrow shows the trend in the data.

(b) The estimated growth rate as a function of mass flow rate for the 15, 20, 25, and 30 A.

Figure 5.9: Comparison of the measured wave amplitude and calculated growth rate.

Next, we calculate the growth rate from our theory. The ionization frequency is determined from the electron temperature (Fig 5.5) and neutral density. The diffusion rate, requires an estimate of the lengthscale, L, and ion velocity, u_i. The lengthscale, L, is calculated as $1/L = \nabla(n)/(n)$ and $u_i \sim 4$ km/s based on Refs. [3, 66]. In Fig. 5.9b, we plot the result of this calculation as a function of flow rate and discharge current. Here, we find a similar trend in the as to Fig. 5.9a, where the amplitude of the wave increases with lower flow rate and greater current. Again this is the same trend as the electron temperature. At the 15 A and 5 sccm, our theory predict that the mode is damped. This agrees with our measurement of the discharge current oscillation amplitude in Fig. 5.9a, which tends to be much lower a 15 A than the 20 A condition.

We further examine this correlation in Fig. 5.10, which shows a response plot between the oscillation amplitude and the theoretically calculated growth rate. Here, the open squares, circles, and diamonds, are the 20, 25, and 30 A conditions, respectively. We have only

plotted points where a growth rate is positive, and where the plume mode frequency could be observed in the Fourier transform of the discharge current. The two dashed lines are linear trend lines for the 20 and 25 conditions (only one point in the 30A condition). Using these data points, we quantify the overall correlation using the bivariate coefficient

$$\rho_{x,y} = \frac{\mathrm{cov}(X, Y)}{\sigma_x \sigma_y} \ , \tag{5.6}$$

where cov represents the covariance between the parameters x and y, and σ represents the standard deviation in x and y. If $\rho_{x,y} = 1$ then x and y are linearly correlated. If $\rho_{x,y} = 0$ then the two are not linearly correlated (possibly uncorrelated). Lastly, if $\rho_{x,y} = -1$ then there is negative, linear correlation between x and y. In our case, the bivariate coefficient tells us if the amplitude of the plume mode wave is positively correlated with the growth rate of the wave. In addition to the bivariate coefficient, we also calculate the p-value, which represents the likelihood of finding a correlation under the assumption that the wave amplitude and theoretical growth rate are uncorrelated. Meaning, if the p-value is small (typically, p $\sim$ 0.05 is used) then it is unlikely that our result could be produced if the two quantities were uncorrelated. Alternatively if p $\sim$ 1, then the distribution of the data could likely be produced by A_{iz} and γ being uncorrelated.

Applying this statistical analysis to our data, we find the results shown in Tab. 5.1. The results indicate that for each condition, the measured wave amplitude and the theoretical growth rate are positively correlated ($\rho_{A_{iz},\gamma} \sim 1$) and that this correlation could not likely be produced if the data were and theory were uncorrelated (p $\sim$ 0.05). When we combine the data sets, we find that $\rho_{A_{iz},\gamma} = 0.36$ and the p-value is 0.27. This indicates that overall there is indeed a positive correlation between the two, however, it is relatively weak be cause p is large (> 0.05). The weak correlation of the overall data set is perhaps not unexpected since we are not directly comparing a theoretical and measured growth rate, but rather growth rate to the amplitude. The wave amplitude could depend on the mechanism behind the

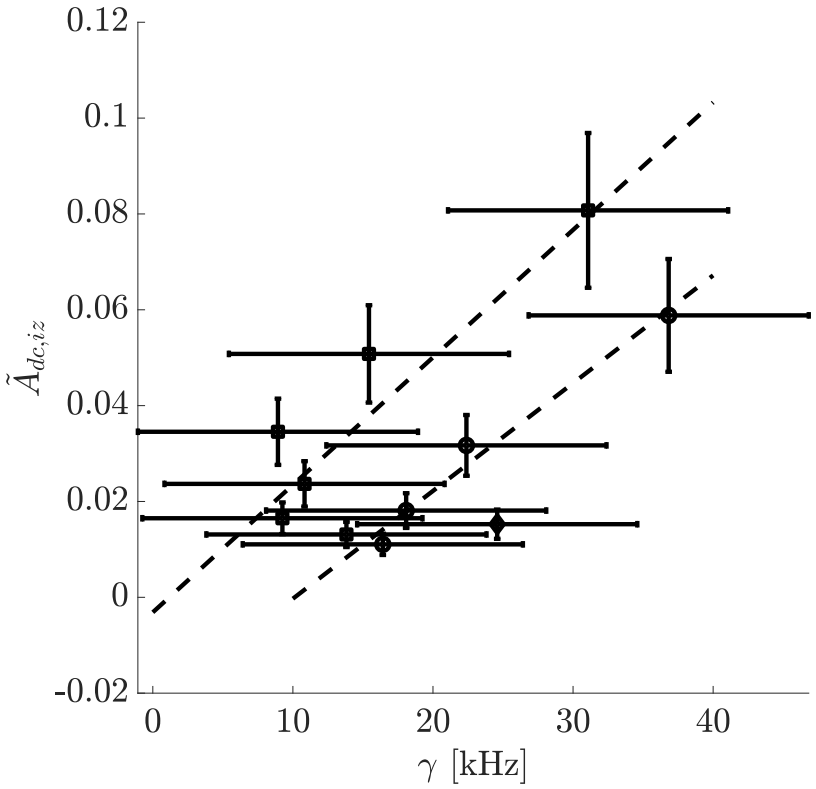

Figure 5.10: Response plot of the discharge current wave amplitude to the predicted growth rate. Dashed lines show trends for the 20 A condition (squares) and the 25 A condition (circles). We also have one point a the 30 A condition (diamond).

saturation of the wave. This non-linear effect may depend on the discharge parameters and it is not taken into account by our analysis. This statistical analysis supports our conclusion through correlation that the growth of the plume mode wave (captured experimentally by an increase in amplitude) can be described by our theory proposed in Chapter 4 where a predator-prey ionization oscillation is destabilized by temperature fluctuations driven by presence of enhanced Ohmic heating of electron due to IAT.

Now we turn our analysis to the real frequency of oscillation. In Fig. 5.11a, we show the measured plume mode oscillation frequency, f, of the discharge current as a function DC discharge current and mass flow rate. This is determined by calculating the Fourier transform of the discharge current signal and algorithmically searching for peaks in the typical plume mode range. In this figure, frequencies below 40 kHz indicate that no clear peak could be

Table 5.1: Bivariate coefficient and p-values comparing the theoretical growth rate with the wave amplitude. This shows that our model is highly correlated to the individual data sets, but weakly correlated to the combined data set.

Data Set	$\rho_{A_{iz},\gamma}$	p-value
20 A	0.679	0.138
25 A	0.99	0.014
20 A + 25 A	0.36	0.27

found by our algorithm for that condition. Here, we find similar trends where the frequency of oscillation tends to grow with greater discharge current and lower frequency, the same trend as the electron temperature. Overall, f tends to be between 50 kHz and 70 kHz. This is in the same frequency range as our earlier measurements (see Fig. 3.14) and the previous observations of others. [2]

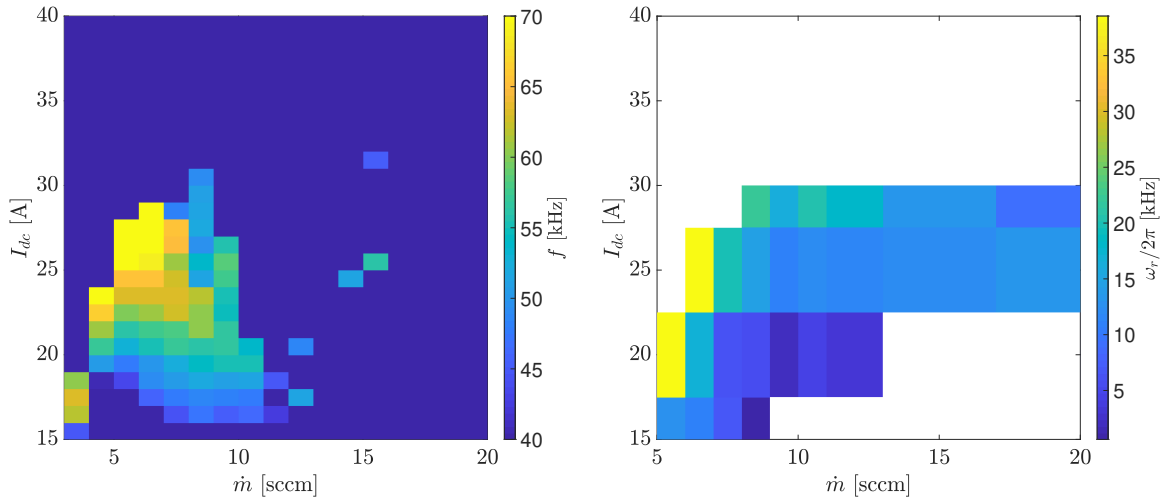

(a) Measured frequency of oscillation in the discharge current as a function of mass flow rate and discharge current.

(b) Real frequency of oscillation determined using Eqn. 4.94 as a function of flow rate and discharge current and measured discharge current oscillation frequency.

Figure 5.11: Measured frequency and predicted frequency.

Figure 5.11b shows the theoretical frequency, $\omega_r/2\pi$ as a function of those same discharge parameters. The blank spaces in the plot are points where there is either no data, or a real frequency could not be calculated based on the theory. Examining this figure, we find a similar trend where the frequency tends to increase at lower flow rates and higher current.

Again, this is notably the same trend as the electron temperature. We compare the measured and theoretical frequency in the response plot showed in Fig. 5.12. In this figure, the dashed line represent the line of perfect correlation and the dotted-dashed line shows the overall trend in the data. We find that the data points are all on the left hand side of the line of perfect correlation, meaning we have underestimated the oscillation frequency by around a factor of between 2 and 10. There are a few possible reasons for this. First is that the ionization fraction is even higher than our corrected estimate. Second is that we have only considered the electron thermal energy as being responsible for ionization; however, in this plasma the kinetic energy of the electrons can be on the same order as the thermal energy (see Fig. 3.13b). Therefore it is possible that we generally have underestimated the ionization rate by not taking this additional energy into account. We find that the lowest flow rate conditions tend to have the best quantitative agreement, which are the conditions where the plume mode is most apparent in the experimental data. The overall trend line has a small positive slope suggesting a positive, but weak, correlation between the total data set and our theory.

We examine the correlation more closely with the bivariate coefficients and p-values shown in Tab. 5.2. First looking at the 20 A data, we actually find negative correlation between the measured frequency and the theory. Upon examining the measured frequencies in Fig. 5.11a, we see that specifically for this condition the frequency does not vary strongly with mass flow rate while the theoretical frequency tends to increase as shown by Fig. 5.11b. This causes the negative correlation. At the 25 A setting, however, we find that our prediction with the model is positively correlated with the measured frequency. This suggests that our model is capturing the trends for the 25 A condition. Examining the complete data set, we find that the frequency is overall positively correlated although the correlation is weak, given the p-value of 0.4. It is unclear why we find conflicting correlations between the 20 and 25 A conditions. It is possible that at this lower current some of the assumptions of the theory are not valid. For example, when the temperature is low (like in the lower

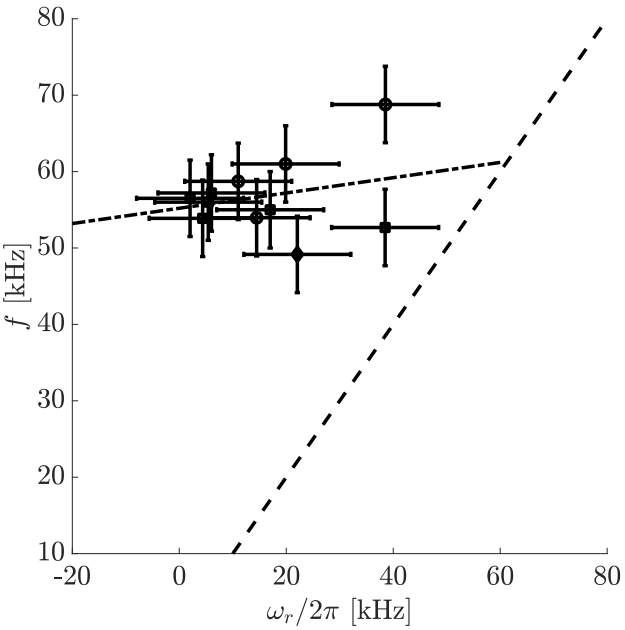

Figure 5.12: Response plot of the measured frequency vs the calculated frequency, showing overall positive correlation. The dashed line indicates perfect correlation and the dotted-dashed line shows is the linear trend in the data. Plotted are the 20 A condition (squares), 25 A condition (circles), and 30 A condition (diamond).

current conditions) the ion inertia may dominate over diffusion and could lead to a change in the theoretical expression for the oscillation frequency. If the mechanism for onset is still: ionization > losses, then we could still expect to find positive correlation to the growth rate shown Tab. 5.1 for the 20 A condition.

Table 5.2: Bivariate coefficient and p-values comparing the theoretical growth rate with the wave amplitude.

Data Set	$\rho_{A_{iz},\gamma}$	p-value
20 A	-0.7	0.1
25 A	0.9	0.1
20 A + 25 A	0.3	0.4

Overall, we have evaluated the growth rate and frequency of the plume mode wave using our model and experimental measurements. We compared this calculation to the amplitude and frequency of the measured plume mode wave. For the 20 A condition, the result was mixed where the growth rate and amplitude were positively correlated while the

frequencies were negatively correlated. It is possible that some of our assumptions are broken at lower currents, leading to the discrepancy. On the other hand, we find that the theory and experiment are highly correlated for the 25 A setting. Given the success of the theory for the 25 A condition and the overall positive correlation, the theoretical model we have developed is able to reasonably describe the experimentally observed trends.

5.4 Discussion

Here we have shown that with increasing current and lower mass flow rate, the hollow cathode plume increases in temperature and ionization fraction (density ratio) as shown by Figs. 5.5 and 5.8. From our enhanced predator-prey model, we expect that the frequency of oscillation should increase with higher neutral density and higher electron temperatures, based on the definitions of α, β, $\nu_{iz,0}$, ν_{D0}, and ν_{tm}. Because the ionization rate depends exponentially on electron temperature, we found that the frequency increases with lower flow rate in Fig 5.11, in agreement with the measurement. Furthermore, we found that when we evaluate the onset criterion in Eqn. 4.95 locally near the cathode, the plasma should be unstable and that the theory predicts the trends in discharge current and mass flow rate.

Next, we analyze our results in the context of global plasma parameters. The empirical onset criterion says $I/\dot{m} > C$, therefore we expect that the discharge current amplitude should be highly correlated with $I/\dot{m}$. In Fig. 5.13, we show a response plot between $I/\dot{m}$ and A_{iz}. Here we find that there appear to be three regions of this plot, which are highlighted by the red, green, and blue lines. In the red region, we find positive correlation between the ionization wave amplitude and the classical onset criterion. These are the conditions in the bottom-left hand side of Fig. 5.9a. In the green region, the wave amplitude is almost uncorrelated with the $I/\dot{m}$, corresponding to the conditions between 10 to 15 sccm and 25 to 40 A in Fig. 5.9a. Lastly, the blue line shows conditions that are negatively correlated. These lie on the right-hand side of Fig. 5.9a, above 15 sccm. Overall, this result tells us that

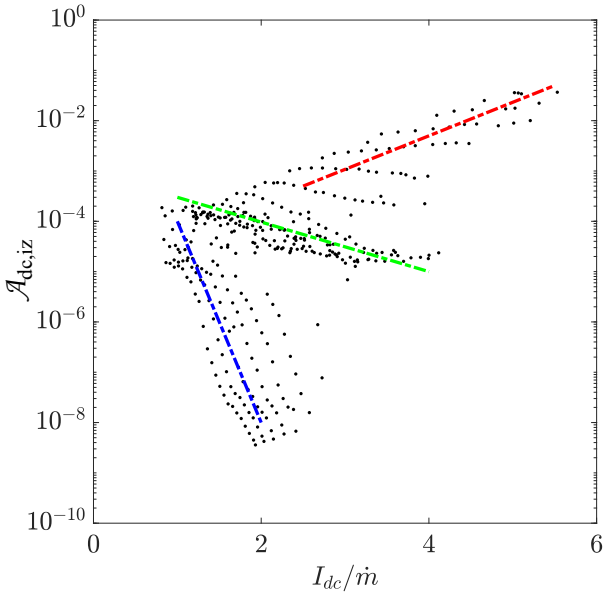

Figure 5.13: Ionization wave discharge current amplitude vs. classical onset criterion $I/\dot{m}$. Blue line shows data points where the wave amplitude is negatively correlated with $I/\dot{m}$. The green line identifies points where the discharge current amplitude is weakly correlated with $I/\dot{m}$. The red line identifies points where the discharge current amplitude is positively correlated with $I/\dot{m}$.

although many sources suggest $I/\dot{m}$ is related to onset, it is in fact not always good predictor of the ionization wave amplitude. By this we mean that increasing $I/\dot{m}$ does not always lead to a increase of the plume mode wave amplitude.

Alternatively, we have shown from our first principles theory that the onset should be related a critical electron temperature that varies weakly with mass flow rate. To illustrate this point, we plot in Fig. 5.14 the ratio of the electron temperature to T_e^{crit}, which was calculated using Eqn. 4.100. The trend in the data follows that of the growth rate in Fig. 5.9b, suggesting that a critical electron temperature is indeed a good predictor of the wave growth. Furthermore, the ratio is always greater than 1, meaning that all these conditions should exhibit the ionization wave, which largely agrees with our full theoretical estimate of the growth rate. This connection means that the concept of a characteristic onset temperature can be used to as a simplified method to evaluate wave growth.

We showed with Eqn. 4.114 that this critical electron temperature can be rewritten as

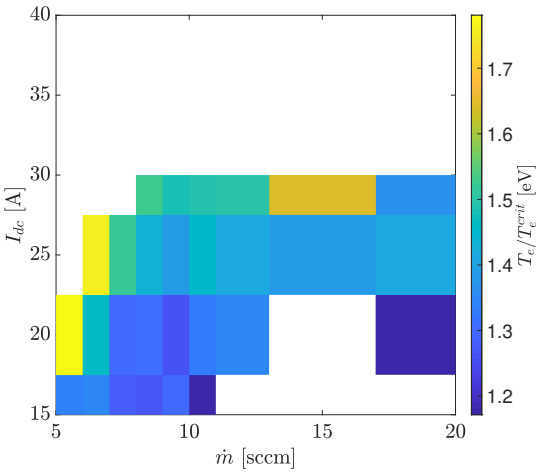

Figure 5.14: Ratio of the electron temperature to the critical electron temperature for the onset of plume mode using Eqn. 4.104.

a discharge voltage. If V_{dc} exceeds this value, then the plume mode is thought to onset. When evaluating Eqn. 4.114, we take an average of the first three points in the plume, since this tends to be the region where the plasma potential changes in the most (see Fig. 3.13a). Figure 5.15a shows a histogram of the critical discharge voltage determined from these points and indicates that it typically lies between 12 V and 18 V. Now plotting our measured wave amplitude in terms of the discharge voltage in Fig. 5.15b, we find that a few distinct trends in the data emerge. At very low voltage, the discharge current oscillation is very small compared to the DC value (10^0 on the plot) but rises with voltage. In this region there appears to be a one-to-one bijection between the two parameters. At intermediate voltages, between 12 and 18 V, there appears to be a transition region where the discharge voltage does not consistently predict the discharge current oscillation in this frequency band, meaning a given discharge voltage could imply several wave amplitudes. However, at voltages above 20 V, we find that the ionization wave amplitude large and highly correlated with the discharge current. This transition coincides with our estimate of the critical discharge voltage in Fig. 5.15a. Overall, the mode transition from spot mode (<15 V) and plume mode (>20 V) is distinctly shown by Fig. 5.15b. Although there are still some challenges in predicting the spatial properties of the wave (see Fig. 5.11 and 5.9b), a remarkable success of our 0 dimensional

model is the identification of the electron temperature and therefore the discharge voltage as the key parameters for the onset of the wave and predicting its growth and amplitude. Interestingly, the onset voltage appears to be independent of the mass flow rate and current (always around 15 - 20 V). Our earlier analysis of the onset criterion suggested that the onset voltage should depend on the neutral density and therefore mass flow rate (see Fig. 4.7). However, we concluded that if the mode onsets near the cathode, where the neutral density is high, then this dependence on the atom number density is relatively weak. This agrees with our experimental finding in Fig. 5.15b. This new insight of a relatively invariant onset voltage could ultimately prove useful for identifying the plume mode in long-duration ground testing of cathodes.

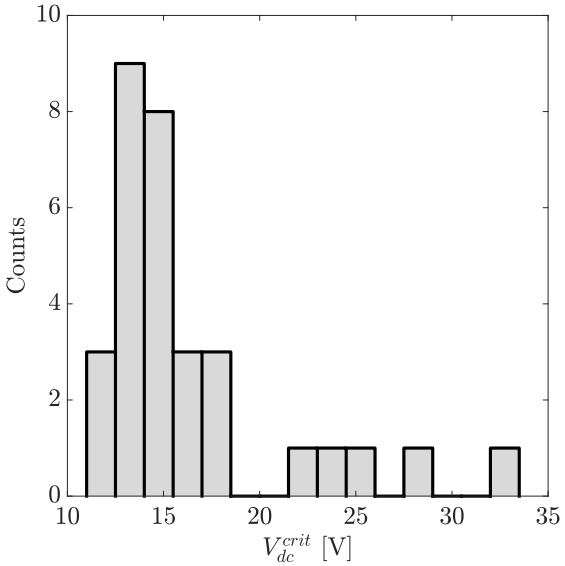

(a) Histogram of the theoretical critical voltage determined from Eqn.4.114.

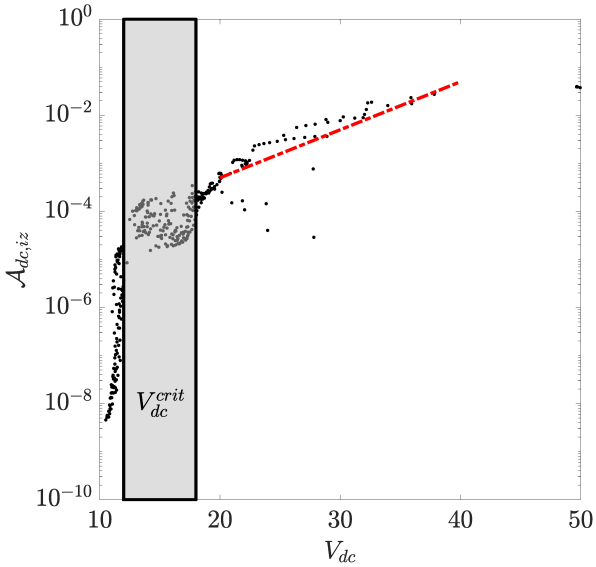

(b) Ionization wave amplitude vs. measured discharge voltage. The gray region indicates the full-width-half-max of the distribution in Fig.5.15a.

Figure 5.15: Critical onset voltage.

5.5 Conclusions

We have conducted an experiment using Langmuir probes to evaluate our theoretical model for the plume mode oscillation by sweeping the current and flow rate to the cathode. In controlling these parameters, we observed the transition from spot to plume mode. We found that the IAT and electron temperature tend to rise with lower flow rate and higher discharge current, which is consistent with the accepted theory that wave-driven collisions are responsible for the enhanced Ohmic heating of electrons in the plume. Furthermore, we show that the ionization fraction tends to increase with discharge current and is relatively insensitive to the mass flow rate. As we increase the current and lower the flow rate, we showed that the amplitude of the plume mode instability generally rises, in agreement with the work of others. When evaluating our theory, we find that although the predicted real frequency follows similar trends to the data, the magnitude is low by around a factor of 2 to 10. The theory may under-predict the frequency because we have not accounted for the role of the electron kinetic energy in ionization, which our experiments indicate is likely on the order of the temperature (see Fig. 3.13b). Overall, we found mixed results when comparing trends in our model to the measured frequency at specific operating conditions.

We also conducted a similar analysis of the theoretical growth rate and compared it to the discharge current oscillation amplitude. Both the experiment and the theory show a similar trend where the magnitude increases as a function of discharge current and lower mass flow rate. This is the same trend as the electron temperature, which our theory predicted is the critical parameter for onset. We examined the correlation statistically, and found that the data is highly correlated with the theory when comparing individual current conditions. This find indicates that our predator-prey theory is able to capture the trends for the onset of the plume mode ionization wave. Further analysis also experimentally corroborated the new theoretical insight that the discharge voltage, not $I/\dot{m}$ is the best predictor for the onset of plume mode. The discovery that this critical voltage is relatively invariant with discharge current and mass flow rate may help identify plume mode in long duration ground tends.

CHAPTER 6

Influence of the Magnetic Field on Stability

6.1 Introduction

In this last Chapter, we aim to better understand the behavior of the plume mode instability in the context of a Hall thruster plasma discharge. In a state-of-the-art Hall thruster, the hollow cathode is centrally mounted and is subject to a roughly axial magnetic field. The presence of the magnetic field is known to form coherent rotating structures in the cathode plume of the thruster that have been described as anti-drift waves. [90] On the other hand, axisymmetric numerical simulations (which for cannot capture the rotating modes) propose that the plume mode wave may continue to exist in the presence of a magnetic field and continues to drive the production of high-energy ions, rather than the rotating modes. [5] This conclusion is supported by the strong correlation between the simulation and experiment show by plume margin curve shown in Fig. 2.8. Together, these earlier findings raise a few questions. Are the plume mode wave and the rotating instabilities we observe in Hall thrusters the same? If not, do they coexist? Do we expect to find plume mode waves in a Hall thruster? Our goal for this Chapter is to conduct a preliminary experimental investigation of these questions regarding the large-scale plasma instabilities that exist in cathode discharges.

From our experimental and theoretical work in Chapters 3 - 5, we know that enhanced heating of the electrons and temperature fluctuations are necessary for the onset of the plume mode. Further, we know that IAT in the cathode plume can provide the means for the wave to

go unstable. Previous experiments show that IAT is able to propagate in the cathode plume possibly leading to the heating necessary for the onset of the ionization wave. [91, 92] The plume mode, however, has never been directly observed in a Hall thruster, but that may be because the plume mode is typically avoided for propulsion applications. In fact, it is unclear whether the presence of a magnetic field in the cathode plume could allow for the conditions necessary for the plume mode to onset. To this end, we conduct two experiments. First a qualitative, path-finding experiment using a high-speed camera. Second we investigate the wave propagation quantitatively using cross-correlated ion saturation probes. We analyze the results in the context of our plume mode theory and existing theory for anti-drift waves in cathodes.

6.2 Theory

6.2.1 Plume Mode Instability Theory

From Chapter 4, we have previously shown that the ionization instability associated with the plume mode has an onset criterion given by Eqn. 4.95 Physically, this mode onsets when particle production due to temperature fluctuations exceeds the losses to diffusion and damping by the atom influx to the plume. This physical picture and instability criterion has been shown to largely explain the growth of the plume mode oscillation. The real frequency is given by Eqn. 4.94 and is typically on the order of 10-100 kHz. This solution is found in a 0 dimensional frame-work and proposed to be convected axially by the ion drift velocity. We therefore also refer to this instability as a longitudinal ionization mode in the cathode plume.

6.2.2 Anti-drift instability

The anti-drift instability is a rotating plasma wave that is excited by the energy held in a density gradient, transverse to the magnetic field in the presence of electron collisions. The

key plasma properties of the cathode plume that enable the growth of this mode are 1) that $\Omega_i < \nu_e < \Omega_e$, where $\Omega_{e,i}$ are the cyclotron frequencies of the electrons and ions, respectively; 2) the ions are cold, i.e. $T_e \gg T_i$; 3) the wave frequency is $\nu_i < \omega < \nu_e$, where $\nu_{e,i}$ are the electron and ion collision frequencies; 4) the phase velocity of in the longitudinal direction is much greater than the sound speed ($\omega/k_z \gg c_s$). Following the work in Ref. [93], the dispersion relation for these modes in a Cartesian framework is given by

$$0 = -\frac{k_x v^* + i\nu_{pl}}{\omega - k_x v_{E\times B} - k_z u_{e,z} + i\nu_{pl}} + \frac{T_e}{m_i}\left(\frac{k}{\omega - \vec{k}\cdot\vec{u}_i}\right)^2 , \tag{6.1}$$

where k_x is the azimuthal wavevector, $v^* = T_e/B_0\nabla(n_e)/n_e$ is the diamagnetic drift, $\nu_{pl} = k_z^2 q T_e/m_e/\nu_e$. Here, we note that the expression in Eqn. 6.1 we have neglected magnetic gradient driven drifts (in comparison with Ref. [94]) and that $k_x = m/R$, where $m = 0, 1, 2, ...$ is the azimuthal mode number and R is the radius. This type of instability has been shown to exist in the partially magnetized hollow cathode plumes of Hall thrusters and should be present during standalone testing of a magnetic field. [90]

6.3 Experimental Methods

Experimentally, we are examining the claim from Ref. [5] that the rotating instability that forms in the presence of a magnetic field might coexist with the ionization instability associated with the plume mode. To shed some light on this topic, we have designed two experiments. First we operated a cathode at 20 A with a 10 sccm and 31 sccm flow rate. We varied the magnetic field strength by changing the current to a solenoid mounted around the anode and used a high-speed camera to qualitatively determine the behavior of any coherent modes that may arise in the plasma.

In our second experiment we operate the cathode in spot mode, where the ionization wave does not dominate, and in plume mode, where the ionization instability is present. Then we imposed an axial magnetic field with a solenoid and varied its strength. In practice,

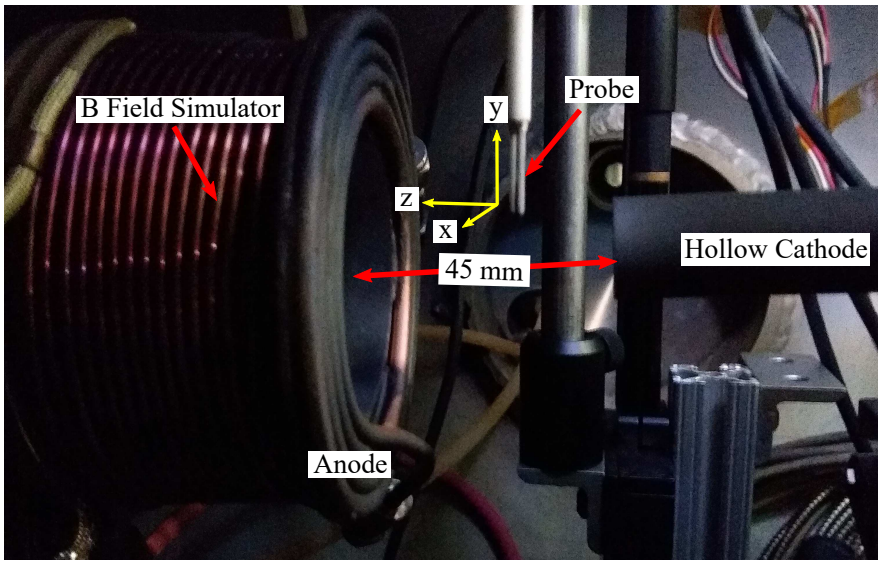

Figure 6.1: Experimental setup showing the cathode, anode, wave probe, and $\boldsymbol{B}$ field simulator.

we used a LaB_6 hollow cathode that was operated on xenon at 35 A of discharge current with 12 and 5.5 sccm. The respective discharge voltage of each condition was 12.6 and 31 V. When the magnetic field is applied, the discharge voltage of both conditions rises to 25.4 V for the high flow and 40 V for the low flow conditions. The anode was positioned 45 mm downstream of the keeper exit. The anode is wrapped with a solenoid to apply an approximately axial magnetic field to the cathode plasma. The current to the solenoid was varied from 0 to 10 A. The maximum magnetic field, $\boldsymbol{B}_0$, produced is on the order of half of the field generated in the cathode region by a state-of-the-art Hall thruster. The discharge was established in a 0.5 m $\times$ 1 m vacuum chamber that is cryogenically pumped and achieved a base pressure of 0.12 μTorr. At our selected operating conditions, the pressure was 50 and 27 μTorr. We made our measurements of plasma waves using a wave probe, biased at -54 V to collect the ion saturation current fluctuation at 20 MHz with an oscilloscope. The axis convention is shown in green on Fig. 6.1, where x, y, and z are the azimuthal, radial, and axial directions, respectively. The probe was positioned at a fixed location, 7 mm radially and 20 mm downstream of the keeper exit. The experimental configuration is shown in Fig. 6.1.

6.4 Experimental Results

In this section, we present our experimental results for the high (spot mode) and low (plume mode) flow rate conditions with variable magnetic field. For our first experiment we qualitatively examine high-speed camera images. Then with our more quantitative second experiment, first we examine the spot mode condition, primarily focusing on the presence of coherent, rotating structures that form when a magnetic field is applied using probes. Then we discuss the plume mode condition, where the ionization instability is apparent.

6.4.1 High-speed Camera

First we discuss the results of the high-speed camera. Fig. 6.2 shows high-speed images captured at 700 kfps, where the camera was place end-on, looking through the anode. In Fig. 6.2 (a) the cathode is in plume mode, and we can see the characteristic $m = 0$ global mode of the cathode oscillating at around 50 kHz. In Fig. 6.2 (b), we applied an axial magnetic field with the solenoid ($B = 1.5B_0$) and we find that rotating modes start to appear. These modes have $m \geq 1$ and are propagating azimuthally around the discharge axis. Notably, we find that by applying the magnetic field the $m = 0$ disappears from the images. This result is in agreement with previous results which showed that by applying a magnetic field, the plume mode oscillation appears to damp. [2] Our result, here, corroborates this finding and suggests that the plume mode instability is damped when a magnetic field is imposed and that rotating modes grow in its place. Fig. 6.2 (c) shows that when we increase the flow rate the cathode under the same magnetic field condition, the waves are generally damped out. Notably, this is the same trends as the plume mode instability, making it possible to confuse the two when examining global discharge parameters. Although it may be difficult to see, there is still a rotating mode in Fig. 6.2 (c), however it is very dim compared to the cathode itself in contrast to Figs. 6.2 (a) and (b).

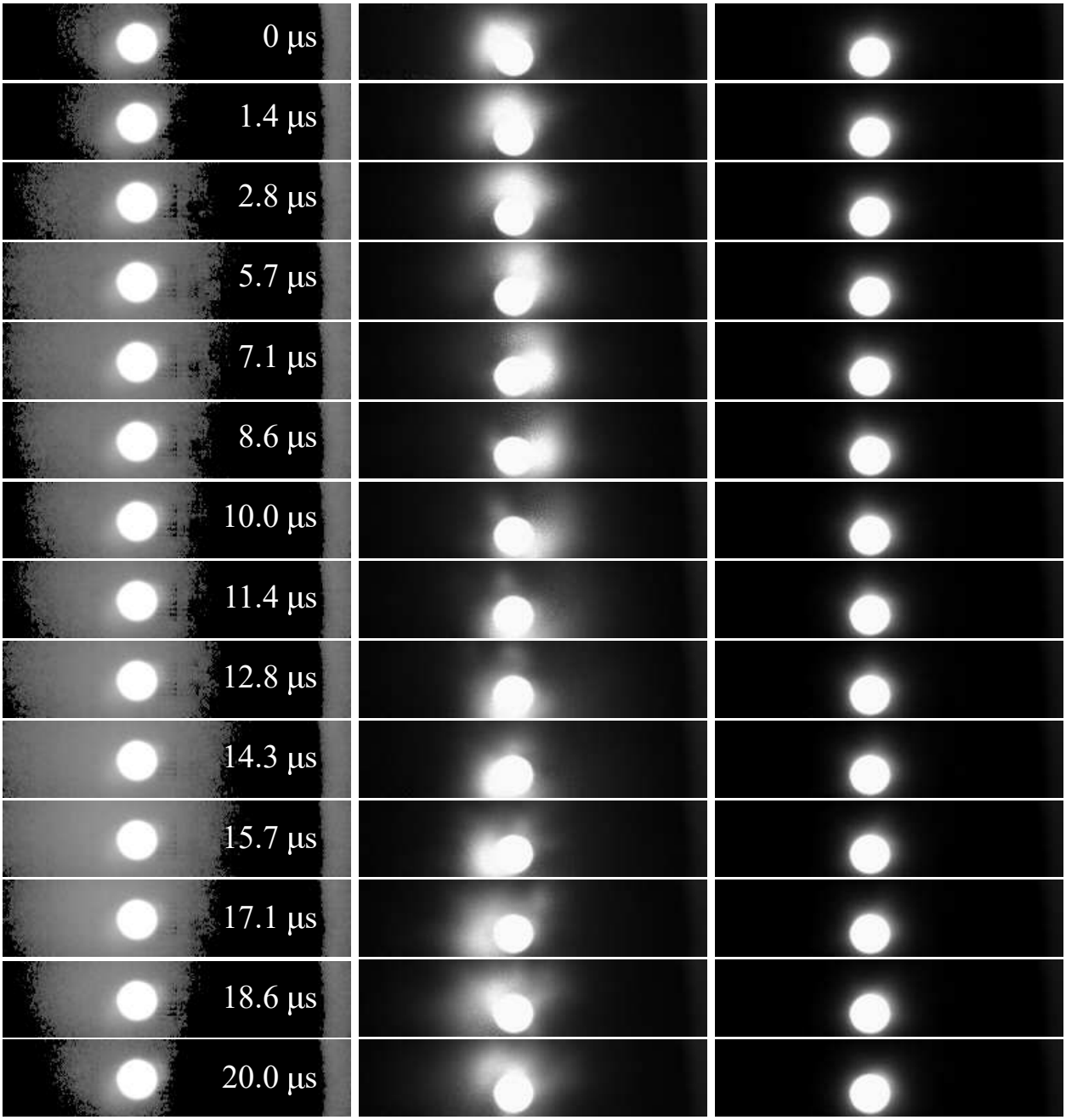

Figure 6.2: High speed images of the hollow cathode. (a) 20 A, 10 sccm, $B = 0$, (b) 20 A, 10 sccm, $B = 1.5B_0$, (c) 20 A, 31 sccm, $B = 1.5B_0$.

6.4.2 Spot Mode

In this section we will focus the behavior of plasma oscillations in spot mode with increasing magnetic field. In Fig. 6.3a, we show the logarithm of the amplitude of each mode in the plasma as a function of magnetic field strength. This figure shows that at low magnetic field, there are no low-frequency oscillations. With greater B, the entire spectrum rises and some large amplitude, coherent, structures are induced. The formation of this low-frequency oscillation is consistent with the previous observations of the cathode "spoke" structure that is believed to be the result of the gradient driven anti-drift instability. Fig. 6.3a also indicates the presence of high-frequency turbulence. When the magnetic field is off, we find waves that are consistent with the presence of IAT. These modes appear to be damped out with increasing magnetic field, then a new set of waves reappears at around $B = 0.5B_{max}$. This trend is better shown by Fig. 6.3b where we have estimated the energy in the high-frequency broadband oscillations as $W \sim \sum_f \left(\tilde{i}_{sat}/i_{sat,0}\right)$, where 100 kHz $< f <$ 4000 kHz. Along with this trend we also find that the frequency of these modes steadily decreases with magnetic field.

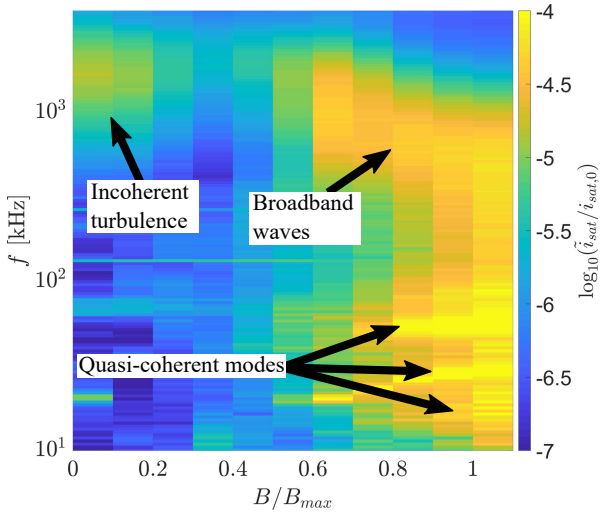

(a) Spectral content with increasing magnetic field.

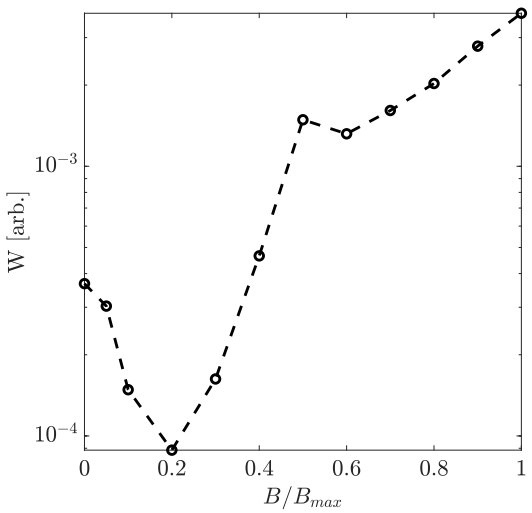

(b) Wave energy of high-frequency modes.

Figure 6.3: Wave properties of the cathode plasma in spot mode.

6.4.2.1 High-frequency Broadband Oscillations

To more clearly identify any axial or rotating modes, we must determine the direction of propagation of these waves. Wave propagation can be assessed by measuring the dispersion and calculating the phase velocity and examining its axial and azimuthal components. We determine the plasma dispersion using a pair of ion saturation probes, following the Beall estimation technique. [61, 78, 95] Given a known separation between the probes, Δx, we calculate the phase difference and corresponding wavevector for each frequency in the Fourier spectrum using Eqn. 3.2. We calculate $k(\omega)$ over 2000 times and populate a histogram to statistically represent the dispersion, $S(\omega, k)$. We note that experimentally this probe technique is subject to aliasing when the wavelength of the wave is smaller than the distance between the probes ($\Delta x = 1.5$ mm). This can result in spurious, negative wavevectors when the true wavevector is larger than $k_{max} = \pi/\Delta x \sim 2100$ [rad/m]. By examining trends in the data, we infer these smaller wavelengths.

Figure. 6.4 shows the dispersion of the plasma measured in the spot mode condition at low and high magnetic field settings. Figures. 6.4a and 6.4b are the dispersion when $B = 0$ in the axial and azimuthal direction, respectively. In the axial direction, we observe some waves (500 - 1000 kHz) that follow a linear dispersion relation ($\omega \propto k$), consistent with IAT. The waves at higher frequency and negative k (1000 - 3000 kHz) are the result of the previously discussed probe aliasing and continue on the trend of the lower frequency waves. In the azimuthal direction (Fig. 6.4b), these higher-frequency waves have some dispersion but are generally centered around $k = 0$ indicating that the waves do not primarily propagate in this direction. Figures. 6.4c and 6.4d show the dispersion for the maximum magnetic field condition. In this case, we see that the spectrum has moved to lower frequencies and longer wavelengths as well as having increased in amplitude. Furthermore, we find that with the applied magnetic field, the waves are dispersed in both the axial and azimuthal directions. Physically, this result indicates that these waves propagate in both directions, evolving helically in the plasma.

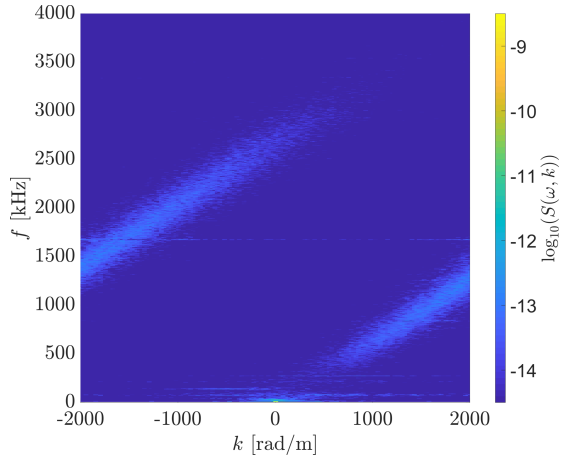

(a) Dispersion of plasma waves in the axial direction when $B = 0$.

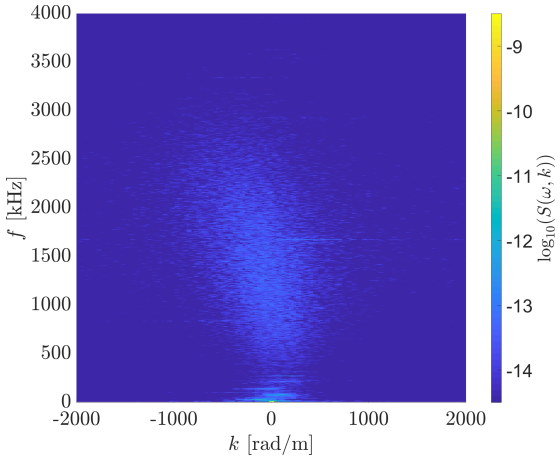

(b) Dispersion of plasma waves in the azimuthal direction when $B = 0$.

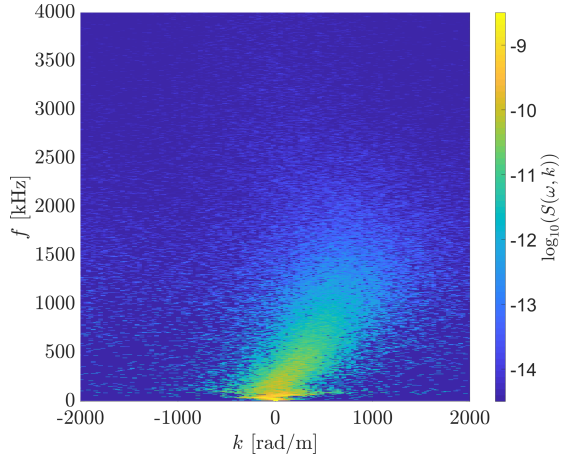

(c) Dispersion of plasma waves in the axial direction when $B = B_{max}$.

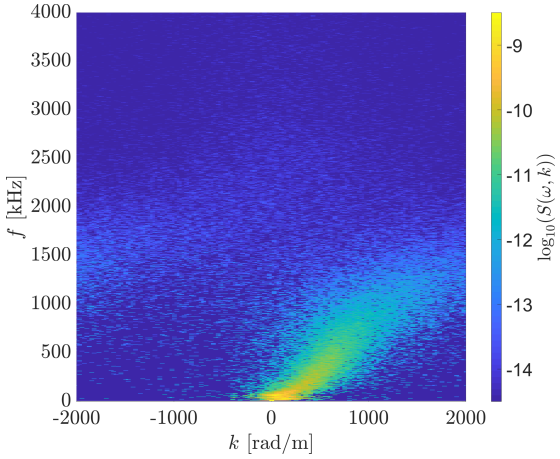

(d) Dispersion of plasma waves in the azimuthal direction when $B = B_{max}$.

Figure 6.4: The dispersion of the plasma in spot mode measured 7 mm radially and 20 mm axially downstream of the keeper exit.

From these measurements of the dispersion, we can calculate an average wavevector $\bar{k}$ as

$$\bar{k}(\omega) = \frac{\int_{-k_{max}}^{k_{max}} kS(\omega,k)dk}{\int_{-k_{max}}^{k_{max}} S(\omega,k)dk} \ . \tag{6.2}$$

Using this value, we then determine the components of the phase velocity to be

$$v_z = \frac{\omega}{\bar{k}_z^2 + \bar{k}_x^2}\bar{k}_z \ , \text{ and } \ v_x = \frac{\omega}{\bar{k}_z^2 + \bar{k}_x^2}\bar{k}_x \ , \text{ and } \ v_{ph} = \sqrt{v_x^2 + v_y^2} \ . \tag{6.3}$$

Here, we have assumed negligible propagation in the radial direction (y). For these higher frequency modes (> 100 kHz), in Fig. 6.5 we plot the phase velocity and its components as a function of magnetic field. At low magnetic fields, we see that the phase velocity is dominated by the axial propagation of waves i.e. the x component of the velocity is small compared to z. In this case, $v_{ph} \sim 4$ km/s, which is consistent with previous measurement of IAT in hollow cathodes. [3, 61] At higher magnetic fields, we find that the axial velocity decreases and the azimuthal increases while the total phase velocity is approximately constant. This result suggests that by increasing the magnetic field, that the high-frequency modes change from a purely longitudinal phenomenon to a rotating one.

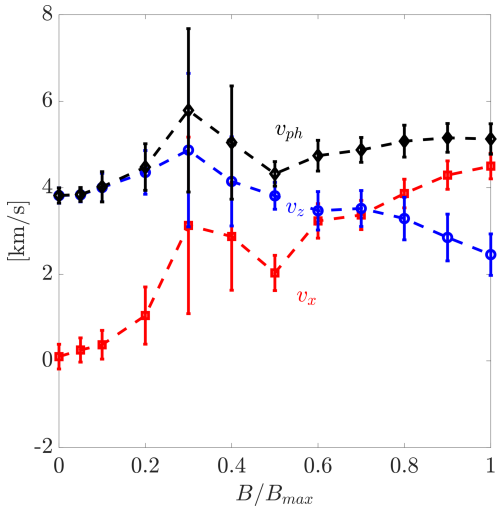

Figure 6.5: Phase velocity and components of the high-frequency, broadband modes as a function of magnetic field.

In combination, Figs. 6.3 - 6.4 indicate the following physical picture for a spot mode discharge. When no magnetic field is present, IAT propagates longitudinally in the plume and there is no coherent ionization wave present. As the magnetic field is applied, electrons begin to rotate in the plasma, the IAT is damped out, and it is replaced with broadband rotating modes at lower frequency and longer wavelength.

6.4.2.2 Low-frequency Coherent Oscillations

Up until this point, we have focused our analysis on these high-frequency modes that are associated with electrostatic turbulence. At lower frequencies in Fig. 6.3a, we observed the formation of coherent structures above a critical magnetic field strength. Zooming into our previous plots of the dispersion, we show in Fig. 6.6a and 6.6b the axial and azimuthal dispersion of these three modes. We find that at 20 kHz, we have an $m = 1$ mode that rotates and an $m = 0$ (30 kHz and second harmonic) mode that propagates axially.

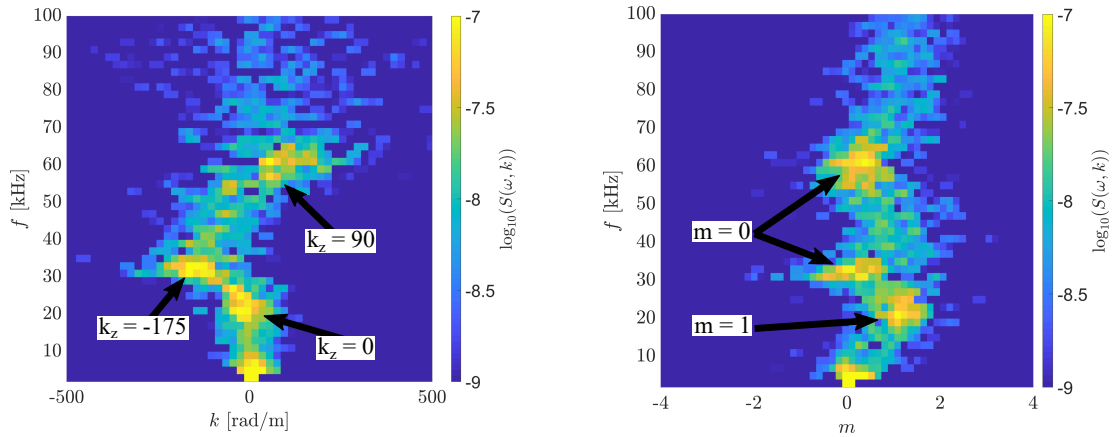

(a) Axial dispersion of low frequency modes, $B = B_{max}$

(b) Azimuthal dispersion of low frequency modes, $B = B_{max}$

Figure 6.6: Dispersion of low frequency modes at the high magnetic field condition.

Examining the azimuthal mode more closely, we can plot its phase velocity as a function of magnetic field strength. Figure 6.7 shows the results of this calculation at magnetic field conditions where this oscillation is clearly present in the Fourier transform in Fig. 6.3a. The phase velocity is constant at around $v_x \sim 1$ km/s and $v_z \sim 0$ km/s. This velocity

is near the ion sound speed, $c_s = \sqrt{T_e/m_i} \sim 1.2$ km/s for $T_e \sim 2$ eV. This azimuthally propagating wave is in qualitative agreement with previous observations of coherent anti-drift waves in the cathode plume of Hall thrusters. [90] Now we turn to the $m = 0$ mode with a fundamental frequency of 30 kHz and its harmonic (60 kHz) that are propagating longitudinally. Physically, the presence of the harmonic indicates that this wave exhibits non-sinusoidal behavior. The modes appear to be able to propagate toward ($k_z < 0$) and away from ($k_z > 0$) the cathode based on the dispersion in Fig. 6.6a. Examining the phase velocity of the fundamental oscillation, we find that it is primarily propagating in the axial direction at around -1 km/s towards the anode and its velocity is insensitive to the magnetic field. Lastly, recall from Fig. 6.3a, that these modes are increasing in strength with magnetic field. Therefore, the magnetic field is not affecting the propagation characteristics but rather influences the strength of this longitudinal mode.

The nature of these longitudinal modes is unclear. It is possible that the magnetic field is changing the plasma properties such that the plume mode ionization wave can onset; however, it is equally possible that this instability is unrelated to the plume mode, given the fact that we started this investigation with a spot mode discharge. Recent simulations of the cathode plume mode wave have been able to find longitudinal waves in the presence of a magnetic field; [5] however, they are at higher frequency (200 kHz) than we have found here and propagate faster ($v_{ph} \sim 10$ km/s). Lastly, we note that these longitudinal modes might be resident modes of the cavity since $k\ell_{ca} \sim 4$ and 8, where ℓ_{ca} is the cathode to anode distance.

To summarize our findings for this operating condition, there exist both azimuthal and longitudinal modes that are excited in the presence of the magnetic field. The rotating modes are qualitatively similar to previous measurements of anti-drift modes in partially magnetized cathode plumes. The excitation of these axial modes is not predicted by this theory and it is unclear whether the magnetic field it self is playing an important role in the onset of this mode, or if it simply changes the plasma properties such that an axial

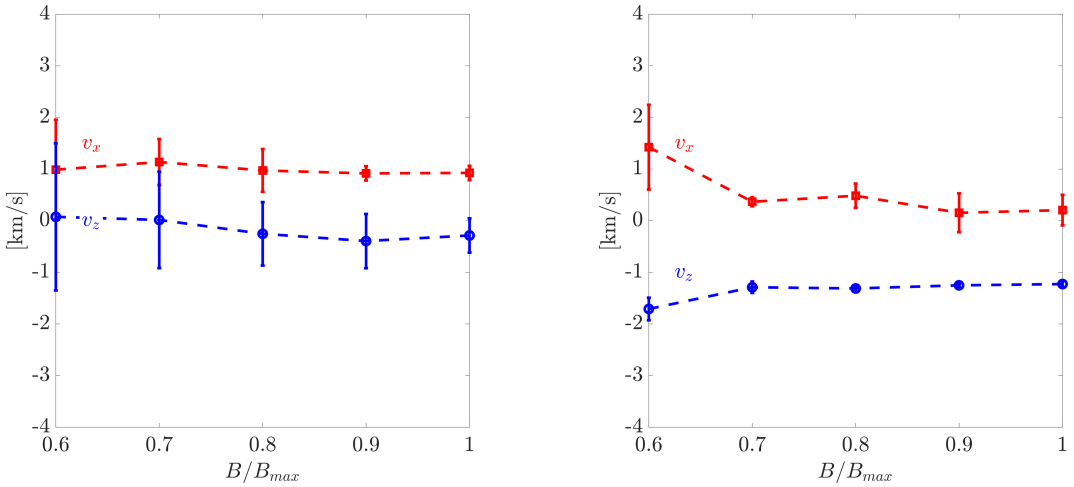

(a) Phase velocity and components of the $m = 1$ mode a function of magnetic field.

(b) Phase velocity and components of the $m = 0$ mode a function of magnetic field.

Figure 6.7: Phase velocity of low frequency structures.

mode can be excited. Furthermore, it is unclear if this wave is related to the plume mode instability. A more complete investigation of the plasma parameters is necessary for a better understanding of this longitudinal wave. Such a large experiment is outside the scope of this work.

6.4.3 Plume Mode

In this section, we replicate a similar analysis as in Sec. 6.4.2 examining the wave properties as a function of magnetic field strength. Figure 6.8a shows that there are two classes of waves in the plasma, a coherent low-frequency oscillation at 82 kHz and high-frequency, broadband waves. This low-frequency wave is consistent with our previous work on the plume mode ionization wave. Figures 6.8a and 6.8b indicate that this appears to decrease in amplitude with increasing magnetic field. This trend is further shown by plotting the peak amplitude of this wave as a function of magnetic field in Fig. 6.8c. Physically, it appears that the ionization instability damps as the magnetic field is increased. This result is in kind with previous experimental work on this instability. [2]

While Figs. 6.8a - 6.8c show that the oscillation is damped by the presence of the magnetic

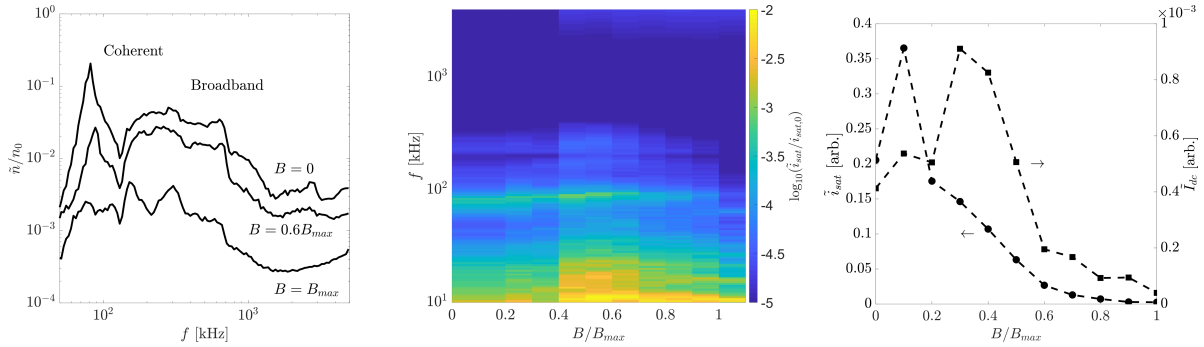

(a) Power Spectrum from ion saturation probe

(b) Power Spectrum from ion saturation probe

(c) Power Spectrum from ion saturation probe

Figure 6.8: Plume mode wave properties measured 7 mm radially and 20 mm downstream.

field, it remains to be seen if it rotates, like the structures shown in Figs. 6.3 - 6.7a. We conduct a similar analysis to Sec. 6.4.2, by first calculating the dispersion via the Beall estimation technique. The results of this analysis are shown in Figs. 6.9a - 6.9d. At low magnetic field, we find that the low-frequency wave (82 kHz) moves in towards the anode ($k > 0$) and exhibits no rotation i.e. $m \sim 0$. The broadband modes above 150 kHz are generally centered around $k = 0$ indicating that they do not propagate. In previous measurements of this instability, [81] the dispersion shows that these waves are IAT; however, this new measurement is in a more extreme ($\sim 100\%$ peak-to-peak I_{dc} oscillations) condition. Perhaps at this off-axis measurement location, the waves are primarily propagating in the radial direction, which we have not measured. In the high magnetic field setting, we find the plume mode oscillation remains at $m = 0$. Physically, this is saying that applying a magnetic field does not result in the rotation of the plume mode ionization instability.

Looking at this in more detail, we use the dispersion to calculate the phase velocity of the low-frequency wave. We show in Fig. 6.10 the propagation of the ionization instability. Here, we see that at low magnetic field, the instability propagates purely in the axial direction ($v_x = 0$) towards the anode. As we increase the magnetic field, we find that the mode changes its direction of propagation towards the cathode. In this transition region ($B = 0.2-0.4B_{max}$), the mode appears to rotate very quickly, however note that in Eqn. 6.3 when k_z and $k_x \to 0$,

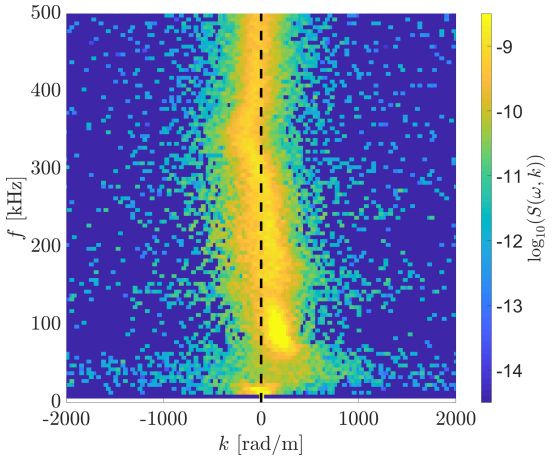

(a) Dispersion of plasma waves in the axial direction when $B = 0$.

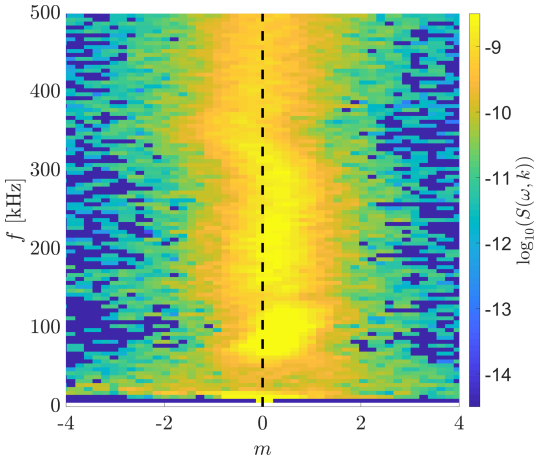

(b) Dispersion of plasma waves in the azimuthal direction when $B = 0$.

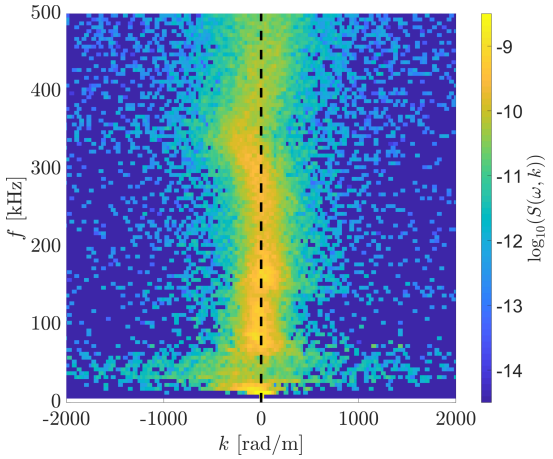

(c) Dispersion of plasma waves in the axial direction when $B = B_{max}$.

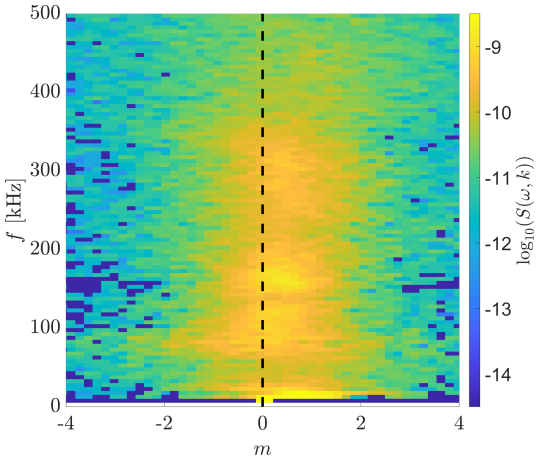

(d) Dispersion of plasma waves in the azimuthal direction when $B = B_{max}$.

Figure 6.9: The dispersion of the plasma in plume mode measured 7 mm radially and 20 mm axially downstream of the keeper exit. The vertical dashed line marks $k = 0$ or $m = 0$.

then v_z and $v_x \to \infty$. As a result, our analysis technique can lead to spuriously large phase velocities when k is small and this is likely what is happening in this transition region of the plot. At higher magnetic fields, the mode moves in the axial direction back towards the cathode with little to no rotation ($v_x \sim 0$). Our earlier work in Chapter 3 shows that the ionization instability is a localized phenomenon in the plume, from which plasma waves emanate towards the cathode and anode. [47, 82] The change in propagation direction is likely due to spatial shifting of the characteristic "active region" towards the anode, such that we measure the cathode-propagating wave at higher magnetic fields.

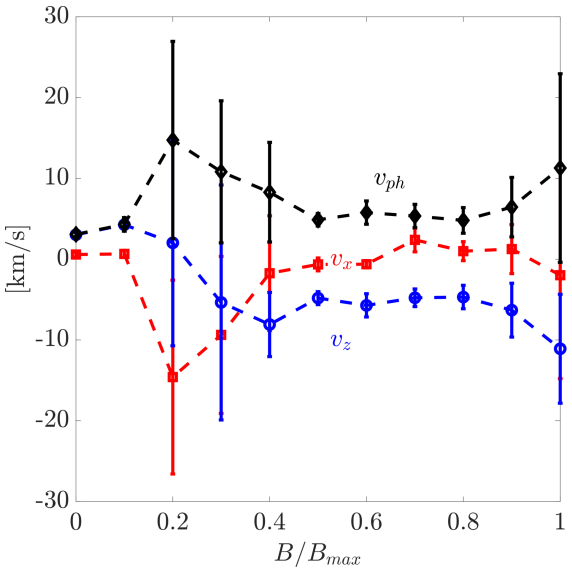

Figure 6.10: Velocity of the ionization instability.

In sum, the ionization mode propagates purely in the axial direction and is damped with increasing magnetic field. No rotational modes were observed in this condition, but this could be due to the maximum magnetic field we were able to experimentally impose on the system. We know from the camera measurement in Fig. 6.2 (b) that they do appear at a low flow rate with sufficiently high magnetic field. The behavior of the ionization instability is distinctly different from the coherent rotational mode that onset at the higher flow rate condition and it still remains unclear if the longitudinal waves found in spot mode are related to the plume mode instability.

6.5 Discussion

In this section, we focus our discussion on the propagating structures that form in the cathode plume. First, let us examine the rotating instability observed at the higher flow rate, spot mode condition. Similar structures have been observed previously in Hall thruster cathode plumes and have been described with the anti-drift wave theory similar to that presented in Sec. 6.2.2. If we take the limit of weak magnetic field, then the dispersion reduces to

$$\omega = k \cdot (c_s + u_i) \sqrt{\frac{\nu^*}{\nu_{E\times B}}} \,. \tag{6.4}$$

By further assuming the plasma approximately follows a Boltzmann relationship with negligible temperature gradients, then $T_e \nabla n/n = E$ and we arrive at a simplified expression for the dispersion

$$\omega \simeq k \cdot (c_s + u_i) \,. \tag{6.5}$$

In the azimuthal direction, $u_i = 0$ therefore we expect phase velocity in this direction to be on the order of the ion sound speed. Without a measurement of the electron temperature, we are forced to make an estimate based on previous work to evaluate the dispersion. Most measurements of cathodes show that the electron temperature is typically between 1 and 5 eV. Given this assumption and the dispersion relation, we find that the velocity should lie around 1.4 ± 0.5 km/s. Experimentally we find that once this wave is excited, its velocity does not vary with the magnetic field. This result is consistent with the theory, since the ratio $\nu^*/\nu_{E\times B}$ is independent of the applied field. The anti-drift wave model for this structure also predicts that there should be a small axial component, which our technique cannot likely distinguish from $k_z = 0$.

Further contrasting these modes, we see experimentally that in plume mode the axial ionization wave is damped by the magnetic field (Fig. 6.8c, a distinctly different behavior

from the azimuthal and longitudinal modes that grow in with increasing magnetic field (Fig. 6.3a)). Furthermore, these instabilities travel at different speeds, with the rotating and axial structures in spot mode propagate at $\mathcal{O}(1$ km/s) while the ionization mode is at $\mathcal{O}(10$ km/s). Although these modes exist in the same frequency band, given the disparity in their propagating characteristics, and behavior with an applied magnetic field, we conclude that we have observed two separate phenomena, an ionization wave and anti-drift waves. Within the bounds of our experiment, they were not found to coexist and therefore, our result indicates that the presence of a magnetic field may ultimately prevent the formation of the plume mode ionization wave in a Hall thruster. This measurement contrasts the interpretation of recent numerical simulations of these cathodes that are able to accurately reproduce the plume margin (see Fig. 2.8). [5] From our experiments we conclude that in the presence of a magnetic field, the plume margin (keeper voltage fluctuations) are likely due to the rotating modes, which are not captured by axisymmetric codes.

6.6 Conclusions

To conclude, in this Chapter we have investigated plasma waves in the cathode plume for the spot and plume modes using a high-speed camera and probes under different magnetic field conditions. Initially in spot mode, we measured ion acoustic turbulence. By varying the magnetic field, we can induce large-scale plasma structures that propagate in the axial and azimuthal directions. While the rotating mode is consistent with the an anti-drift wave in the low magnetic field limit, the origins of the longitudinal mode remain unclear, but are perhaps a resonant mode of the cathode to anode cavity. By increasing the magnetic field in plume mode, where an ionization instability was initially present, we have shown that this mode can be damped. Examining the propagation of these instabilities, we determined that the structures formed in spot mode are likely different from the ionization instability in plume mode and that, within the bounds of the experiment, they do not coexist. Furthermore,

the characteristic keeper voltage oscillations observed at low flow rates in cathodes under a magnetic field are not likely due to the ionization plume mode wave.

CHAPTER 7

Conclusions and Future Work

Predicting the onset of the plume mode instability is important for the electric propulsion community because of its link to the formation of energetic ions in the plume that cause erosion and could limit system lifetime. Several theories have been proposed for its onset, such as a current imbalance at the anode sheath, or a predator-prey ionization oscillation. However, these relatively simple descriptions have not been successful in predicting the frequency and growth characteristics of the wave. Recent numerical simulations included the non-classical effects of ion acoustic turbulence (IAT) and showed that the resulting enhanced Ohmic heating of electrons in the plume was necessary for the onset of this ionization-like wave. With that said, the success of these modified continuum models indicates that this process can be described by a multi-fluid formulation. The full fluid equations, however, are too complex to arrive at a physically intuitive, analytical description of the wave. Our goal for this work was to explore the missing links to this developing physical picture via experimentation, simplification the governing equations, and ultimately a derivation of the frequency and growth rate for this instability that we validate against experiment.

In this context, we explore the possible connection between IAT and temperature fluctuations through an experimental campaign in Chapter 3. First, we used a high-speed camera to image the instability, which for the first time showed the wave structure. The oscillation presents itself as a point source near the cathode and convects away from this region. This result lends itself to a 0 dimensional description of the oscillation at this source location.

This qualitative finding was followed by high-speed probe measurements where the plasma density and the IAT wave energy were measured over the time-scale of the plume mode oscillation. We showed for the first time that the IAT is indeed fluctuating on this time-scale. Additionally, it was highly correlated in time with the plasma density. The wave energy lead the density by around 70°. Given that the IAT amplitude likely drives the heating of electrons, the measured phase relationship between the IAT and the density is potentially causal. If the wave energy and temperature are in phase, then the density could plausibly be related to the IAT through ionization. The IAT amplitude, the density, and the light emission were analyzed across the plume over the time-scale of the wave. We found that the density, light emission and IAT were also highly correlated in time and the results further corroborated the interpretation of this mode as one that is locally formed and convected. The final exploratory experiment used a collection of high-speed probes to measure the plasma properties as a function of time and space in the plume. First we showed that indeed the IAT is the dominant form of electron resistivity in the plume. Then, we examined the fluctuations in electron temperature, where we found that the peak-to-peak fluctuations had a local maximum near the cathode. This feature was consistent with our high-speed camera measurements of a localized spatial structure. We chose to conduct our time-resolved analysis at the point where the oscillation in temperature was greatest as this is the "source" region where a simplified analytical theory may ultimately apply. Here, we found that the IAT drives large-scale fluctuations in the plasma resistivity. Investigating the temperature, density and velocity of the electrons, we find that the anomalous collision frequency leads the temperature, which leads the density. The density lags the temperature by 70°, which is consistent with ionization being the link between the two parameters. There was a small phase delay between the density and electron drift that gave rise to the current oscillations that are characteristic of the plume mode. All together, these preliminary experimental results built-up to the following interpretation. Heating from the IAT modulates the electron temperature in the plume and destabilizes an underlying predator-prey instability between

the electrons and neutrals.

This physical description was examined in Chapter 4 through an analysis of the fluid equations to arrive at a first-principles understanding for the onset of the wave. The experimental results suggested that we can simplify the fluid equations such that plasma diffusion is balanced by ionization, the ionization of neutrals is balanced by the influx, and heating from the IAT is balanced by inelastic ionization collisions and energy flux. In this reduced fidelity model, we then perturbed the electron density, temperature, velocity, and collision frequency as well as the neutral density. We took care to also perturb the ionization rate and ion-neutral collision frequency as they explicitly depend on densities and temperature. We applied three different models for the electron collision frequency. First we assumed that the electron resistivity is driven by classical Coulomb collisions. In this limit, the electrons experience very few collisions per transit, meaning the Ohmic heating is negligible. The end result is that the wave is oscillates at a similar frequency as predicted by the classic predator-prey model used for Hall thrusters but is unconditionally damped out by plasma diffusion and the neutral influx. Next we modeled the collision frequency as constant and large. In this case, the electrons experience many collisions per transit. We found that the mode can grow if ionization due to electron temperature variations is able to overcome the diffusion losses. Lastly, we applied a model based on saturated IAT and arrived at a similar result to the constant case. This supports the idea that the mechanism for enhanced collisionality is not necessarily important, only that it is high and that temperature can fluctuate. Increased Ohmic electron heating due to IAT is a realistic mechanism by which this can occur. We next applied this theory to examine our earlier measurement in Chapter 3 and showed that it was able to predict the frequency of oscillation and the growth of the ionization instability in the plume region of the cathode. Lastly, the onset criterion was rewritten in terms of the discharge operating conditions. We found that it can be expressed as critical electron temperature that depends weakly on the neutral density, when the neutral density is large. Since the mode onsets near the cathode, where the atom density is high, we predicted that

this critical parameter is likely invariant. Lastly, we showed that this can be thought of as a threshold discharge voltage for the wave to onset.

Building upon this initial success of our model, we conducted another experiment where we measured the steady-state plasma parameters and wave properties as a function of discharge current, and mass flow rate, position in the plume. We found that the IAT amplitude generally rises with greater current and lower flow rate. The same trends held for the amplitude of the electron temperature, indicative of the enhanced Ohmic heating of electrons. We evaluated our theory near the cathode as this appeared to be where the wave originates. We used the relevant limiting case of our analytical model where the Ohmic heating due to IAT is strong. The theoretical frequency and growth rate were compared to the global discharge current oscillation frequency and amplitude, respectively. Overall, our theory was able to capture the trends with flow rate and discharge current. We find that both the measured and theoretical oscillation frequencies increased with lower flow rate and higher discharge current. Further, we found that the calculated frequency captured the observed trends in the data; however, it is generally lower. We suspected that this could be due to a lower than expected ionization fraction, or because we have not considered the role of the electron kinetic energy in ionization, which could be significant. Conducting a correlation analysis, we found that the 25 A condition was highly correlated, whereas the 20 A condition was negatively correlated with the theory. It is possible that at lower current conditions, where diffusion is lower, that some of our assumptions may not apply and causes the negative correlation. We next compared the wave amplitude to our expected growth rate. Our model predicted growth for all the conditions except for one at 15 A and 5 sccm. Above the 15 A conditions, the plume mode growth rate increased with current and lower mass flow rate. This trend matched the experimental data. Below 15 A, where our model can predict that the wave is damped, we found an inverse trend with gas flow rate. This contradicted our experimental observations. It was suggested that ion inertia or the ionization rate may also contribute to the ion drag, which could change the dependence of diffusion on neutral

density and cause this discrepancy. A correlation analysis showed that for the 20 A to 30 A conditions, the predicted growth rate and discharge current amplitude are highly correlated. This result supports our theory from Chapter 4. Lastly we examined the novel idea that the wave onsets at critical voltage, rather than the traditional $I/\dot{m}$ dependence. We found that the wave amplitude is highly correlated with the discharge voltage and that a clear mode transition occurs between 15 and 20 V. The relatively constant onset voltage indicated that the critical voltage may be independent of discharge current or mass flow rate, as predicted by our theory.

In our final chapter, we examined the plume mode oscillation in the presence of a magnetic field. First we showed qualitatively using the high-speed camera that when we apply a magnetic field to a cathode in plume mode, the ionization instability disappears and is replaced by propagating azimuthal modes. It was shown that with increasing magnetic field, the wave was damped and that rotating modes, consistent with anti-drift waves, were able to propagate. This result suggests that the plume mode wave may ultimately be damped in a Hall thruster. Previous experimental results on cathodes in magnetic fields showed similar behavior. The formation of longitudinal propagating waves in spot mode may be related to the findings of recent simulations cathodes where longitudinal oscillations are found with an applied magnetic field, rather than the plume mode instability. Our results suggested that these may be resident modes of the cathode-anode cavity.

The major contributions of this work can be summarize as the responses to the questions outlined in Chapter 2. These are

1. What is the structure of the plume mode oscillation?

   The plume mode instability is a dynamic phenomenon with a localized source from which structures propagate.

2. Is the wave actually related to ionization?

   Yes, changes in electron temperature drive variations in the ionization rate.

3. How is IAT connected to the wave?

   The turbulence can fluctuate on time-scale of the plume mode and drives fluctuations in electron temperature.

4. What is the energy source for driving this wave unstable?

   The explicit energy source for the wave is the electron temperature, however, since it is driven by IAT collisions the most fundamental energy source is the electron kinetic energy.

5. Can we derive a self-consistent theory for the instability?

   The plume mode instability can be described as a predator-prey oscillation that is driven unstable by the temperature fluctuations due to the presence of turbulence.

6. Does the onset criterion predict the experimentally observed onset of the wave?

   The onset criterion for the plume mode is related a critical electron temperature in the plasma above which ionization overcomes diffusion. Turbulent heating of electrons is necessary to achieve these temperatures. The theory can be used to predict the growth of the wave.

7. Will this phenomenon be observed in cathodes operating in Hall thrusters?

   The plume mode instability is damped by magnetic fields and anti-drift waves form in its place. Our work suggests the plume mode will not be observed.

7.1 Future Work

The following additional experiments may be useful for further validating the theory:

1. Combine non-invasive measurements of the electron temperature and density using Thomson scattering with measurements of the neutral density to more precisely evaluate the theory.

2. Conduct a numerical experiment and evaluate the results with our analytical theory to determine if the code accurately reproduces the properties of the instability.

3. Evaluate the onset criterion of the plume mode wave in a cathode at low flow rate under an axial magnetic field by measuring the plasma parameters in the plume. This can be used to show definitively that the wave is damped in the presence of a magnetic field.

4. Conduct a similar experiment in a Hall thruster to similarly show damping.

From a theoretical perspective, additional work could be used to show why the presence of a magnetic field damps the wave. Is it that the temperature is lower? Or does the magnetization of the electrons substantially change the system of equations? This could perhaps be used to tailor the magnetic field near the cathode or be useful for extrapolating to the stability for externally mounted cathodes in Hall thrusters. Lastly the onset criterion could potentially be used to identify new design laws for high-power Hall thrusters.

Appendices

Appendix A

Alternative Derivation: Ionization Drag

A.1 Introduction

In this appendix, we explore the assumption the dominant form of drag for the ions is ion-neutral collisions. However, the cathode plume is known to be largely collisionless. Therefore, it is possible that other forms of drag may be reducing the free diffusion of the plasma. Ionization can also act as an effective drag on the ions. This process increases the number of slow particles and therefore reduces the average momentum of the ions and electrons. If indeed this is the dominant process, then our simplification of the ion equations changes and leads to a slightly different interpretation of the ionization wave.

A.2 Modification of the Ion Equations in the Presence of Strong Ionization Drag

In this section, we modify our derivation of the ion equations such that ambipolar electric fields are now assumed balanced by ionization drag rather than ion-neutral collisions or ion inertia.

A.2.1 Plasma Equations

Under the assumption that quasineutrality holds on the relatively long time-scales of this instability, the ion continuity equation is given by

$$\frac{\partial n}{\partial t} + \nabla \cdot (n u_i) = n \nu_{iz}(n_n, T_e) \ , \tag{A.1}$$

where ν_{iz} is the ionization rate of the plasma, which depends on the neutral density and electron temperature. This expression reflects the fact that the variations in plasma density are the result of changes in ion flux and ionization. We have assumed that ion losses through re-combination type processes are not a critical part of the mechanism that determines

stability and oscillation. Physically, this is justified by the low classical collision frequency between electrons and ions in the plume, along with the fact that there are no nearby surfaces in this region by which recombination can be mediated. Similarly, we write the electron continuity equation as

$$\frac{\partial n}{\partial t} + \nabla \cdot (n u_e) = n \nu_{iz} \ . \tag{A.2}$$

Combining the electron and ion continuity equations, we arrive at

$$\frac{\partial n}{\partial t} + \nabla \cdot (n u_i) = n \nu_{iz} \tag{A.3}$$

$$\nabla \cdot (n u_e) = \nabla \cdot (n u_i) \ . \tag{A.4}$$

From our physical description, we suspect that the electrons are driving the wave. Therefore it is convenient to express the ion velocity in terms of other electron parameters and reduce the order of the problem. With this goal in mind, we examine the momentum equations to find such an expression for the ion velocity. We write the ion momentum equation as

$$m_i \frac{\partial n u_i}{\partial t} + m_i (u_i \nabla \cdot (n u_i) + n u_i \nabla \cdot (u_i)) = nqE - n m_i (u_i - u_n) \nu_{in} - n m_e (u_i - u_e) \nu_{ei} - \nabla (n T_i) \ . \tag{A.5}$$

Here m_i is the ion mass, q is the unit charge, E is the electric field, ν_{in} is the ion-neutral collision frequency, T_i is the ion temperature, and ν_{ei} is the electron-ion collision frequency. Equation A.5 describes the change in ion momentum that is dictated by the acceleration due to electric fields and collisional effects. Collisions between ions and neutrals lead to a loss of ion momentum because the ions move quickly compared to the neutrals. Conversely, collisions between electrons and ions lead to an increase in ion momentum, although because of the disparity in the electron and ion mass, little momentum is generally transferred in this manner. The electron momentum is described by an Ohm's law, having neglected the

electron inertia given their small mass:

$$0 = -nqE - \nabla(nT_e) - nm_e(u_e - u_i)\nu_{ei} - nm_e(u_e - u_n)\nu_{en} \ . \tag{A.6}$$

We simplify the momentum equations using a velocity hierarchy that is known to apply to the cathode plasma. [63] We will assume that $u_n \ll u_i \ll u_e$, allowing us to simplify momentum equations to

$$m_i\frac{\partial nu_i}{\partial t} + m_i(u_i\nabla\cdot(nu_i) + nu_i\nabla\cdot(u_i)) = nqE - nm_iu_i\nu_{in} + nm_eu_e\nu_{ei} - \nabla(nT_i) \tag{A.7}$$

$$0 = -nqE - \nabla(nT_e) - nm_eu_e\nu_{ei} - nm_eu_e\nu_{en} \ . \tag{A.8}$$

Combining these two expressions, we can eliminate the electric field to find that

$$m_i\frac{\partial nu_i}{\partial t} + +m_i(u_i\nabla\cdot(nu_i) + nu_i\nabla\cdot(u_i)) = -\nabla(n(T_e + T_i)) + m_eu_e\nu_{en} - m_iu_i\nu_{in} \ . \tag{A.9}$$

With the ratio of the masses being $\mathcal{O}(10^{-6})$, we can neglect the effect of electron neutral collisions on the total ion momentum. Additionally, we know that the ion pressure is typically low compared to that of the electrons in these plasmas. [6] By combining with the ion continuity equation, we find

$$nm_i\frac{\partial u_i}{\partial t} + m_iu_i(\nu_{in} + \nu_{iz} + \nabla\cdot u_i) = -\nabla(nT_e) \tag{A.10}$$

At this point in the derivation, we deviate from the procedure in Chapter. 4 and assume that $\nu_{iz} \gg \nu_{in}$ and we continue to neglect changes in ion inertia. This leaves us with

$$nm_iu_i\nu_{iz} = -\nabla(nT_e) \tag{A.11}$$

$$\nabla\cdot(nu_i) = -\frac{\nabla^2(nT_e)}{m_i\nu_{in}} \tag{A.12}$$

Physically, this implies that the change in ion flux is the result of ambipolar diffusion where ionization drag is balanced by the ambipolar electric field. Substituting this back into the continuity equation, we find that

$$\boxed{\frac{\partial n}{\partial t} - \frac{\nabla^2(nT_e)}{m_i \nu_{iz}} = n\nu_{iz}} \tag{A.13}$$

For the electrons, then we have from Eqn. A.4

$$\boxed{\nabla \cdot (nu_e) = -\frac{\nabla^2(nT_e)}{m_i \nu_{iz}}} \,. \tag{A.14}$$

Physically, these equations show that the plasma particle conservation is a balance between diffusion processes and ionization. For the sake of brevity, the derivation of the neutral and energy equations and the 0 dimensional assumption remain the same as in Chapter. 4.

A.2.2 Summary of Equations and Assumptions

Here we present the complete set of equations that we will perturb in order to describe the ionization wave associated with the cathode plume mode. In this model, the plasma and neutral particle interactions are related through the ion and neutral continuity equations. Changes in density, temperature are connected through the electron continuity equation and the energy equation. All together, the primary effects that we are considering here are Ohmic heating of electrons, ionization, and diffusion, which will ultimately form the basis for the ionization instability.

$$
\begin{aligned}
\frac{\partial n}{\partial t} + \frac{(nT_e - T_{e,in}n_{in})}{m_i \nu_{iz} L^2} + 2\frac{nT_e}{m_i \nu_{iz} R^2} &= n\nu_{iz} \\
\frac{(nu_e - n_{in}u_{e,in})}{L} &= \frac{(nT_e - T_{e,in}n_{in})}{m_i \nu_{iz} L^2} + 2\frac{nT_e}{m_i \nu_{iz} R^2} \\
\frac{\partial n_n}{\partial t} &= \frac{n_{in} - n_n}{L} u_n - n\nu_{iz} \\
\frac{3}{2}\frac{\partial T_e}{\partial t} + \frac{T_e u_e - T_{e,in}u_{e,in}}{L} + \frac{1}{2}u_e \frac{T_e - T_{e,in}}{L} &= m_e u_e^2 \nu_e - \epsilon_{iz}\nu_{iz}
\end{aligned}
\tag{A.15}
$$

To arrive at this set of equations, we have made the assumption that the problem can be represented with a 0 dimensional model with influx and outflux conditions and that the influx is constant in time. This is justified by localized nature of the plume mode (see Fig. 3.2) and that the plasma in the emitter region is not fluctuating. [2] The neutral particle velocity is considered to change slowly across our 0 dimensional volume, an assumption that follows those used in numerical models that are also able to recover the instability. [5] Furthermore, we have associated our control volume with the density gradient lengthscales. Lastly, we have applied the hierarchy in Tab. A.1 to reduce the initially complicated set of equations.

Table A.1: Assumptions used in the development of governing equations for an ionization instability that describes the plume mode.

Parameters	Hierarchy
Velocity	$u_n \ll u_i \ll u_e$
Frequency	$\omega \sim \nu_{iz} < \nu_{in}$
Energy	$T_n \ll T_i \ll T_e \ll \epsilon_{iz}$

A.3 Linear Perturbation Analysis

Now, we conduct our linear perturbation analysis of Eqns. A.15. We expand the outlet condition, using the convention $x = x_0 + x_1 e^{-i\omega t}$, where x_0 is the steady state condition and x_1 represents a small fluctuation on top of that steady state value. Consistent with the measurements in Chapter 3, we recognize that the density, electron temperature, electron

drift velocity, and anomalous collision frequency vary in time. We therefore allow these to be perturbed in the governing equations. We similarly note that the ionization and ion-neutral collision frequencies is an explicit function of density and cross section, which depends on electron temperature for ionization. These too are perturbed. First we establish the steady-state criteria, then we perturb each individual expression. The equations are then combined to determine the characteristic polynomial for the oscillation. This is analyzed and simplified, using the assumptions in Tab. A.1.

A.3.1 Steady-state Conditions

Here we examine the steady state criteria and discuss them in the context of the mechanism we have proposed for the instability. First we begin with the ion continuity equation. We have that

$$\frac{n_0 T_0 - T_{e,in} n_{in}}{m_i \nu_{iz,0} L^2} + 2\frac{n_0 T_{e0}}{m_i \nu_{iz,0} R^2} = n_0 \nu_{iz,0} \tag{A.16}$$

For the electron continuity equation we find

$$\frac{n_0 u_{e0} - n_{in} u_{e,in}}{L} = \frac{n_0 T_0 - T_{e,in} n_{in}}{m_i \nu_{iz,0} L^2} + 2\frac{n_0 T_{e0}}{m_i \nu_{iz,0} R^2} \tag{A.17}$$

$$\frac{n_0 u_{e0} - n_{in} u_{e,in}}{L} = n_0 \nu_{iz,0} \tag{A.18}$$

$$\frac{n_0 u_{e0}}{L} = n_0 \nu_{iz,0} + \frac{n_{in} u_{e,in}}{L} \ . \tag{A.19}$$

We interpret $n_{in} u_{e,in}$ as the current drawn from the plasma in the orifice region and $n_0 u_{e0}$ and the current demanded by the anode. This result implies that steady ionization in the plasma is able to supplement the current out of the cathode to meet the steady-state current required by the power supply. For the neutral continuity, we find that

$$\frac{n_{n,in}}{L} u_n = n_0 \nu_{iz} + \frac{n_{n0}}{L} u_n \ , \tag{A.20}$$

which states that the inlet neutral gas must be equal to the sum of the outlet and the losses to ionization. Alternatively, we can substitute in the steady-state electron continuity equation to show that

$$\frac{n_{n,in} - n_{n0}}{L} u_n = \frac{n_0 u_{e0} - n_{in} u_{e,in}}{L} \ . \tag{A.21}$$

This implies that neutral gas is consumed by ionization if the electron current demanded by the power supply is greater than the internal cathode plasma can provide. Lastly, examining the steady-state electron energy equation, we find that

$$\frac{T_{e0} u_{e0} - T_{e,in} u_{e,in}}{L} + \frac{1}{2} T_{e0} \frac{u_{e0} - u_{e,in}}{L} = m_e u_{e0}^2 \nu_{e0} - \epsilon_{iz} \nu_{iz,0} \ . \tag{A.22}$$

This result tells us that the outlet heat flux of the volume will be greater than the inlet heat flux if the electrons experience sufficient Ohmic heating to exceed the ionization losses.

In summary, the steady-state conditions we use for our perturbation are

$$\begin{aligned}
\frac{T_{e0} n_0 - T_{e,in} n_{in}}{m_i \nu_{iz,0} L^2} + 2 \frac{n_0 T_{e0}}{m_i \nu_{iz,0} R^2} &= n_0 \nu_{iz,0} \ , \\
\frac{n_0 u_{e0} - n_{in} u_{e,in}}{L} &= n_0 \nu_{iz,0} \ , \\
\frac{n_0 - n_{in}}{L} &= n_0 \nu_{iz,0} \ , \\
\frac{T_{e0} u_{e0} - T_{e,in} u_{e,in}}{L} + \frac{1}{2} T_{e0} \frac{u_{e0} - u_{e,in}}{L} &= m_e u_{e0}^2 \nu_{e0} - \epsilon_{iz} \nu_{iz,0} \ .
\end{aligned} \tag{A.23}$$

Overall, these results make physical sense for the cathode plasma. Ionization is balanced by diffusion and is necessary to increase the current density in the plasma to maintain the discharge current. Conversely this can be expressed as the rate at which neutral gas must be consumed to ensure current continuity. This interpretation of the equations physically links the oscillations in discharge current to those in neutral density through the predator-prey mechanism. Lastly, the heat flux across the volume can be increased if sufficient Ohmic heating occurs in the plasma to overcome losses due to ionization.

A.3.2 Ion Continuity

Starting with the linear perturbation of the ion continuity equation,

$$\frac{\partial n}{\partial t} + \frac{nT_e - T_{e,in}n_{in}}{m_i \nu_{iz} L^2} + 2\frac{nT_e}{m_i \nu_{in} R^2} = n\nu_{iz} \tag{A.24}$$

$$\nu_{iz}\frac{\partial n}{\partial t} + \frac{nT_e - T_{e,in}n_{in}}{m_i L^2} + 2\frac{nT_e}{m_i R^2} = n\nu_{iz}^2 \tag{A.25}$$

$$-i\omega\nu_{iz,0}n_1 + \left(\frac{n_1}{n_0} + \frac{T_{e1}}{T_{e0}}\right)\frac{n_0 T_{e0}}{m_i L^2} + 2\frac{n_0 T_{e0}}{m_i R^2}\left(\frac{n_1}{n_0} + \frac{T_{e1}}{T_{e0}}\right) = n_0\nu_{iz,0}^2\left(\frac{n_1}{n_0} + 2\frac{n_{n1}}{n_{n0}} + 2\frac{\gamma_{iz}}{\nu_{iz,0}}\frac{T_{e1}}{T_{e0}}\right) . \tag{A.26}$$

Here we have defined $\gamma_{iz} \equiv T_{e0}\partial\nu_{iz}/\partial T_e$, which in physical terms represents the change in the ionization rate due to temperature variations. Mathematically, it is the result of a Taylor expansion of the ionization rate near the steady state temperature ($\nu_{iz} = \nu_{iz,0} + \frac{\partial\nu_{iz}}{\partial T_e}(T_e - T_{e0})$). Dividing by the ion-neutral collision rate, we find that

$$-i\omega\frac{n_1}{n_0} + \left(\frac{n_1}{n_0} + \frac{T_{e1}}{T_{e0}}\right)\frac{T_{e0}}{m_i\nu_{iz,0}} + 2\frac{T_{e0}}{m_i\nu_{iz,0}R^2}\left(\frac{n_1}{n_0} + \frac{T_{e1}}{T_{e0}}\right) = \nu_{iz,0}\left(\frac{n_1}{n_0} + 2\frac{n_{n1}}{n_{n0}} + (2\beta - 1)\frac{T_{e1}}{T_{e0}}\right) . \tag{A.27}$$

where $\beta \equiv \gamma_{iz}/\nu_{iz,0}$ is a non-dimensional parameter. When $|\beta| \gg 1$, then temperature fluctuations are important i.e. the ionization rate has a greater than linear dependence on electron temperature, where as $|\beta| \ll 1$, then temperature fluctuations are not as important. For a low temperature xenon plasma, $\beta \sim \mathcal{O}(1-10)$. Greater T_e leads to smaller β. We apply the steady state condition and divide out by the outlet density.

$$-i\omega\frac{n_1}{n_0} + \left(\frac{n_1}{n_0} + \frac{T_{e1}}{T_{e0}}\right)\frac{n_{in}}{n_0}\frac{T_{e,in}}{m_i\nu_{iz,0}L^2} = \nu_{iz,0}\left(2\frac{n_{n1}}{n_{n0}} + (2\beta - 1)\frac{T_{e1}}{T_{e0}}\right) \tag{A.28}$$

Now we will define $D_{iz} = T_{e,in}/m_i\nu_{iz,0}$, and $\nu_{Diz} = D_{iz}/L^2$ is the diffusion rate of the plasma due to the ambipolar electric field balancing against the effective drag ionization.

$$-i\omega\frac{n_1}{n_0} + \left(\frac{n_1}{n_0} + \frac{T_{e1}}{T_{e0}}\right)\frac{n_{in}}{n_0}\nu_{Diz} = \nu_{iz,0}\left(2\frac{n_{n1}}{n_{n0}} + (\beta - 1)\frac{T_{e1}}{T_{e0}}\right) \tag{A.29}$$

Dividing by the ionization rate to non-dimensionalize the equation, and defining $\zeta_{iz} \equiv n_{in}\nu_{Diz}/n_0\nu_{iz,0}$ and $x = \omega/\nu_{iz,0}$ such that

$$\frac{n_1}{n_0}(-ix + \zeta_{iz}) = 2\frac{n_{n1}}{n_{n0}} + \frac{T_{e1}}{T_{e0}}(\beta - 1 - \zeta_{iz}) \tag{A.30}$$

Physically, when $\zeta_i \gg 1$ then the then diffusion losses are much greater than ionization and when $\zeta_i \ll 1$ then plasma production due to ionization is greater than the diffusion losses. Notably, in expression we find that if $\beta > \zeta_i + 1$, then changes in electron temperature will enhance the changes plasma density.

A.3.3 Electron Continuity

Conducting the perturbation of the electron continuity equation, we find

$$\frac{(nu_e - n_{in}u_{e,in})}{L} = \frac{nT_e - T_{e,in}n_{in}}{m_i\nu_{iz}L^2} + 2\frac{nT_e}{m_i\nu_{in}R^2} \tag{A.31}$$

$$\nu_{iz}\frac{(nu_e - n_{in}u_{e,in})}{L} = \frac{nT_e - T_{e,in}n_{in}}{m_iL^2} + 2\frac{nT_e}{m_iR^2} \tag{A.32}$$

$$\nu_{iz,0}\left(\frac{n_0u_{e0} - n_{in}u_{e,in}}{L}\right)\left(\frac{n_{n1}}{n_{n0}} + \beta\frac{T_{e1}}{T_{e0}}\right) + \nu_{iz,0}\frac{n_0u_{e0}}{L}\left(\frac{n_1}{n_0} + \frac{u_{e1}}{u_{e0}}\right) = \left(\frac{n_1}{n_0} + \frac{T_{e1}}{T_{e0}}\right)\left(\frac{n_0T_{e0}}{m_iL^2} + 2\frac{n_0T_{e0}}{m_iR^2}\right) . \tag{A.33}$$

Applying the state state condition for the electron continuity equation simplifies the result to

$$\nu_{in,0}\left(\frac{n_0u_{e0} - n_{in}u_{e,in}}{L}\right)\left(\frac{n_{n1}}{n_{n0}} + (\beta - 1)\frac{T_{e1}}{T_{e0}}\right) + \nu_{in,0}\frac{n_0u_{e0}}{L}\left(\frac{u_{e1}}{u_{e0}}\right) + \nu_{in,0}\frac{n_{in}u_{e,in}}{L}\frac{n_1}{n_{in}} = \left(\frac{n_1}{n_0} + \frac{T_{e1}}{T_{e0}}\right)\frac{n_{in}T_{e,in}}{m_iL^2} \tag{A.34}$$

Now we nondimensionalize the expression by dividing by $\nu_{in}n_{in}u_{e,in}/L$ to find that

$$\left(\frac{n_0u_{e0}}{n_{in}u_{e,in}} - 1\right)\left(\frac{n_{n1}}{n_{n0}} + (\beta - 1)\frac{T_{e1}}{T_{e0}}\right) + \frac{n_0u_{e0}}{n_{in}u_{e,in}}\left(\frac{u_{e1}}{u_{e0}}\right) + \frac{n_1}{n_0} = \left(\frac{n_1}{n_0} + \frac{T_{e1}}{T_{e0}}\right)\frac{T_{e,in}}{m_i\nu_{in,0}L^2}\frac{L}{u_{e,in}} . \tag{A.35}$$

We can express this equation differently by applying the steady state condition and the result simplifies

$$\frac{L}{\lambda_{iz}}\left(\frac{n_{n1}}{n_{n0}}+\frac{u_{e1}}{u_{e0}}+(\beta-1)\frac{T_{e1}}{T_{e0}}\right)+\frac{u_{e1}}{u_{e0}}=\frac{n_1}{n_0}\left(\frac{\lambda_{in}}{L}\frac{1}{M_{e,in}^2}\frac{m_e}{m_i}-1\right)\ . \tag{A.36}$$

Experimentally, we know the electron Mach number is $\mathcal{O}(1)$, the ratio λ_{in}/L is between 10^2-10^3 and $m_e/m_i\sim 10^{-6}$ (See Chapter 3), therefore, we can neglect this term and simplify our expression to

$$\epsilon\left(\frac{n_{n1}}{n_{n0}}+\frac{u_{e1}}{u_{e0}}+(\beta-1)\frac{T_{e1}}{T_{e0}}\right)+\frac{u_{e1}}{u_{e0}}=-\frac{n_1}{n_0}\ . \tag{A.37}$$

Here we have defined the nondimensional parameter $\epsilon=L/\lambda_{iz}$, which we know experimentally should be small for the cathode plasma, $\mathcal{O}(10^2-10^3)$.

A.3.4 Summary of Equations

Equation A.38 shows the set of perturbed equations that we combine to solve for the dispersion.

$$\begin{aligned}
\frac{n_1}{n_0}(-ix+\zeta_{iz}) &= 2\frac{n_{n1}}{n_{n0}}+\frac{T_{e1}}{T_{e0}}(2\beta-1-\zeta_{iz})\\
\epsilon\left(\frac{n_{n1}}{n_{n0}}+\frac{u_{e1}}{u_{e0}}+(\beta-1)\frac{T_{e1}}{T_{e0}}\right)+\frac{u_{e1}}{u_{e0}} &= -\frac{n_1}{n_0}\\
\frac{n_{n1}}{n_{n0}}(-ix) &= -\alpha\left(\frac{n_1}{n_0}+\beta\frac{T_{e1}}{T_{e0}}\right)\\
\left(\frac{3}{2}\frac{T_{e1}}{T_{e0}}+\frac{u_{e1}}{u_{e0}}\right)(\epsilon+\delta) &= \eta\left(\frac{u_{e1}}{u_{e0}}+\frac{\nu_1}{\nu_0}+\frac{T_{e1}}{T_{e0}}\right)
\end{aligned} \tag{A.38}$$

A.4 Oscillation and Growth

More recent numerical simulation of hollow cathodes use the same model derived by Sagdeev, but more accurately include the temperature dependence

$$\nu_{an} = \alpha_2 \omega_{pe} M_e \frac{T_e}{T_i} \tag{A.39}$$

where α_2 is a constant of order 10^{-2}. Including this now into the energy equation, under the assumption that the ion temperature does not fluctuate strongly, we find that

$$\left(\frac{3}{2}\frac{T_{e1}}{T_{e0}} + \frac{u_{e1}}{u_{e0}}\right)(\epsilon + \delta) = \eta\left(2\frac{u_{e1}}{u_{e0}} + \frac{1}{2}\frac{n_1}{n_0} + \frac{3}{2}\frac{T_{e1}}{T_{e0}}\right) . \tag{A.40}$$

This is only a slight modification of the energy equation from what we found with the previous Sagdeev model. Making the same assumption that electrons experience many collisions ($\eta \gg \delta \gg \epsilon$) and solving for the dispersion

$$D(x) = x^2 - ix\,(2\beta - 2\zeta_{iz} - 1) - 2\alpha\,(1 + \beta) \ . \tag{A.41}$$

The frequency and growth rate in the limit that the imaginary component of the dispersion is small compared to the real component are

$$\omega_r \simeq \sqrt{2\alpha(\nu_{iz,0}^2 + \gamma_{iz}\nu_{iz,0})} \tag{A.42}$$

$$\gamma = \gamma_{iz} - \frac{n_{in}}{n_0}\nu_{Diz} - \frac{\nu_{iz,0}}{2} \tag{A.43}$$

The result is very similar to the previous result in Chapter 4, which is unsurprising given that form of the equations has changed little between the two cases. Setting the growth rate to zero, we have a linear differential equation (a form of Bernoulli's equation) that we can

solve for the critical growth and damping factors. Doing this, we find that

$$\nu_{iz,0}^{crit} = \frac{1}{L}\sqrt{2\frac{T_e}{m_i}\ln(T_e) + cT_e} = \sqrt{2\ln(T_e)}\frac{c_s}{L} \ , \tag{A.44}$$

where we have taken the integration constant, $c = 0$. As was discussed at length in Chapter 4, this onset criterion can be represented as a critical electron temperature that depends on the neutral gas density. Physically, this indicates that above a certain temperature ionization will enhance particle production above the rate at which the ambipolar electric field can force plasma diffusion. In contrast to the previous result in Chapter 4, here we do not strictly require ion-neutral collisions to occur in the plasma to resolve an instability. Furthermore, we have weakened the inverted dependence on the neutral density. The onset criterion now only depends on the neutral density through ionization rate, in comparison to the previous result in Chapter 4 where there was additional dependence on the neutral density because of ion-neutral collisions.

BIBLIOGRAPHY

[1] Cusson, S., Hofer, R., Vazsonyi, A., Jorns, B., and Gallimore, A., "A 30-kW Class Magnetically Shielded Nested Hall Thruster," *The 36th International Electric Propulsion Conference*, 2019.

[2] Goebel, D. M., Jameson, K. K., Katz, I., and Mikellides, I. G., "Potential fluctuations and energetic ion production in hollow cathode discharges," *Physics of Plasmas (1994-present)*, Vol. 14, No. 10, Oct. 2007, pp. 103508.

[3] Jorns, B. A., Dodson, C., Goebel, D. M., and Wirz, R., "Propagation of ion acoustic wave energy in the plume of a high-current LaB6 hollow cathode," *Physical Review E*, Vol. 96, No. 2, Aug. 2017, pp. 023208.

[4] Mikellides, I. G., Katz, I., Goebel, D. M., and Jameson, K. K., "Evidence of nonclassical plasma transport in hollow cathodes for electric propulsion," *Journal of Applied Physics*, Vol. 101, No. 6, March 2007, pp. 063301.

[5] Mikellides, I., Ortega, A. L., Goebel, D. M., and Becatti, G., "Dynamics of a hollow cathode discharge in the frequency range of 1-500 kHz," *Plasma Sources Science and Technology*, 2020.

[6] Goebel, D. M. and Katz, I., *Fundamentals of electric propulsion: ion and Hall thrusters*, Vol. 1, John Wiley & Sons, 2008.

[7] Paschen, F., "Bohrs Heliumlinien," *Annalen der Physik*, Vol. 355, No. 16, 1916, pp. 901–940.

[8] Eichhorn, H., Schoenbach, K. H., and Tessnow, T., "Paschen's law for a hollow cathode discharge," *Applied Physics Letters*, Vol. 63, No. 18, Nov. 1993, pp. 2481–2483.

[9] Goebel, D. M. and Watkins, R. M., "Compact lanthanum hexaboride hollow cathode," *Review of Scientific Instruments*, Vol. 81, No. 8, Aug. 2010, pp. 083504.

[10] Chu, E. and Goebel, D. M., "High-Current Lanthanum Hexaboride Hollow Cathode for 10-to-50-kW Hall Thrusters," *IEEE Transactions on Plasma Science*, Vol. 40, No. 9, Sept. 2012, pp. 2133–2144.

[11] Goebel, D. M. and Chu, E., "High-Current Lanthanum Hexaboride Hollow Cathode for High-Power Hall Thrusters," *Journal of Propulsion and Power*, Vol. 30, No. 1, 2014, pp. 35–40.

[12] Goebel, D. M. and Polk, J. E., "Lanthanum Hexaboride Hollow Cathode for the Asteroid Redirect Robotic Mission 12.5 kW Hall Thruster," 2015.

[13] Sarver-Verhey, T. R., Kamhawi, H., Goebel, D. M., Polk, J. E., Peterson, P. Y., and Robinson, D. A., "Hollow Cathode Assembly Development for the HERMeS Hall Thruster," *52nd AIAA/SAE/ASEE Joint Propulsion Conference*, American Institute of Aeronautics and Astronautics, Salt Lake City, UT, July 2016.

[14] Mikellides, I., Katz, I., Goebel, D., and Polk, J., "Theoretical model of a hollow cathode insert plasma," *AIAA Paper*, Vol. 3817, 2004, pp. 11–14.

[15] Mikellides, I. G., Katz, I., and Goebel, D. M., "Numerical simulation of the hollow cathode discharge plasma dynamics," *29th Int. Electric Propulsion Conf.*, 2005.

[16] Mikellides, I. G., Katz, I., Goebel, D. M., and Polk, J. E., *Theoretical model of a hollow cathode plasma for the assessment of insert and keeper lifetimes*, Pasadena, CA: Jet Propulsion Laboratory, National Aeronautics and Space Administration, 2005.

[17] Mikellides, I. G., Katz, I., Goebel, D. M., Polk, J. E., and Jameson, K. K., "Plasma processes inside dispenser hollow cathodes," *Physics of Plasmas (1994-present)*, Vol. 13, No. 6, 2006, pp. 063504.

[18] Katz, I., Mikellides, I. G., Goebel, D. M., and Polk, J. E., "Insert Heating and Ignition in Inert-Gas Hollow Cathodes," *IEEE Transactions on Plasma Science*, Vol. 36, No. 5, Oct. 2008, pp. 2199–2206.

[19] Goebel, D., Katz, I., Watkins, R., and Jameson, K., "Hollow Cathode and Keeper-Region Plasma Measurements Using Ultra-Fast Miniature Scanning Probes," *40th AIAA/ASME/SAE/ASEE Joint Propulsion Conference and Exhibit*, American Institute of Aeronautics and Astronautics.

[20] Mikellides, I., Katz, I., Jameson, K., and Goebel, D., "Driving Processes in the Orifice and Near-Plume Regions of a Hollow Cathode," American Institute of Aeronautics and Astronautics, July 2006.

[21] Katz, I., Anderson, J. R., Polk, J. E., and Brophy, J. R., "One-dimensional hollow cathode model," *Journal of Propulsion and Power*, Vol. 19, No. 4, 2003, pp. 595–600.

[22] Katz, I., Mikellides, I., Goebel, D., Jameson, K., Wirz, R., and Johnson, L., "Production of High Energy Ions Near an Ion Thruster Discharge Hollow Cathode," *42nd AIAA/ASME/SAE/ASEE Joint Propulsion Conference & Exhibit*, American Institute of Aeronautics and Astronautics, Sacramento, California, July 2006.

[23] Rawlin, V. K., Sovey, J. S., Anderson, J. R., and Polk, J. E., "NSTAR flight thruster qualification testing," *AIAA Paper*, , No. 98-3936, 1998.

[24] Polk, J. E., Anderson, J. R., Brophy, J. R., Rawlin, V. K., Patterson, M. J., Sovey, J., and Hamley, J., "An overview of the results from an 8200 hour wear test of the NSTAR ion thruster," *AIAA Paper*, Vol. 2446, 1999, pp. 1999.

[25] Polk, J. E., Kakuda, R. Y., Anderson, J. R., Brophy, J. R., Rawlin, V. K., Patterson, M. J., Sovey, J., and Hamley, J., "Validation of the NSTAR ion propulsion system on the Deep Space One mission: overview and initial results," *AIAA paper*, Vol. 99, 1999, pp. 2274.

[26] Wilbur, P. J., Rawlin, V. K., and Beattie, J. R., "Ion thruster development trends and status in the United States," *Journal of Propulsion and Power*, Vol. 14, No. 5, 1998, pp. 708–715.

[27] Polk, J. E., Brinza, D., Kakuda, R. Y., Brophy, J. R., Katz, I., Anderson, J. R., Rawlin, V. K., Patterson, M. J., Sovey, J., and Hamley, J., "Demonstration of the NSTAR ion propulsion system on the Deep Space One mission," *27th International Electric Propulsion Conference, Pasadena, CA*, Citeseer, 2001.

[28] Kaufman, H. R., "Technology of Electron-Bombardment Ion Thrusters," *Advances in Electronics and Electron Physics*, edited by L. Marton, Vol. 36, Academic Press, 1975, pp. 265–373.

[29] Csiky, G. A., "Measurements of some properties of a discharge from a hollow cathode," *NASA Technical Note*, 1969.

[30] Philip, C., "A Study of Hollow Cathode Discharge Characteristics," *AIAA Journal*, Vol. 9, No. 11, Nov. 1971, pp. 2191–2196.

[31] Rawlin, V. K., Banks, B. A., and Byers, D. C., "Design, fabrication, and operation of dished accelerator grids on a 30-cm ion thruster," 17-19 Apr. 1972, United States, Jan. 1972.

[32] Brophy, J. and Garner, C., "Tests of high current hollow cathodes for ion engines," *24th Joint Propulsion Conference*, American Institute of Aeronautics and Astronautics, Boston,MA,U.S.A., July 1988.

[33] Friedly, V. J. and Wilbur, P. J., "High current hollow cathode phenomena," *Journal of Propulsion and Power*, Vol. 8, No. 3, 1992, pp. 635–643.

[34] Kameyama, I. and Wilbur, P. J., "Measurements of Ions from High-Current Hollow Cathodes Using Electrostatic Energy Analyzer," *Journal of Propulsion and Power*, Vol. 16, No. 3, 2000, pp. 529–535.

[35] Hall, S. J., Gray, T. G., Yim, J. T., Choi, M., Mooney, M. M., Timothy, S.-V. R., and Kamhawi, H., "The Effect of Anode Position on Operation of a 25-A class Hollow Cathode," ERPS, 2019, p. 299.

[36] Hall, S. J., Yim, J. T., Choi, M., Mooney, M. M., Sarver-Verhey, T. R., and Kamhawi, H., "The Effect of a Hall Thruster-like Magnetic Field on Operation of a 25-A class Hollow Cathode," 300, ERPS, 2019.

[37] Fife, J., Martinez-Sanchez, M., Szabo, J., Fife, J., Martinez-Sanchez, M., and Szabo, J., "A numerical study of low-frequency discharge oscillations in Hall thrusters," American Institute of Aeronautics and Astronautics, July 1997.

[38] Hara, K., Sekerak, M. J., Boyd, I. D., and Gallimore, A. D., "Mode transition of a Hall thruster discharge plasma," *Journal of Applied Physics*, Vol. 115, No. 20, May 2014, pp. 203304.

[39] Hara, K., Sekerak, M. J., Boyd, I. D., and Gallimore, A. D., "Perturbation analysis of ionization oscillations in Hall effect thrusters," *Physics of Plasmas (1994-present)*, Vol. 21, No. 12, Dec. 2014, pp. 122103.

[40] Mandell, M. and Katz, I., "Theory of hollow operation in spot and plume modes," American Institute of Aeronautics and Astronautics, June 1994.

[41] Pekarek, L., "Ionization Waves (Striations) in a Discharge Plasma," *Soviet Physics Uspekhi*, Vol. 11, March 1968, pp. 188–208.

[42] Lee, D. A. and Garscadden, A., "Standing Striations as Solutions of the Pekarek Equation," *Physics of Fluids (1958-1988)*, Vol. 15, No. 10, Oct. 1972, pp. 1826–1830.

[43] Nedospasov, A. V., "Striations," *Physics-Uspekhi*, Vol. 11, No. 2, 1968, pp. 174–187.

[44] Robertson, H. S., "Moving Striations in Direct Current Glow Discharges," *Physical Review*, Vol. 105, No. 2, Jan. 1957, pp. 368–377.

[45] Oleson, N. L. and Cooper, A. W., "Moving Striations," *Advances in Electronics and Electron Physics*, edited by L. Marton, Vol. 24, Academic Press, 1968, pp. 155–278.

[46] Kolobov, V. I., "Striations in rare gas plasmas," *Journal of Physics D: Applied Physics*, Vol. 39, No. 24, 2006, pp. R487.

[47] Georgin, M. P., Jorns, B. A., and Gallimore, A. D., "An Experimental and Theoretical Study of Hollow Cathode Plume Mode Oscillations," Vol. IEPC-2017-298, Electric Rocket Propulsion Society, Atlanta Georgia, Oct. 2017.

[48] Georgin, M. P., Jorns, B. A., and Gallimore, A. D., "Experimental Evidence for Ion Acoustic Solitons in the Plume of a Hollow Cathode," Vol. 403, Sevilla, Spain, May 2018, p. 12.

[49] Tran, M. Q., "Ion Acoustic Solitons in a Plasma: A Review of their Experimental Properties and Related Theories," *Physica Scripta*, Vol. 20, No. 3-4, 1979, pp. 317.

[50] Sheridan, T. E., Yi, S., and Lonngren, K. E., "On the origin of the ion acoustic soliton," *Physics of Plasmas*, Vol. 5, No. 9, Sept. 1998, pp. 3165–3170.

[51] Dauxois, T. and Peyrard, M., *Physics of Solitons*, Cambridge University Press, March 2006, Google-Books-ID: YKe1UZc_Qo8C.

[52] Chuang, S.-H. and Hau, L.-N., "The characteristics of ion acoustic solitons in non-Maxwellian plasmas," *Physics of Plasmas*, Vol. 16, No. 2, Feb. 2009, pp. 022901.

[53] Lafleur, T. and Boswell, R. W., "Particle-in-cell simulations of hollow cathode enhanced capacitively coupled radio frequency discharges," *Physics of Plasmas*, Vol. 19, No. 2, Feb. 2012, pp. 023508.

[54] Mikellides, I. G., Goebel, D. M., Jorns, B. A., Polk, J. E., and Guerrero, P., "Numerical Simulations of the Partially Ionized Gas in a 100-A LaB6 Hollow Cathode," *IEEE Transactions on Plasma Science*, Vol. 43, No. 1, Jan. 2015, pp. 173–184.

[55] Lopez Ortega, A., Mikellides, I. G., and Jorns, B., "First-principles modeling of the IAT-driven anomalous resistivity in hollow cathode discharges II: Numerical simulations and comparison with measurements," American Institute of Aeronautics and Astronautics, July 2016.

[56] Sary, G., Garrigues, L., and Boeuf, J.-P., "Hollow cathode modeling: I. A coupled plasma thermal two-dimensional model," *Plasma Sources Science and Technology*, Vol. 26, No. 5, 2017, pp. 055007.

[57] Sary, G., Garrigues, L., and Boeuf, J.-P., "Hollow cathode modeling: II. Physical analysis and parametric study," *Plasma Sources Science and Technology*, Vol. 26, No. 5, 2017, pp. 055008.

[58] Mikellides, I., Katz, I., and Goebel, D., "Model of the Plasma Potential Distribution in the Plume of a Hollow Cathode," *40th AIAA/ASME/SAE/ASEE Joint Propulsion Conference and Exhibit*, American Institute of Aeronautics and Astronautics, Fort Lauderdale, Florida, July 2004.

[59] Mikellides, I. G., Katz, I., Goebel, D. M., Jameson, K. K., and Polk, J. E., "Wear mechanisms in electron sources for ion propulsion, II: Discharge hollow cathode," *Journal of Propulsion and Power*, Vol. 24, No. 4, 2008, pp. 866–879.

[60] Lopez Ortega, A., Mikellides, I. G., Sekerak, M. J., and Jorns, B. A., "Plasma simulations in 2-D (r-z) geometry for the assessment of pole erosion in a magnetically shielded Hall thruster," *Journal of Applied Physics*, Vol. 125, No. 3, Jan. 2019, pp. 033302.

[61] Jorns, B. A., Mikellides, I. G., and Goebel, D. M., "Ion acoustic turbulence in a 100-A LaB6 hollow cathode," *Physical Review E*, Vol. 90, No. 6, Dec. 2014, pp. 063106.

[62] Mikellides, I. G., Guerrero, P., Lopez Ortega, A., and Polk, J. E., "Spot-to-plume Mode Transition Investigations in the HERMeS Hollow Cathode Discharge Using Coupled 2-D Axisymmetric Plasma-Thermal Simulations," American Institute of Aeronautics and Astronautics, July 2018.

[63] Jorns, B., Lopez Ortega, A., and Mikellides, I. G., "First-principles Modelling of the IAT-driven Anomalous Resistivity in Hollow Cathode Discharges I: Theory," American Institute of Aeronautics and Astronautics, July 2016.

[64] Sagdeev, R. Z., "The 1976 Oppenheimer lectures: Critical problems in plasma astrophysics. I. Turbulence and nonlinear waves," *Reviews of Modern Physics*, Vol. 51, No. 1, Jan. 1979, pp. 1–9.

[65] Jorns, B. A. and Hofer, R. R., "Plasma oscillations in a 6-kW magnetically shielded Hall thruster," *Physics of Plasmas (1994-present)*, Vol. 21, No. 5, May 2014, pp. 053512.

[66] Dodson, C. A., Perez-Grande, D., Jorns, B. A., Goebel, D. M., and Wirz, R. E., "Ion Heating Measurements on the Centerline of a High-Current Hollow Cathode Plume," *Journal of Propulsion and Power*, Vol. 34, No. 5, 2018, pp. 1225–1234.

[67] Dodson, C., Jorns, B. A., and Wirz, R. E., "Measurements of ion velocity and wave propagation in a hollow cathode plume," *Plasma Sources Science and Technology*, 2019.

[68] Ortega, A. L., Jorns, B. A., and Mikellides, I. G., "Hollow Cathode Simulations with a First-Principles Model of Ion-Acoustic Anomalous Resistivity," *Journal of Propulsion and Power*, Vol. 34, No. 4, 2018, pp. 1026–1038.

[69] Stix, T. H., *The Theory of Plasma Waves*, 1962.

[70] Kanik, I., Johnson, P. V., and James, G. K., "Electron-impact-induced emission and excitation cross sections of xenon at low energies," *Journal of Physics B: Atomic, Molecular and Optical Physics*, Vol. 34, No. 9, 2001, pp. 1685.

[71] Chesta, E., Lam, C. M., Meezan, N. B., Schmidt, D. P., and Cappelli, M. A., "A characterization of plasma fluctuations within a Hall discharge," *IEEE Transactions on Plasma Science*, Vol. 29, No. 4, Aug. 2001, pp. 582–591.

[72] Carter, T. A., Brugman, B., Pribyl, P., and Lybarger, W., "Laboratory Observation of a Nonlinear Interaction between Shear Alfv\'en Waves," *Physical Review Letters*, Vol. 96, No. 15, April 2006, pp. 155001.

[73] Dorfman, S. and Carter, T. A., "Nonlinear Excitation of Acoustic Modes by Large-Amplitude Alfv\'en Waves in a Laboratory Plasma," *Physical Review Letters*, Vol. 110, No. 19, May 2013, pp. 195001.

[74] Williams, G.J., J., Smith, T., Domonkos, M., Gallimore, A., and Drake, R., "Laser-induced fluorescence characterization of ions emitted from hollow cathodes," *IEEE Transactions on Plasma Science*, Vol. 28, No. 5, Oct. 2000, pp. 1664–1675.

[75] Honzawa, T. and Kawai, Y., "Ion heating caused by ion acoustic waves in an ion-streaming plasma," *Plasma Physics*, Vol. 14, No. 1, Jan. 1972, pp. 27–36.

[76] Pots, B. F. M., Coumans, J. J. H., and Schram, D. C., "Collective scattering of CO2-laser light from ion-acoustic turbulence," *The Physics of Fluids*, Vol. 24, No. 3, March 1981, pp. 517–527.

[77] Ilić, D. B., "Spectra of ion acoustic plasma instability," *The Physics of Fluids*, Vol. 20, No. 10, Oct. 1977, pp. 1717–1727.

[78] Beall, J. M., Kim, Y. C., and Powers, E. J., "Estimation of wavenumber and frequency spectra using fixed probe pairs," *Journal of Applied Physics*, Vol. 53, No. 6, June 1982, pp. 3933–3940.

[79] Nold, B., Ribeiro, T. T., Ramisch, M., Huang, Z., Müller, H. W., Scott, B. D., and and, U. S., "Influence of temperature fluctuations on plasma turbulence investigations with Langmuir probes," *New Journal of Physics*, Vol. 14, No. 6, June 2012, pp. 063022.

[80] Jorns, B. A., Mikellides, I. G., and Goebel, D. M., "Investigation of Energetic Ions in a 100-A Hollow Cathode," *50th AIAA/ASME/SAE/ASEE Joint Propulsion Conference*, 2014, p. 3826.

[81] Georgin, M. P., Jorns, B., and Gallimore, A., "Time-varying Non-classical Collisions and Turbulence in a Hollow Cathode," *AIAA Propulsion and Energy 2019 Forum*, American Institute of Aeronautics and Astronautics, Indianapolis, IN, Aug. 2019.

[82] Georgin, M. P., Jorns, B. A., and Gallimore, A. D., "Correlation of ion acoustic turbulence with self-organization in a low-temperature plasma," *Physics of Plasmas*, Vol. 26, No. 8, Aug. 2019, pp. 082308.

[83] Tsikata, S. and Minea, T., "Modulated Electron Cyclotron Drift Instability in a High-Power Pulsed Magnetron Discharge," *Physical Review Letters*, Vol. 114, No. 18, May 2015, pp. 185001.

[84] Subramanian, K. P. and Kumar, V., "Total electron scattering cross sections for argon, krypton and xenon at low electron energies," *Journal of Physics B: Atomic and Molecular Physics*, Vol. 20, No. 20, Oct. 1987, pp. 5505–5515.

[85] Huba, J. D., *NRL Plasma Formulary*, The Office of Naval Research, 2016.

[86] Lotka, A. J., "Analytical note on certain rhythmic relations in organic systems," *Proceedings of the National Academy of Sciences*, Vol. 6, No. 7, 1920, pp. 410–415.

[87] Garrigues, L., Sary, G., Vincent, B., Tsikata, S., and Mazouffre, S., "Numerical modeling and incoherent Thomson scattering measurements of a 5A cathode with LaB6 emitter," *IEPC 2019*, p. 783.

[88] Sagdeev, R. Z. and Galeev, A. A., *Nonlinear Plasma Theory*, 1969.

[89] Chen, F. F., "Langmuir probe diagnostics," *IEEE-ICOPS Meeting, Jeju, Korea*, Vol. 2, 2003.

[90] Jorns, B. A. and Hofer, R. R., "Low Frequency Plasma Oscillations in a 6-kW Magnetically Shielded Hall Thruster," *49th AIAA/ASME/SAE/ASEE Joint Propulsion Conference*, American Institute of Aeronautics and Astronautics, 2013.

[91] Cusson, S. E., Jorns, B., and Gallimore, A., "Simple Model for Cathode Coupling Voltage Versus Background Pressure in a Hall Thruster," *53rd AIAA/SAE/ASEE Joint Propulsion Conference*, American Institute of Aeronautics and Astronautics, Atlanta, GA, July 2017.

[92] Cusson, S. E., Jorns, B. A., and Gallimore, A., "Ion Acoustic Turbulence in the Hollow Cathode Plume of a Hall Effect Thruster," *2018 Joint Propulsion Conference*, American Institute of Aeronautics and Astronautics, Cincinnati, Ohio, July 2018.

[93] Jorns, B. A., Cusson, S. E., Brown, Z., and Dale, E. T., "Non-classical Electron Transport in the Cathode Plume of a Hall E ect Thruster," *Physics of Plasmas -Submitted*, 2019.

[94] Frias, W., Smolyakov, A. I., Kaganovich, I. D., and Raitses, Y., "Long wavelength gradient drift instability in Hall plasma devices. I. Fluid theory," *Physics of Plasmas*, Vol. 19, No. 7, July 2012, pp. 072112.

[95] Ilić, D. B., "Measurement of Ion-Acoustic Plasma Turbulence by Cross-Power Spectra," *Physical Review Letters*, Vol. 34, No. 8, Feb. 1975, pp. 464–466.